Parallel Supercomputer Simulations
of
Cosmic Evolution

Dissertation der Fakultät für Physik

der

Ludwig–Maximilians–Universität München

vorgelegt von
Jörg Colberg
aus Wilhelmshaven

München, den 29.11.1999

Parallel Supercomputer Simulations
of
Cosmic Evolution

Dissertation der Fakultät für Physik

der

Ludwig–Maximilians–Universität München

vorgelegt von
Jörg Colberg
aus Wilhelmshaven

München, den 29.11.1999

Contents

Simulationen der Entstehung und Entwicklung von Strukturen im Kosmos

(Deutsche Zusammenfassung)

> *Daß die Welt* nicht *der Inbegriff einer ewigen Vernünftigkeit ist, läßt sich endgültig dadurch beweisen, daß jenes* Stück Welt, *welches wir kennen – ich meine unsre menschliche Vernunft –, nicht allzu vernünftig ist. Und wenn* sie *nicht allezeit und vollständig weise und rationell ist, so wird es die übrige Welt auch nicht sein; hier gilt der Schluß* a minori ad maius, a parte ad totum, *und zwar mit entscheidender Kraft.*
>
> Friedrich Nietzsche
> Menschliches, Allzumenschliches, Bd. 2, 2.2

1.1. Einleitung

Im Verlaufe der zurückliegenden zwanzig Jahre hat sich die Kosmologie zu einer eigenständigen Wissenschaft entwickelt, die anderen naturwissenschaftlichen Disziplinen in Bezug auf die Präzision von Beobachtungen und theoretischen Vorhersagen in nichts mehr nachsteht. Die Menge an Wissen, die in diesem Zeitraum angehäuft werden konnte, läßt einen Vergleich mit der Entwicklung der Quantenmechanik und der nachfolgenden Revolution in der Atomphysik durchaus zu.

Die Kosmologie hat hierbei maßgeblich von den gewaltigen technologischen Entwicklungen profitiert. Der COBE–Satellit[1] zum Beispiel hat die Mikrowellenhintergrundstrahlung mit

---

[1]COBE ist die Abkürzung für Cosmic Microwave Background Explorer.

einer bis dato unerreichten Präzision vermessen. Dabei zeigte sich, daß diese Strahlung, die die Erde als Nachglühen des Urknalls erreicht, ein Spektrum hat, das nahezu *perfekt* dem eines Planck'schen Schwarzen Strahlers entspricht. Zudem muß es im frühen Universum Dichte–Fluktuationen in der Materie von der Größenordnung 10^{-5} gegeben haben. Das Hubble–Space–Teleskop (HST) und neue Teleskope auf der Erde haben es ermöglicht, Galaxien bei einer Rotverschiebung von 5 zu finden, d.h. zu einer Zeit, als das Universum ein Sechstel seiner heutigen Größe hatte. Gleichermaßen zeigte sich in immer deutlicherem Maße, daß ein großer Teil der Materie im Universum in einer Form vorliegt, die sich vollständig von der unterscheidet, wie man sie von der Erde kennt. Diese Dunkle Materie zeigt sich ausschließlich durch den Einfluß ihrer Schwerkraft, indem sie z.B. das Licht von Galaxien, die sich hinter einem Galaxienhaufen befinden, ablenkt und um diesen herum verzerrte Abbilder erzeugt. Diese Liste ist keineswegs vollständig. Alle Theorien der Geburt des Universums und der nachfolgenden Entstehung und Entwicklung von Galaxien und von großräumigen Strukturen müssen ihr Rechnung tragen und Erklärungen und Modelle dafür bieten.

Die neuen Beobachtungsdaten haben Theoretikern abverlangt, bestehende Theorien zu überprüfen und, wo nötig, zu überarbeiten, insbesondere aber Vorhersagen von größerer Präzision zu erarbeiten. Es stellte sich dabei heraus, daß die einfachsten Theorien mit den Beobachtungen nicht zu vereinbaren waren. Allerdings zeigte sich gleichermaßen, daß die notwendigen Korrekturen und Verfeinerungen der Modelle relativ einfach durchzuführen waren. Computersimulationen haben hierbei eine wichtige Rolle gespielt. Der gewaltige Anstieg der Leistungsfähigkeit moderner Supercomputer ist hierbei nicht der alleinige Grund für diese Entwicklung. So konnte das Modell, demzufolge die Dunkle Materie ausschließlich aus Neutrinos besteht, mit einer Simulation mit nur 1000 Teilchen ausgeschlossen werden (White et al. 1983). Nichtsdestotrotz waren und sind große Simulationen nötig, um hinreichend exakte Vorhersagen zu erzielen. Sehr große Ausschnitte des Universums müssen mit einer hohen Massenauflösung simuliert werden, um zukünftige Tests von kosmologischen Modellen zu ermöglichen.

Im folgenden Abschnitt werden die zunächst die grundlegenden Konzepte moderner Kosmologie und das Cold Dark Matter–Modell motiviert. Abschnitt 1.2 befaßt sich mit der Verteilung der Materie auf großen Skalen. In Abschnitt 1.3 werden die Pekuliargeschwindigkeiten der massereichsten Objekte im Universum (Galaxienhaufen) untersucht. Galaxienhaufen stehen auch im Mittelpunkt in Abschnitt 1.4, der die Entstehung und räumliche Verteilung von Galaxienhaufen in den bislang größten und umfangreichsten Computersimulationen des Universums beschreibt.

1.1.1. Moderne Kosmologie und das Cold Dark Matter–Modell

Zum Urknall als Modell für die Entstehung des Universums gibt es mittlerweile keine ernstzunehmende Alternative mehr. Die Theorie, die die Dynamik des Gravitationsfeldes im Universum beschreibt, ist Einsteins Allgemeine Relativitätstheorie. Sie nimmt an, daß das Universum auf großen Skalen gleichförmig und homogen ist und daß es keinen bevorzugten Ort im

Universum gibt. Die Metrik hierfür ist die Friedmann–Robertson–Walker–Metrik

$$ds^2 = (c\mathrm{d}t)^2 - a^2(t)\left[\frac{\mathrm{d}r^2}{1 - kr^2} + r^2(\mathrm{d}\vartheta^2 + \sin^2\vartheta\mathrm{d}\phi^2)\right].\tag{1.1}$$

Der sogenannte Expansionsfaktor $a(t)$ (Dimension: Länge) und die Krümmung k (dimensionslos; nimmt die Werte 1, 0, und -1 an für positive, keine und negative Krümmung räumlicher Hyperflächen) sind hierbei mithilfe der Einstein'schen Feldgleichungen zu bestimmen. Unter der Annahme von Homogenität und Isotropie lassen sich diese Gleichungen vereinfacht schreiben als

$$\frac{\dot{a}^2 + kc^2}{a^2} = \frac{8\pi G}{3}\rho\,,\tag{1.2}$$

$$\frac{2\ddot{a}}{a} + \frac{\dot{a}^2 + kc^2}{a^2} = -8\pi G p\,,\tag{1.3}$$

wobei G die Gravitationskonstante ist, und p und ρ sind der Druck und die Dichte des Fluids, das sich im Universum befindet. Der Punkt bezeichnet Ableitung nach der Zeit. Es ist üblich in der Kosmologie, folgende Größen zu definieren:

$$H_0 \equiv \left(\frac{\dot{a}}{a}\right)_{t=t_0}\tag{1.4}$$

$$\rho_c \equiv \frac{3H_0^2}{8\pi G}\tag{1.5}$$

$$\Omega \equiv \frac{\rho_0}{\rho_c}\tag{1.6}$$

Diese sind die sog. Hubble–Konstante zur heutigen Zeit, H_0, die kritische Dichte, ρ_c, und der Dichteparameter, Ω. Der Krümmungsterm k wird dann bestimmt durch

$$k = H_0^2(\Omega - 1)\,.\tag{1.7}$$

Das Universum ist nur auf sehr großen Skalen homogen. Das Wachstum von Inhomogenitäten aus kleinen Fluktuationen läßt sich in linearer Theorie berechnen. Betrachtet man ein Fluid der Dichte ρ und Geschwindigkeit $\mathbf{v}$ mit $p = 0$, das sich in einem Schwerefeld mit dem Potential Φ bewegt, so wird das Fluid beschrieben durch die Kontinuitätsgleichung und die Euler– und Poissongleichungen:

$$\frac{\partial\rho}{\partial t} + \nabla\cdot(\rho\mathbf{v}) = 0\,,\tag{1.8}$$

$$\frac{\partial\mathbf{v}}{\partial t} + (\mathbf{v}\cdot\nabla)\mathbf{v} = -\nabla\Phi\,,\tag{1.9}$$

$$\nabla^2\Phi = 4\pi G\rho\,.\tag{1.10}$$

Mit der Annahme eines räumlich variierenden Dichtefeldes

$$\rho(\mathbf{x}, t) = \bar{\rho}(t)\cdot(1 + \delta(\mathbf{x}, t))\,,\tag{1.11}$$

und $\delta \ll 1$, ergibt sich nach Vernachlässigung aller nichtlinearen Terme

$$\ddot{\delta} + 2\frac{\dot{a}}{a}\dot{\delta} - 4\pi\,G\,\bar{\rho}\,\delta = 0\,. \tag{1.12}$$

Diese Gleichung beschreibt das *lineare* Wachstum von Strukturen im Universum, die ja, wie durch den COBE–Satelliten bestätigt, aus sehr kleinen anfänglichen Dichteschwankungen resultiert sein müssen. Für den einfachen Fall $\Omega = 1$ z.B. ergibt sich die anwachsende Lösung als[2]

$$\delta \propto D(t) \propto t^{2/3} \propto a\,. \tag{1.13}$$

$D(t)$ beschreibt hier explizit das Wachstum der Struktur. t ist die Zeitvariable. Für $\Omega < 1$ sind die Lösungen komplizierter, hier gerät der anwachsende Teil der Lösung in Sättigung, und die Struktur wächst im wesentlichen ab einem bestimmten Zeitpunkt an kaum weiter.

Wie bereits oben angedeutet, gibt es Evidenz, daß ein großer Teil der Materie im Universum in Form von Dunkler Materie vorliegt. Ebenso wurde erwähnt, daß Neutrinos aus theoretischen Erwägungen nicht den überwiegenden Teil dieser Materie stellen können. Der Grund hierfür ist, daß sich Neutrinos nach ihrer Entkopplung relativistisch bewegen – sie werden deswegen auch Heiße Dunkle Materie (engl. Hot Dark Matter, HDM) genannt – und so Fluktuationen auf kleinen Skalen auswaschen. Die Struktur, wie sie im Universum beobachtet wird, hätte sich nicht bilden können. Die Dunkle Materie muß also in einer Form vorliegen, die bei ihrer Entkopplung nichtrelativistisch war. Diese sogenannte Kalte Dunkle Materie (engl. Cold Dark Matter, CDM) konnte bislang noch nicht direkt nachgewiesen werden. Es gibt aber Kandidaten hierfür, Elementarteilchen, wie sie von verschiedenen Erweiterungen des Standardmodells der Elementarteilchenphysik vorhergesagt werden. Als eine der Haupthypothesen dieser Arbeit wird angenommen, daß die Dunkle Materie ausschließlich aus CDM besteht.

Wie sind die Dichteschwankungen im Universum entstanden? Diese Frage wird von einer Theorie beantwortet, die ursprünglich viel gewichtigeren Fragen zugewandt war: Warum ist im Universum der Dichteparameter $\Omega \approx 1$? Warum finden sich im Universum nicht die riesige Anzahl von magnetischen Monopolen, die eigentlich während des Phasenübergangs im frühen Universum hätten entstanden sein müssen? Und wieso sind die Variationen in der kosmischen Hintergrundstrahlung so klein, wenn doch die Bereiche, aus denen sie kommt, während der Rekombination kausal getrennt waren? Eine plausible Antwort hierauf gibt die Theorie der Inflation, derzufolge sich das Universum während einer sehr frühen und sehr kurzen Phase nach dem Urknall exponentiell ausdehnte, so daß Quantenfluktuationen auf kosmische Skalen gedehnt wurden. Damit werden die gestellten Fragen geklärt. Aber Inflation kann noch mehr: Es ist nämlich möglich, ein Spektrum der Dichtefluktuationen anzugeben. Dieses ist, weil von Quantenfluktuationen herrührend, Gaussisch. Wenn alle physikalischen Effekte berücksichtigt werden, die das primordiale Spektrum noch ändern können, ergibt sich schließlich das lineare CDM–Spektrum, für das Bond & Efstathiou (1984) folgenden Fit angeben:

$$P(k) = \frac{Ak}{(1 + [ak/\Gamma + (bk/\Gamma)^{3/2} + (ck/\Gamma)^2]^\nu)^{2/\nu}}\,, \tag{1.14}$$

mit $a = 6.4\,h^{-1}\,\mathrm{Mpc}$, $b = 3.0\,h^{-1}\,\mathrm{Mpc}$, $c = 1.7\,h^{-1}\,\mathrm{Mpc}$, and $\nu = 1.13$. Hierbei wurde die Hubble–Konstante abgekürzt durch $H_0 = 100\,h^{-1}\,\mathrm{km/sec}$. Γ ist ein Parameter, der die für

---

[2]Die zweite Lösung beschreibt den Zerfall der Dichteschwankungen und ist deswegen nicht von Interesse.

Modell	Ω	Λ	h	Γ
OCDM	0.3	0.0	0.7	0.21
ΛCDM	0.3	0.7	0.7	0.21
SCDM	1.0	0.0	0.5	0.50
τCDM	1.0	0.0	0.5	0.21

Tabelle 1.1.: Die kosmologischen Modelle.

das jeweilige Modell charakteristische Skala des Spektrums beschreibt. Die Normierung des Spektrums, A, kann nicht eindeutig aus inflationären Szenarien vorhergesagt werden. In dieser Arbeit wird sie so gesetzt, daß in den Simulationen die im Universum beobachtete Anzahl massereicher Galaxienhaufen reproduziert wird. Dies wird üblicherweise ausgedrückt über σ_8, die mittlere quadratische Abweichung der Massenverteilung auf einer Skala von $8\,h^{-1}$ Mpc. Tabelle 1 gibt eine Übersicht über die vier kosmologischen Modelle, die in dieser Arbeit benutzt werden. Von diesen Modellen wurden zwei Gruppen gerechnet. Bei der ersten Gruppe (Virgo–Simulationen) ist das simulierte Volumen für alle Modelle gleich groß – ein Würfel der Kantenlänge $240\,h^{-1}$ Mpc. In der zweiten Gruppe (GIF–Simulationen) hat jedes Modell die gleiche Massenauflösung, d.h. die Teilchen haben gleiche Massen (von $2 \cdot 10^{10}\,M_\odot$). Jeweils 256^3 Teilchen wurden simuliert. Die Simulationen wurden im Rahmen des britisch–deutsch–kanadischen Virgo Supercomputing Consortiums durchgeführt.

1.2. Die Verteilung der Materie auf großen Skalen

In den ersten großen Galaxienkatalogen, die in den achtziger Jahren erstellt wurden, zeichnete sich ab, daß die Verteilung der Galaxien keineswegs gleichförmig ist. Abgesehen von den Galaxien, die sich in Gruppen oder Haufen befinden, sind praktisch alle Galaxien Teil eines komplizierten Netzwerkes. Seitdem ist die Debatte, woraus dieses Netzwerk gebildet wird, nicht mehr abgerissen. Sind die Galaxien bevorzugt in großen zweidimensionalen flachen Strukturen (engl. Sheets) angesiedelt, wie der erste CfA–Katalog mit der berühmten "Großen Mauer" zeigte (De Lapparant et al. 1986)? Oder liegen Galaxien bevorzugt in Filamenten, d.h. sind sie aneinandergereit wie Perlen einer Kette, wie z.B. Haynes (1986) vorschlug? Die ersten größeren Simulationen von CDM–Universen (z.B. Davis et al. 1985) zeigten qualitativ eine Materieverteilung, die der Verteilung der Galaxien in den Katalogen sehr ähnlich war. Allerdings ist die Auflösung solcher Simulationen bislang zu grob gewesen, um diese Fragen genauer zu beantworten.

Die Simulationen, die im Rahmen dieser Arbeit durchgeführt worden sind, haben es aufgrund ihrer sehr hohen Auflösung ermöglicht, sich mit der Frage nach der Verteilung der Materie auf großen Skalen zu beschäftigen. Abbildung A.4 zeigt einen Schnitt der Dicke $8.5\,\mathrm{Mpc}/h$ durch die τCDM GIF–Simulation zur heutigen Zeit. Direkt in der Mitte befindet sich eine große Region, die nur sehr wenig Materie enthält. Solche Regionen, die mit ihrem englischen Fachterm Voids genannt werden, zeichnen sich auch in Galaxienkatalogen ab. Um die Void befindet sich ein komplexes Netzwerk, darunter ein sehr massereicher Galaxien-

haufen[3] direkt südlich davon, sowie eine große Anzahl von Objekten, von denen die meisten sich entweder in Filamenten oder eventuell auch in Sheets befinden. Große Objekte treten zumeist gehäuft auf, während sich kleinere um sie gruppieren. Dieses Verhalten ist typisch für CDM–Universen. In diesen bilden sich zunächst kleine Objekte, die dann entweder durch Akkretion von Materie oder durch Kollisionen und anschließende Virialisierung größere Objekte bilden.

Dreidimensionale Darstellungen der Materieverteilung erlauben es, diese aus einem anderen Blickwinkel heraus zu untersuchen. Dazu wird die Materie auf ein Gitter verteilt, geglättet, und diejenige Materie, die sich in Zellen befindet, deren Überdichte[4] größer als ein Schwellwert ist, wird betrachtet. Einige dieser Zellen sind Teil eines größeren Objekts. Abbildung A.13 zeigt das größte Objekt in der τCDM GIF–Simulation bei einer Überdichte von 3. Dieses Objekt beinhaltet etwa 30% der Gesamtmasse, füllt etwa 1% des Gesamtvolumens aus und erstreckt sich periodisch über das gesamte Volumen – ein Effekt, der als Perkolation bekannt ist. Wird der Schwellwert der Überdichte erhöht, schrumpft das Objekt und zerbricht schließlich in viele kleine Objekte. Dieses Verhalten ist typisch für die CDM–Universen. Eine quantitative Untersuchung des größten Objekts ergibt, daß es im wesentlichen aus Filamenten zusammengesetzt ist – wie ja in Abbildung A.13 auch deutlich zu sehen ist.

Für sehr hohe Werte der Überdichte, etwa 180, bilden die Zellen nur noch spärische oder elliptische Objekte. Die massivsten dieser Objekte entsprechen den bereits erwähnten Galaxienhaufen. Es zeigt sich, daß sich diese Galaxienhaufen an bevorzugten Stellen innerhalb der Verteilung der Materie bilden: An den Stellen, wo mehrere Filamente oder Sheets aufeinander treffen. Die Materie, die den Galaxienhaufen bildet, strömt im zeitlichen Verlauf der Simulation entlang der Filamente oder Sheets in Richtung des Haufens. Damit stellen Galaxienhaufen in einem gewissen Sinne bevorzugte Objekte innerhalb der großräumigen Struktur dar. Dies gilt umso mehr, als sie sich, auf der kosmologischen Zeitskala betrachtet, erst sehr spät (etwa bei Rotverschiebungen um 0.3 oder 0.1, je nach dem Wert von Ω) bilden. So kann man z.B. erwarten, daß man zwischen zwei benachbarten Haufen im Universum ein Filament aus Dunkler Materie finden kann – für den Fall, daß sich das Universum wirklich durch ein CDM–Modell beschreiben läßt.

1.3. Pekuliargeschwindigkeiten von Galaxienhaufen

Galaxienhaufen sind nicht nur in Hinsicht auf ihre besondere Lage innerhalb der großräumigen Struktur von Interesse. Zunächst einmal sind sie vor allem die massereichsten Objekte, die sich im Universum bislang gebildet haben. Aufgrund ihrer großen Masse mußte Materie aus einer sehr großen Region im frühen Universum kollabieren. Das bedeutet nun, daß das Dichtefeld im Universum zu dieser Zeit, wenn es auf einer Skala von etwa $10\,\mathrm{Mpc}/h$ geglättet wird, in den Bereichen, wo Galaxienhaufen entstehen, deutliche Überdichten haben mußte. Eines der Hauptparadigmen von CDM–Szenarien besagt, daß alle Objekte aus solchen überdichten Bereichen, im folgenden wie im Englischen Peaks genannt, entstanden sind und daß die Masse

---

[3]Die Simulationen enthalten nur Dunkle Materie und keine Galaxien. Üblicherweise werden die größten Objekte, die in ihnen gefunden werden, mit den größten Objekten im Universum, Galaxienhaufen, identifiziert.

[4]Die Überdichte ergibt sich aus der Dichte, indem durch die mittlere Dichte geteilt und 1 subtrahiert wird.

eines Objekts im wesentlichen proportional zur Höhe eines solchen Peaks ist, wobei mit der Höhe eines Peaks schlichtwegs seine Überdichte mit Bezug auf die mittlere Dichte gemeint ist. Darüberhinaus sollte auch die Geschwindigkeit[5] eines Peaks, bestimmt über das geglättete Geschwindigkeitsfeld, mit der des entsprechenden Galaxienhaufens übereinstimmen. Die Virgo–Simulationen sind ideal, um diese Punkte zu untersuchen, weil sie einerseits eine relativ große Region des Universums enthalten und weil es andererseits in ihnen eine genügend große Anzahl von Galaxienhaufen gibt.

Die Geschwindigkeitsdispersion in CDM–Universen läßt sich analytisch berechnen, und auch Angaben über die Geschwindigkeiten von Peaks sind möglich, weil das Spektrum der Modelle, wie oben erwähnt, Gaussisch ist. Die theoretischen Vorhersagen sind hierbei

$$\sigma_{\mathrm{v}}(R) \equiv H_0\, \Omega^{0.6}\, \sigma_{-1}(R)\,, \tag{1.15}$$

wobei σ_j für eine ganze Zahl j definiert wird als

$$\sigma_j^2(R) = \frac{1}{2\pi^2} \int P(k)\, W^2(kR)\, k^{2j+2}\, \mathrm{d}k\,, \tag{1.16}$$

für das Integral über das gesamte Feld und

$$\sigma_{\mathrm{p}}(R) = \sigma_{\mathrm{v}}(R)\sqrt{1 - \sigma_0^4/\sigma_1^2\sigma_{-1}^2}\,, \tag{1.17}$$

für Peaks. $W(kR)$ ist eine Filterfunktion, in der die Glättungsskala gesetzt wird. In den Simulationen werden Galaxienhaufen als die größten Masseansammlungen zur heutigen Zeit gefunden. Die in ihnen enthaltenen Teilchen werden dann zu alle früheren Zeitpunkte markiert. Peaks werden über das geglättete Dichtefeld in den Anfangsbedingungen der Simulationen identifiziert. Die Glättungsskala wird hierbei derart gesetzt, daß sie der minimalen Masse der untersuchten Menge von Haufen entspricht.

Wie in Abbildung 1.1 zu sehen ist, kann der überwiegenden Mehrheit der Haufen tatsächlich ein hoher Peak zugeordnet werden. Allerdings ist die Streuung in der Zuordnung recht beträchtlich. Werden die Geschwindigkeit der Haufen in den Anfangsbedingungen, denen ein Peak zugeordnet werden kann, verglichen mit der Geschwindigkeit des entsprechenden Peaks, zeigt sich eine exzellente Entsprechung. Gleichermaßen gut ist die Übereinstimmung der Geschwindigkeiten der Peaks mit der analytischen Vorhersage (Gl. 1.17). Die Geschwindigkeitsdispersion der Haufen zur heutigen Zeit, direkt gemessen aus der Simulationen, ist jedoch deutlich größer als die der Haufen, wenn ihre Geschwindigkeiten aus den Anfangsbedingungen auf die heutige Zeit hochskaliert werden. Insbesondere zeigen Haufen, die einen benachbarten Haufen in einer maximalen Distanz von $10\, h^{-1}$Mpc haben, größere Abweichungen, wie in Abbildung 1.2 zu sehen ist.

Im wesentlichen entsprechen also Galaxienhaufen hohen Peaks mit gleichen Geschwindigkeiten im frühen Universum, wobei massereichen Haufen im allgemeinen höheren Peaks entsprechen. Allerdings führen nichtlineare Effekte dazu, daß die Geschwindigkeitsdispersion zur heutigen Zeit deutlich (um 40%) über der Vorhersage der linearen Theorie liegt.

---

[5]Im folgenden wird mit der Geschwindigkeit einer Objekts grundsätzlich seine Pekuliargeschwindigkeit bezeichnet, d.h. seine Geschwindigkeit in einem Bezugssystem, das sich mit der Hubble–Expansion mitbewegt. Desweiteren werden alle (Pekuliar–) Geschwindigkeiten auf ihre Werte zur heutigen Zeit hochgerechnet.
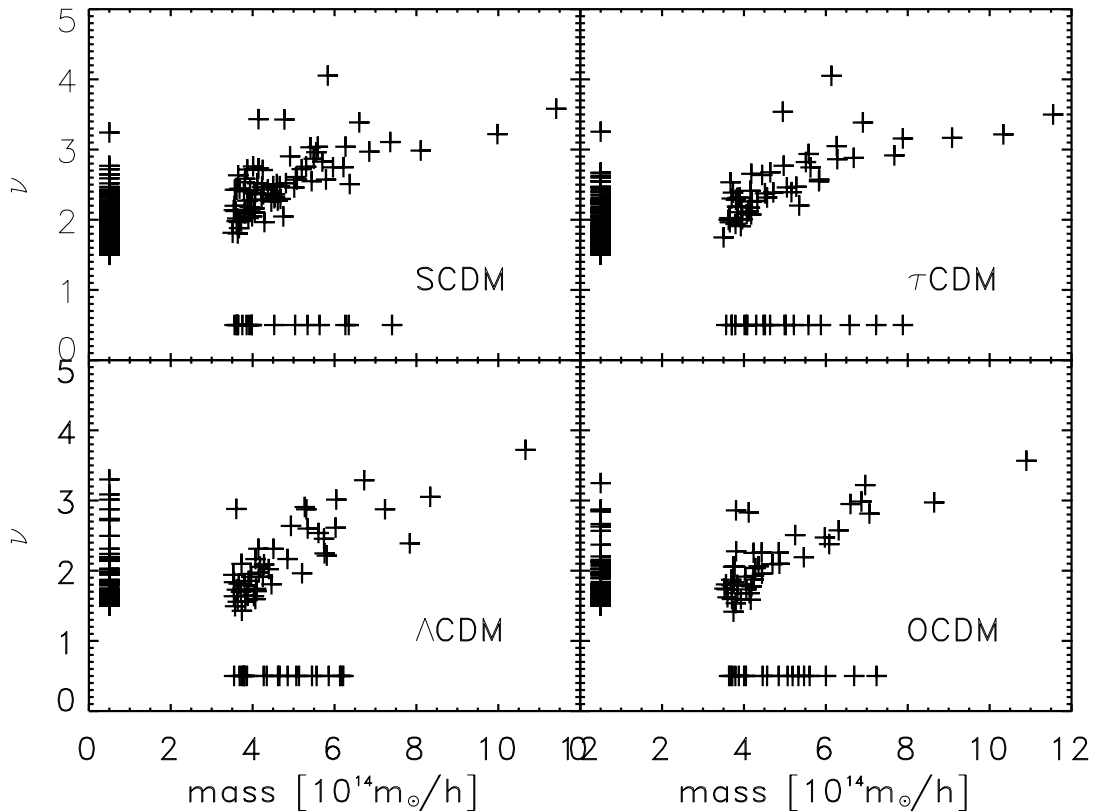
Abbildung 1.1.: Die Massen der Galaxienhaufen in den vier Simulationen in Abhängigkeit der Höhe der ihnen entsprechenden Peaks. Es gibt 351, 239, 84, und 83 Peaks ohne zugehörigen Haufen in der SCDM, τCDM, ΛCDM, und OCDM–Simulation. 85% und 75% der Haufen in den Modellen mit $\Omega = 1$ und $\Omega < 1$ konnte ein Peak zugeordnet werden.

1.4. Simulationen des Hubble Volumens

Die ideale kosmologische Simulation würde das gesamte beobachtbare Universum enthalten mit einer sehr hohen Massenauflösung. Dies wäre insbesondere für das Studium sehr seltener Objekte, wie z.B. Galaxienhaufen, von Interesse. Im Rahmen dieser Arbeit wurden zwei Simulationen, die sog. Hubble–Simulationen, durchgeführt, die diesem Ideal relativ nahe kommen. Beide Simulationen enthalten einen signifikanten Bruchteil des gesamten beobachtbaren Universums und sind um mindestens eine Größenordnung größer als die nächste Generation von sehr umfangreichen Galaxienkatalogen. Damit wurde es zum ersten Mal möglich, Eigenschaften von Galaxienhaufen zu untersuchen, die bislang jenseits der Möglichkeiten von Simulationen lagen.

Abbildung 1.3 zeigt die differentielle Anzahldichte von massereichen Galaxienhaufen bei einer Rotverschiebung von $z = 0.78$. Die Anzahl der Beobachtungen solcher Haufen ist derzeit stark im Steigen begriffen. Drei dieser Objekte, für die es sehr genaue Messungen der Massen mithilfe ihres Gravitationslinseneffekts gibt, sind in Abbildung 1.3 gezeigt. Wie deut-
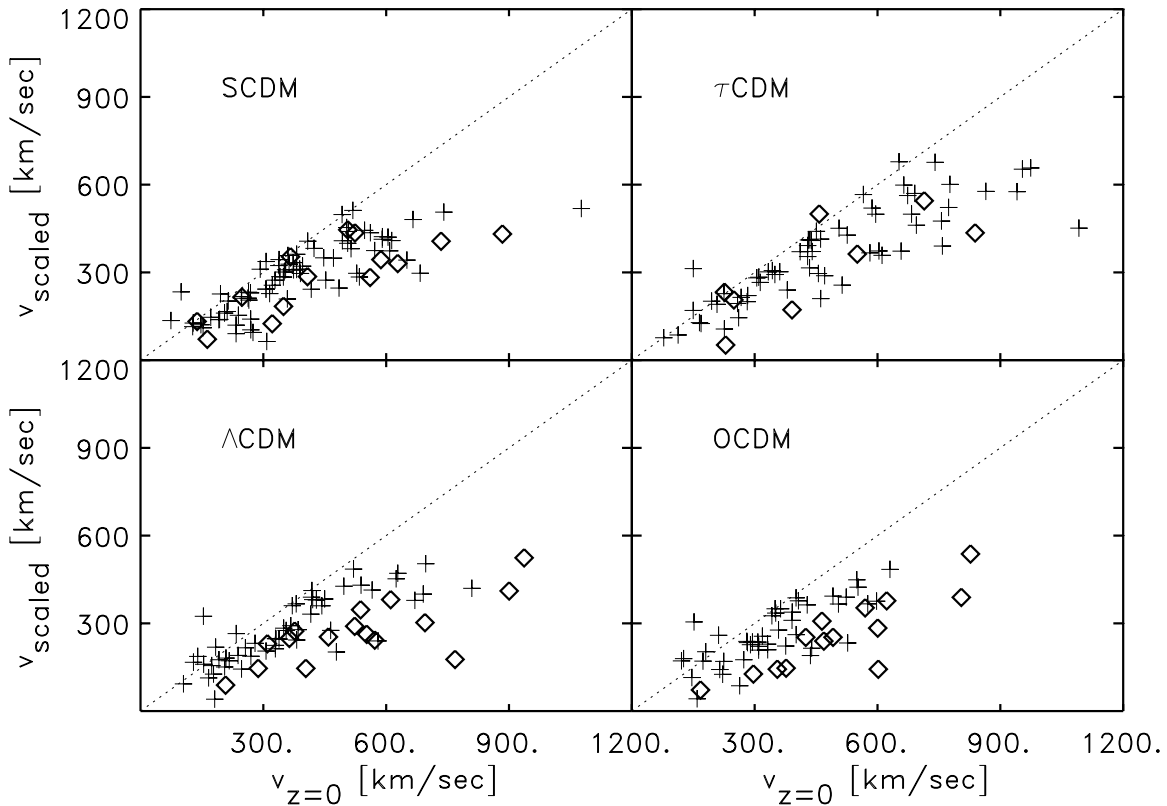
Abbildung 1.2.: Vergleich der Geschwindigkeiten der Galaxienhaufen zur heutigen Zeit ($v_{z=0}$) mit der auf die heutige Zeit hochskalierten Geschwindigkeit aus den Anfangsbedingungen (v_{scaled}). Galaxienhaufen, die einen benachbarten Haufen in einer maximalen Distanz von $10\,h^{-1}$Mpc haben, sind durch die Rauten kenntlich gemacht.

lich zu sehen ist, ist die τCDM–Simulation nicht in der Lage, solch massereiche Objekte zu bilden. Mit anderen Worten bildet sich Struktur in einem Universum mit $\Omega = 1$ viel zu spät. Das ΛCDM–Modell bildet mehr massereiche Galaxienhaufen bei $z = 0.78$, allerdings befindet sich ein beobachteter Haufen weit außerhalb der Verteilung. Derzeit sind die Bestimmungen der Massen solcher Haufen noch immer strittig, so daß es zum heutigen Zeitpunkt nicht angebracht erscheint, ein endgültiges Urteil über das ΛCDM–Modell zu fällen.

Abbildung 1.4 vergleicht die Massenfunktion der τCDM–Simulation mit der theoretischen Vorhersage des Press–Schechter–Modells. Die Simulation läßt sich in der Tat sehr gut mit diesem Modell beschreiben. Die Abweichungen, die in der Abbildung zu sehen sind, entsprechen denen, die bislang in kleineren Simulationen gefunden worden sind. Sie sind insofern kein Grund zur Sorge, als es *a priori* überhaupt keinen Grund gibt, warum das Press– Schechter–Modell die Massenfunktion überhaupt so gut beschreiben soll.

Von großem Interesse ist es, die räumliche Verteilung von Galaxienhaufen zu untersuchen. Wie oben bereits angedeutet, sind diese keineswegs gleichförmig verteilt, sondern sie ballen sich selbst zu Gruppen zusammen. Die Kataloge von Haufen, die aus den Hubble–
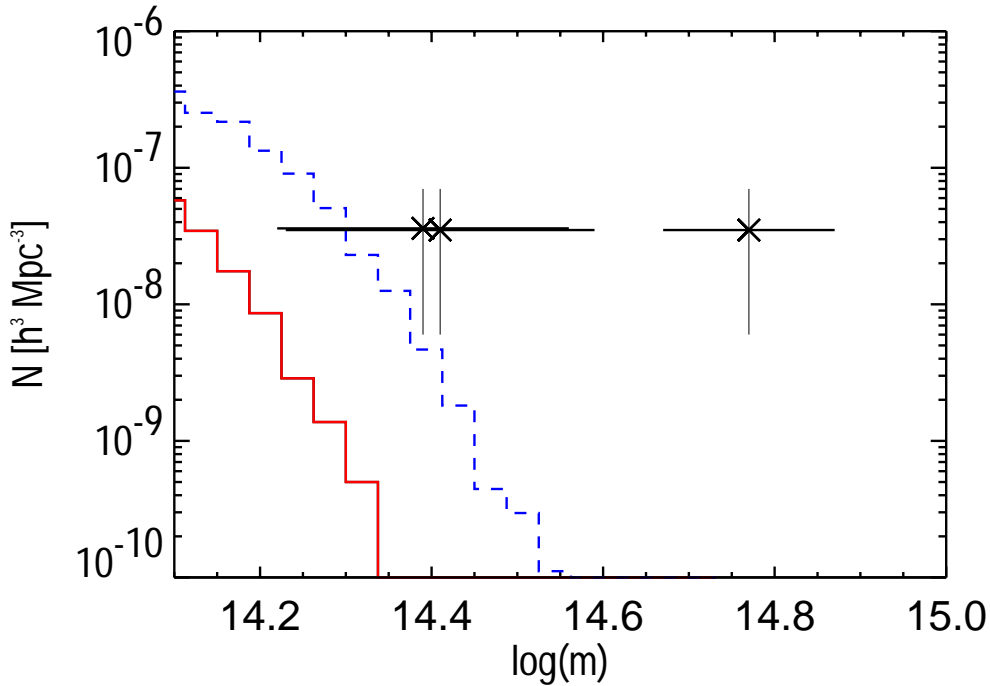
Abbildung 1.3.: Die differentielle Anzahldichte von Galaxienhaufen bei einer Rotver-
schiebung von $z = 0.78$ in der τCDM (durchgezogene Linie) und der ΛCDM
(gestrichelte Linie) Simulation. Die Massen sind innerhalb eines Radius von
$0.5\,\mathrm{Mpc}/h$ bestimmt worden. Die drei Meßpunkte geben drei beobachtete
Objekte im Universum wieder.

Simulationen erstellt wurden, sind ideal, um dies zu untersuchen. Hierzu wird die Zwei–
Punkt–Korrelationsfunktion, $\xi(r)$, benutzt. Für jeden Haufen gibt sie an, wieviel wahrschein-
licher es ist, bei einer Entfernung r einen zweiten zu finden, als wenn die Haufen poisson-
verteilt im Raume wären. Die Korrelationslänge, r_0, ist definiert über $\xi(r_0) = 1$. Da Gala-
xienhaufen im Universum so selten sind, ist es äußerst schwer, einen Katalog zu erstellen,
der vollständig ist. Üblicherweise sind Kataloge nur vollständig ab z.B. einer bestimmten
Röntgenleuchtkraft der Haufen. Deswegen wird die Korrelationsfunktion gemessen als Funk-
tion der Dichte, n_c, des Katalogs, der über $d_c = n_c^{-1/3}$ ein mittlerer Abstand der Haufen
entspricht. Die Abhängigkeit der Korrelationslänge von der Haufendichte ist derzeit noch um-
stritten, und erst mit den Hubble–Simulationen stehen ausreichend große simulierte Kataloge
zur Verfügung, um dies zu untersuchen.

Abbildung 1.5 zeigt die Korrelationslängen der Galaxienhaufen in der τCDM (Kästchen)
und der ΛCDM (Rauten) Simulation in Abhängigkeit der Dichten von Teilmengen der Kata-
loge. Ebenfalls gegeben sind für die beiden Modelle (gestrichelte und strichpunktierte Linie)
die Vorhersagen des Modells von Mo & White (1996). Dieses drückt die Korrelationsfunktion
der Haufen aus über

$$\xi(r) = b^2(R)\,\xi_{\mathrm{DM}}(r)\,, \tag{1.18}$$
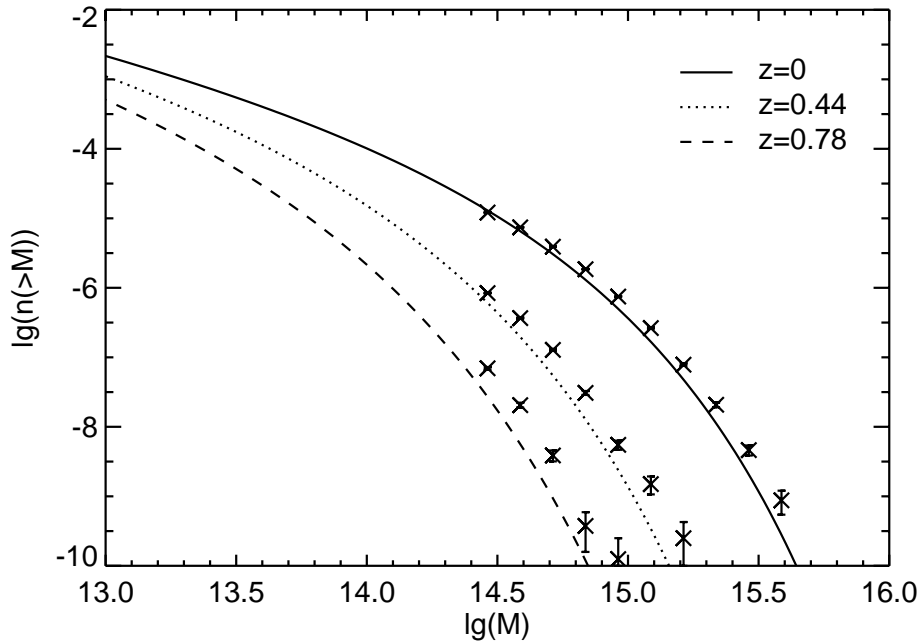
Abbildung 1.4.: Die kumulative Massenfunktion in der τCDM–Simulation (Kreuze) für drei verschiedene Rotverschiebungen. Die Kurven geben die theoretische Vorhersage wieder.

mit

$$b(R) = 1 + \frac{\delta_{\mathrm{c}}}{\sigma^2(R)} - \frac{1}{\delta_{\mathrm{c}}} \,. \tag{1.19}$$

Hierbei ist $\xi_{\mathrm{DM}}(r)$ die Korrelationsfunktion der Dunklen Materie, und $b(R)$ ist ein sogenannter Biasfaktor. Dieser bestimmt sich aus der Konstanten $\delta_{\mathrm{c}} = 1.69$ und aus dem Moment $\sigma^2(R)$ (entsprechend $j = 0$ in Gleichung 1.16). R ist wie oben der Radius, der der minimalen Haufenmasse entspricht. Ebenfalls abgebildet sind in Abbildung 1.5 ein linearer Zusammenhang zwischen der Korrelationslänge und der Haufendichte (gestrichelte Linie) und das Ergebnis der Analyse der Galaxienhaufen im APM–Katalog (Kreuze; Croft et al. 1997). Wie deutlich zu sehen ist, ist das lineare Modell nicht vereinbar mit den Vorhersagen der Modelle und der Messung. Die Theorie von Mo & White sagt zu große Korrelationslängen voraus, stimmt qualitativ aber mit den Ergebnissen aus der Simulation überein. Von den beiden Simulationen stimmt wieder nur die ΛCDM–Simulation mit der Messung überein.

Die Hubble–Simulationen haben sich also bereits im Rahmen dieser Arbeit als mächtige Werkzeuge erwiesen, um Modelle mit Beobachtungen zu vergleichen. Sie werden in der Zukunft von vielen Arbeitsgruppen benutzt werden, z.B. um detaillierte simulierte Galaxienkataloge zu erstellen und Vorhersagen für die nächsten großen beobachteten Galaxienkataloge zu erstellen.
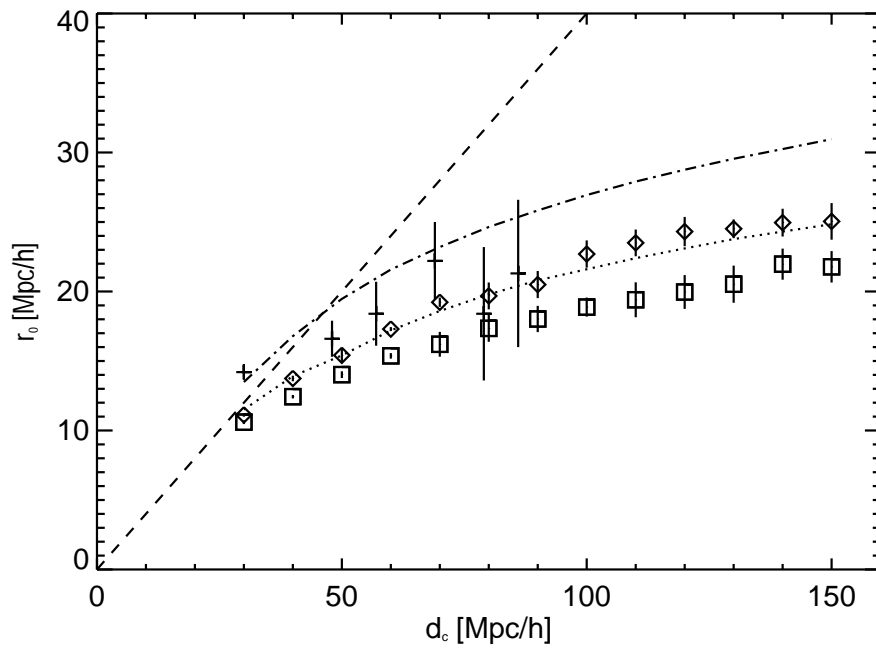
Abbildung 1.5.: Die Korrelationslänge der Galaxienhaufen in Abhängigkeit des mittleren Abstands der Haufen (mithin als Funktion der Dichte der Haufen). Die Boxen und Rauten sind die Ergebnisse aus der τCDM und der ΛCDM–Simulation. Die gestrichelte Linie entspricht einer linearen Abhängigkeit der beiden Größen. Die gepunktete und die Strich–Punkt–Linie zeigen die Vorhersage des analytischen Modells von Mo & White (1996). Kreuze mit Fehlerbalken sind Ergebnisse aus der Analyse der Haufen im APM–Katalog von Croft et al. (1997).

Bibliography

[1] Bond J.R., Efstathiou G., ApJ **285**, L45 (1984)

[2] Croft R.A.C., Dalton G.B., Efstathiou G., Sutherland W.J., Maddox S.J., astro-ph/9701040

[3] de Lapparent V., Geller M.J., Huchra J.P., ApJ, 302, L1 (1986)

[4] Davis M., Efstathiou G., Frenk C.S., White S.D.M., ApJ, 292, 371 (1985)

[5] Haynes M.P., Giovanelli R., ApJ, 306, L55 (1986)

[6] Mo H.J., White S.D.M., MNRAS, **282**, 347 (1996)

[7] White S.D.M., Frenk C.S., Davis M., ApJ **274**, L1 (1983)

Chapter 2

Introduction

C'est une maladie naturelle à l'homme de croire qu'il possède la vérité directement; et de là vient qu'il est toujours disposé à nier ce qui lui est incompréhensible.

Blaise Pascal

Over the last twenty years, cosmology has evolved from a rather speculative side branch of astrophysics and philosophy into a high precision science of its own. This is due to the fact that, recently, an amount of knowledge has been gained which is so large compared with what was known earlier that is probably not too much of an exaggeration to compare this process with the development of quantum mechanics and its subsequent revolution of atomic physics in the early decades of the 20th century.

Observationally, new technology in the form of satellites and telescopes and also new techniques in order to study objects have arisen which have revolutionized our understanding of the Universe. For instance, the Cosmic Microwave Background Explorer (COBE) satellite has measured the afterglow of the Big Bang with a precision undreamt of before. It shows that the Microwave Background (CMB) has a nearly *perfect* black body spectrum and that there must have been fluctuations of the order of 10^{-5} in temperature (and thus in density) in the very early Universe. The Hubble Space Telescope (HST) has widened the view of not only cosmology, but of the whole field of astrophysics. Combined with new ground based telescopes like for the Keck, galaxies at a redshift of five, that is, at a time when the Universe had only a sixth of its current age and size, can now be found. The existence of Dark Matter in galaxy clusters can be observed by means of gravitational lensing. This very short list gives only a few highlights of the new data which theories about the birth of the Universe and the subsequent formation and evolution of galaxies and Large–Scale Structure have to explain.

On the theoretical side, the data gained with new observational instruments and techniques allow high precision tests of existing theories. High precision *predictions* for some of the theories have also been developed. While the simplest theories have failed to be good models

for the Universe, some of them are not very wrong. So theoreticians have to start fine tuning their models – something unknown to the field before. Computer simulations have played a major rôle in this process. This is not only due to the truly gigantic increase in computational power over the last decades. For instance, the Hot Dark Matter model, which assumes that the dominant (and unseen) mass component in the Universe consists of massive neutrinos[1], was rejected on the basis of a simulation with only 1000 particles (White et al. 1983). The seminal simulation work of Marc Davis, George Efstathiou, Carlos Frenk, and Simon White in 1985 (DEFW hereafter) with 32^3 Cold Dark Matter particles contains results which are still valid today. However, larger simulations are still needed to increase the predictive power of the theories. Larger regions of the Universe have to be simulated with a higher mass resolution to test cosmological models further.

This work is about some of these high precision simulations. In the remaining sections of this Chapter, the basic theoretical foundations will be laid. Section 2.1 briefly describes the set of fundamental cosmological equations and variables used throughout the whole work. Section 2.2 gives an overview of the growth of perturbations. Finally, section 2.3 contains an introduction into the family of Cold Dark Matter models used in the simulations themselves.

Chapters 3 and 8 contains the technical part of this work. They describe some details of the computers, the codes used, and the simulations themselves.

In Chapter 4, the large–scale distribution of the mass in the simulations is studied. The density field, smoothed on suitable large scales, is investigated as a function of the mass above an overdensity threshold.

Chapter 5 contains a study of the most massive objects in the simulations. These are identified similarly to how observers find galaxy clusters. The main point of the Chapter is to determine if peculiar velocities of galaxy clusters can be predicted accurately. To this end, the correspondance between peaks in the smoothed initial density field and clusters is studied.

In Chapter 6, the Hubble Volume Simulations are introduced. These represent the biggest effort in computational cosmology to date and will be the basis for predictions for the next generation of very large galaxy surveys. Catalogs of galaxy clusters which each contain hundreds of thousands of clusters are extracted and used to study the existence of massive objects at high redshifts and the mass function itself (section 6.3), and cluster correlation functions (section 6.4).

Chapter 7 links the themes of the earlier Chapters. It shows how the formation process of galaxy clusters is linked to the mass distribution around the clusters, that is, to Large–Scale Structure itself. Finally, Chapter 9 contains a summary of this thesis.

---

[1]In the context of astrophysics and cosmology, "massive" usually means a few eV.

2.1. Basic Cosmology

> *Hüten wir uns, zu sagen, daß es Gesetze in der Natur gebe. Es gibt nur Notwendigkeiten: da ist keiner, der befiehlt, keiner, der gehorcht, keiner, der übertritt. Wenn ihr wißt, daß es keine Zwecke gibt, so wißt ihr auch, daß es keinen Zufall gibt: denn nur in einer Welt von Zwecken hat das Wort "Zufall" einen Sinn.*
> Friedrich Nietzsche,
> Die Fröhliche Wissenschaft, III, 109

The Big Bang as the origin of the Universe is now a well–established theory. According to this theory, at some time in the distant past, space and time originated from the expansion of a tiny region. In this section, it is assumed that the result of this process is a Universe which is smooth and homogeneous on very large scales. This implies that the Universe essentially looks the same at all spatial locations, there is no preferred region in the Universe – something called the "Copernican Principle". The theory which describes the dynamics of the gravitational field is Einstein's theory of General Relativity. The spacetime metric for such a Universe is the Friedmann–Robertson–Walker (FWR) metric[2]

$$ds^2 = (cdt)^2 - a^2(t)\left[\frac{dr^2}{1 - kr^2} + r^2(d\vartheta^2 + \sin^2\vartheta d\phi^2)\right].\tag{2.1}$$

Here, $a(t)$, the so–called expansion factor, and k are determined using Einstein's equation. k may take three different values, namely $k = 1, 0$, and -1 for positive, zero, and negative curvatures of spatial hypersurfaces, respectively. The time dependance of a implies that any proper distance scale $l(t)$ is proportional to it

$$l(t) \propto a(t).\tag{2.2}$$

This implies that electromagnetic radiation will change its frequency as it travels across the Universe. As $\dot{a} > 0$, an observer will receive spectra from distant objects which are reddened. If the observed and emitted frequencies are named ω_0 and ω_e, respectively, then the redshift z is be defined via

$$\frac{\omega_e}{\omega_0} = \frac{1}{a(t_e)} \equiv 1 + z,\tag{2.3}$$

where t_e denotes the time of emission, and $a(t)$ has been normalized such that it is unity today, i.e. $a(t_0) = 1$.

As indicated above, $a(t)$ and k can be computed from Einstein's equations

$$G^\alpha_\beta = 8\pi G T^\alpha_\beta,\tag{2.4}$$

---

[2]The following discussion can be found in most textbooks on cosmology, e.g. Padmanabhan 1993. Note, that $c = 1$ here.

if the stress–tensor T for the source of the gravitational field is given. Matter is usually treated as a perfect fluid which is specified by a pressure p and a density ρ. Using the FRW metric (2.1) and the assumption of homogeneity and isotropy (which makes all non–diagonal elements of T vanish) then yields two independent equations, viz.[3]

$$\frac{\dot{a}^2 + k}{a^2} = \frac{8\pi G}{3}\rho\,,\tag{2.5}$$

$$\frac{2\ddot{a}}{a} + \frac{\dot{a}^2 + k}{a^2} = -8\pi G p\,.\tag{2.6}$$

The overdot denotes differentiation with respect to time. $a(t), \rho(t)$, and $p(t)$ are fully specified once the equation of state $p = p(\rho)$ is given. Using the following three abbreviations

$$H_0 \equiv \left(\frac{\dot{a}}{a}\right)_{t=t_0}\tag{2.7}$$

$$\rho_c \equiv \frac{3H_0^2}{8\pi G}\tag{2.8}$$

$$\Omega_0 \equiv \frac{\rho_0}{\rho_c}\tag{2.9}$$

yields that at present epoch

$$k = H_0^2(\Omega_0 - 1)\,.\tag{2.10}$$

H_0 is called the Hubble constant at present time, ρ_c is the critical density, and Ω_0 is the density parameter. From equation (2.10) it is obvious that these parameters determine the curvature of the Universe. $\Omega_0 = 1$ gives a flat Universe.

Combining equations (2.5) and (2.6) gives

$$\frac{\ddot{a}}{a} = -\frac{4\pi G}{3}(\rho + 3p)\,,\tag{2.11}$$

which implies that $\ddot{a} < 0$ for ordinary kinds of matter, which have $(\rho + 3p) > 0$. a thus is smaller in the past and will become zero at some finite time in the past (Big Bang). Integration yields the age of the Universe:

$$t_0 = \frac{2}{3}\frac{1}{H_0}f(\Omega_0)\,,\tag{2.12}$$

where $f(\Omega_0) = 1$ for $\Omega_0 = 1$ and $f(\Omega_0) > 1$ for $\Omega_0 < 1$. Furthermore, one can show that for $\Omega_0 = 1$

$$a \propto t^{1/2}\tag{2.13}$$

$$a \propto t^{2/3}\tag{2.14}$$

for the radiation–dominated and matter–dominated phases of the Universe, respectively[4]. Generally, the equations are easy to solve analytically for $\Omega_0 = 1$ and need to be done numerically otherwise.

---

[3] $c = 1$ has been set here.

[4] The Universe is called radiation (matter) dominated when the energy density of radiation (matter) dominates. Then, $p = \rho/3$ ($p \simeq 0$).

A further concept has to be introduced here. The source term for Einstein's equations (2.4) can be any conserved stress–tensor. In particular, one can take

$$T_k^i = \Lambda \delta_k^i \,, \tag{2.15}$$

where Λ is the so–called Cosmological Constant postulated, and later abandoned, by Einstein. He originally wanted to have a stable, i.e. non–expanding Universe, but quite obviously this doesn't work because small fluctuations around the "stable" state would result in an immediate collapse (or in an immediate expansion). Λ corresponds to an equation of state $p = -\rho = -\Lambda$. By noting its contribution to the density in the Universe

$$\Lambda_0 = \frac{8\pi G \Lambda}{3H_0^2} \tag{2.16}$$

one can take this as the vacuum energy density. Crudely speaking, Λ doesn't change the expansion of the Universe at early times. At later times it starts to accelerate the expansion. The age of the Universe is increased relative to a Universe with $\Omega_0 = 1$. A non–vanishing Λ is embarrassing because there is no good physical explanation for its existence and no convincing explanation why it should have the value favoured by some cosmologists (for further discussion see section 2.3.5).

2.2. The Growth of Perturbations

In the preceding section, it was assumed that at early times the Universe was smooth and homogeneous on large scales. From the fact that e.g. galaxies exist today it is obvious that it can not be smooth and homogeneous on small scales. Deviations from homogeneity must have existed in the early Universe from which all objects seen today must have formed. Objects in the gravitational instability scenario formed from the collapse of overdense regions. COBE does indeed find such fluctuations on the Microwave Sky, they are small ($\delta T/T \approx 10^{-5}$), but nevertheless they must have been big enough to cause the collapse of structure.

Consider a pressureless fluid with density ρ and velocity $\mathbf{v}$ under the influence of a gravitational field with potential Φ[5]. The equations which describe this fluid are

$$\frac{\partial \rho}{\partial t} + \nabla \cdot (\rho \mathbf{v}) \;=\; 0\,, \qquad \text{(continuity)} \tag{2.17}$$

$$\frac{\partial \mathbf{v}}{\partial t} + (\mathbf{v} \cdot \nabla)\mathbf{v} \;=\; -\nabla\Phi\,, \quad \text{(Euler)} \tag{2.18}$$

$$\nabla^2 \Phi \;=\; 4\pi\, G\, \rho\,. \quad \text{(Poisson)} \tag{2.19}$$

These equations can be cast into a cosmological context by using appropriate variables. These are a comoving position $\mathbf{x} = \mathbf{r}/a$, which is fixed for an observer moving with the Hubble expansion, and the corresponding peculiar velocity $\mathbf{u} = a\, d\mathbf{x}/dt$, representing departures of the matter motion from pure Hubble expansion.

---

[5]This section follows Efstathiou (1990a).

Assume the density is spatially variable

$$\rho(\mathbf{x}, t) = \bar{\rho}(t) \cdot (1 + \delta(\mathbf{x}, t)). \tag{2.20}$$

Then equations (2.17) to (2.19) can be transformed from the coordinate system $\mathbf{r}$ to $\mathbf{x}$ which gives

$$\frac{\partial \delta}{\partial t} + \nabla \cdot \mathbf{u} + \nabla \cdot (\mathbf{u}\delta) = 0, \tag{2.21}$$

$$\frac{\partial \mathbf{u}}{\partial t} + (\mathbf{u} \cdot \nabla)\mathbf{u} + 2\frac{\dot{a}}{a}\mathbf{u} = -\nabla \Phi / a^2, \tag{2.22}$$

$$\nabla^2 \Phi / a^2 = 4\pi G \bar{\rho} \delta. \tag{2.23}$$

In these equations, ∇ and the overdot now denote differentiation w.r.t. $\mathbf{x}$ and time, respectively.

Perturbations in the early Universe must have been small. One can thus combine equations (2.21) to (2.23) and neglect all non–linear terms to get

$$\ddot{\delta} + 2\frac{\dot{a}}{a}\dot{\delta} - 4\pi G \bar{\rho} \delta = 0. \tag{2.24}$$

For $\Omega_0 = 1$, equation (2.24) can be solved easily. In this case, $a \propto t^{2/3}$, which gives

$$\ddot{\delta} + \frac{4}{3t}\dot{\delta} - \frac{2}{3t^2}\delta = 0. \tag{2.25}$$

Obvious solutions for equation (2.25) are

$$\delta \propto D(t) \propto t^{2/3} \propto a \quad \text{(growing mode)} \tag{2.26}$$

$$\propto a^{-3/2} \quad \text{(decaying mode)} \tag{2.27}$$

$D(t)$ is the so–called growth factor of fluctuations. For $\Omega_0 < 1$, the solution is more complicated. It can be shown that at early times when $\Omega \approx 1$ the decaying and growing mode behave as in the case where $\Omega_0 = 1$. At late times, when $\Omega < 1$, the growing mode starts to saturate and structure ceases to grow.

The growth of peculiar velocities is studied in Chapter 5. After some algebra, the equations above show that the peculiar velocity of every mass element grows as

$$\mathbf{v} \propto a\dot{D}. \tag{2.28}$$

According to Heath (1977), the growth factor for a general cosmology is given by

$$D = H_0^{-2} X^{1/2} a^{-1} \int_0^a X^{-3/2} \mathrm{d}\tilde{a}, \tag{2.29}$$

where $X \equiv 1 + \Omega_0(a^{-1} - 1) + \Lambda_0(a^2 - 1)$. The subscript "0" now explicitly refers to the values of the density parameter and the cosmological constant at the present time. A number of accurate approximate forms are known for the relations between D and a. $\dot{D}$ can be re–written as follows

$$\dot{D} \equiv \frac{\mathrm{d}D}{\mathrm{d}t} = \frac{\mathrm{d}D}{\mathrm{d}a}\frac{\mathrm{d}a}{\mathrm{d}t}, \tag{2.30}$$

where $\mathrm{d}a/\mathrm{d}t$ can be substituted from the Friedmann equation. Lahav et al. (1991) give an approximation for $\mathrm{d}D/\mathrm{d}a$:

$$f(a) \equiv \frac{\mathrm{d}D}{\mathrm{d}a}\frac{a}{D} \approx \left(\frac{\Omega_0 \, a^{-3}}{\Omega_0 a^{-3} + (1 - \Omega_0 - \Lambda_0)a^{-2} + \Lambda_0}\right)^{0.6} . \tag{2.31}$$

For $a = 1$ this gives the standard factor $f \approx \Omega_0^{0.6}$ which appears when predicting the peculiar velocities produced by a given overdensity field. Carroll et al. (1992) used this result to derive an approximation for $D(a)$ itself,

$$D \approx ag(a) , \tag{2.32}$$

where

$$g(a) = \frac{5}{2}\frac{\Omega(a)}{\Omega^{4/7}(a) - \Lambda(a) + \left(1 + \frac{\Omega(a)}{2}\right)\left(1 + \frac{\Lambda(a)}{70}\right)} \tag{2.33}$$

with

$$\Omega(a) \equiv \frac{\Omega_0}{a + \Omega_0(1 - a) + \Lambda_0(a^3 - a)} , \tag{2.34}$$

$$\Lambda(a) \equiv \frac{\Lambda_0 a^3}{a + \Omega_0(1 - a) + \Lambda_0(a^3 - a)} . \tag{2.35}$$

Combining these equations, yields an explicit approximation for the growth of peculiar velocities:

$$\mathbf{v} \propto f(a)g(a)a^2 \sqrt{\Omega_0 a^{-3} + (1 - \Omega_0 - \Lambda_0)a^{-2} + \Lambda_0} . \tag{2.36}$$

For the simple case where $\Omega_0 = 1$ and $\Lambda_0 = 0$, these formulae reduce to the exact results $D = a \propto t^{2/3}$ and $\mathbf{v} \propto \sqrt{a}$.

2.3. The Cold Dark Matter Model

2.3.1. Introduction

According to the standard theory in cosmology described above, the Universe was born in the Big Bang, i.e. it was hot, dense, and homogeneous in the beginning, from whence it expanded adiabatically according to the laws of General Relativity. However, this picture is incomplete, for it does not explain why on small scales, say a few Megaparsecs (Mpc), matter is clumpy and not distributed homogeneously. In addition, evidence is growing that the amount of matter which emits electromagnetic radiation and thus can be seen in the Universe, is far less than the amount of matter which must be there. The visible matter can only account for a small fraction of the total mass: Dark Matter shows up via its gravitational influence on various scales.

In the following, various concepts are added to the standard model. In section 2.3.2, the idea of Cold Dark Matter is motivated. This is the missing matter component. Inflation, as a well studied mechanism to account for density fluctuations in the early Universe, is introduced in section 2.3.3. section 2.3.4 discusses the amplitude of the initial fluctuation spectrum. Finally, section 2.3.5 describes four cosmological models which are based on the preceeding hypotheses and which have been simulated using large N–body simulations (c.f. Chapter 3).

2.3.2. Dark Matter

Why Dark Matter?

Evidence for the existence of matter which does not emit electromagnetic radiation at any wavelength and which only shows up via the influence of its gravity (Dark Matter) comes from different scales:

Scales of galaxies (a few ten kpc): The rotation curves of spiral galaxies, i.e. the rotation speed as a function of the distance from the galactic center, are flat at large distances, contrary to the prediction of Kepler's law which would give a decreasing rotation speed for the visible matter. However, if a spherically distributed Dark Matter component is added, which is larger than the disk itself, a so–called halo, the observed rotation curve for radii larger than a few kpc is dominated by the halo and can be flat.

Scales of galaxy clusters (a few Mpc): The relative amount of Dark Matter is greater for galaxy clusters[6]. The total mass of a galaxy cluster can be found either by using the galaxies as test particles in the system's potential and deducing the mass from their velocities, by converting the X–ray emission of the hot intracluster gas into a mass estimate, or by means of gravitational lensing where the deflected light of background galaxies is used to infer the mass of the cluster. The latter method is free of assumptions (whereas the former two assume virial equilibrium which is not necessarily true). However, it measures the projected mass which could be contaminated by objects lying behind or in front of clusters. The methods agree relatively well for a large sample of clusters and if one compares the total mass with the mass of the baryons (which is believed to mainly consist of the galaxies themselves plus the hot intracluster gas) one finds that the baryon fraction is around 10 to 20% (White et al. 1993a).

Very large scales (tens of Mpc): The assumption that galaxies may be treated as test particles allows a reconstruction of the cosmic velocity field from which the potential of the underlying mass distribution can be deduced. Using Poisson's equation then gives the density field which can be compared to the observed density field of the galaxies. From this procedure, evidence is mounting that not only is the visible mass just a small fraction of the total mass, but that the total mass may be close to the critical amount required to make the Universe flat, i.e. $\Omega_0 = 1$ (e.g. Dekel 1994).

These observations directly lead to the question:

What is the Dark Matter?

The simplest approach to solve the Dark Matter problem is to assume that the Dark Matter is the same type of matter as that which has already been seen, i.e. baryons. Objects which consist of baryons but do emit little if any light are well known: they include for instance brown dwarfs.

---

[6]The uusal way of expressing this is to give the ratio of the mass of and the light emitted by an object, the so–called mass–to–light–ratio M/L. Typical values are $M/L \approx 30 M_\odot / L_\odot$ and $M/L \approx 300 M_\odot / L_\odot$ for galaxies and galaxy clusters, respectively, where $M_\odot$ and $L_\odot$ denote the sun's mass and luminosity, respectively.

However, a strong upper and lower limit on the amount of baryons in the Universe comes from Primordial Nucleosynthesis. According to this theory,

$$0.009 \, h^{-2} \leq \Omega_b \leq 0.02 \, h^{-2} \tag{2.37}$$

which is inferred from measured abundances of light elements (e.g. Copi et al. 1995). Hence, unless a severe error in these computations and measurements shows up, the Dark Matter can not consist of ordinary baryons unless Ω_0 is very small.

Almost all remaining Dark Matter candidates have one thing in common: They are elementary particles. Usually they are classified according to their speed when galaxy–sized fluctuations entered the horizon. Particles which were relativistic (non–relativistic) at that time are named Hot (Cold) Dark Matter.

Hot Dark Matter is probably the most straightforward solution for the Dark Matter problem, simply because neutrinos with a non–vanishing mass would have been relativistic when they decoupled from the rest of the matter in the Universe. In addition, neutrinos are known to exist. However, their masses are unknown. The mass of a neutrino must not be larger than about $30 \, \mathrm{eV}$ – otherwise neutrinos would overclose the Universe. Although the neutrino masses are not known, it is already clear that neutrinos can not be the dominating Dark Matter component[7]. If $\Omega_\nu \approx 1$ then the free streaming of the neutrinos would have destroyed any adiabatic density fluctuation smaller than the size of superclusters ($\approx 10^{15} \, M_\odot$) in the early Universe (Bond et al. 1980). As a consequence, structure would have formed in a so–called top–down scenario, with superclusters forming first and galaxies forming only at the present epoch. As high redshift galaxies are have been observed, this model cannot explain the formation of structure in the Universe. In addition, this model is incompatible with the fluctuations in the CMB.

As a consequence of the above, Cold Dark Matter (CDM) remains the best Dark Matter candidate. There are no known (i.e. detected) elementary particles which could be CDM. However, the list of postulated CDM particles is long. Most of these particles are either Weakly Interacting Massive Particles (WIMPs). There are two reasons why one should not worry about the fact that neither of these types of particles has been detected yet. First, the neutrino itself was postulated by Wolfgang Pauli long before it was detected – which shows that postulating particles on a solid physical ground is much more than science fiction. And second, particle physicists themselves are thinking of elementary particles beyond the standard model of particle physics; the masses of some of these particles fit nicely into the cosmological mass estimates.

Whatever CDM actually consists of, the important point is that, from the viewpoint of cosmology, there is a need for these particles, which are well motivated within almost all extensions of the standard model of particle physics. Thus, one of the main hypotheses of this work is that Dark Matter consists entirely of CDM[8].

---

[7] This holds if the density fluctuations were generated during inflation. Hot Dark Matter could work in the context of string cosmologies but this is beyond the scope of this work.

[8] It may be argued that there may be a small contribution of Hot Dark Matter if $\Omega_0 = 1$. For details on the so–called Mixed Dark Matter Models (or CHDM with the H standing for Hot) c.f. e.g. Primack (1997).

2.3.3.   Inflation as the Origin of Fluctuations

Introduction

Currently, there are two competing scenarios for the generation of density fluctuations needed to trigger gravitational collapse. These are Inflation and Topological Defects. Due to its complexity, the latter is neither as well understood nor has it been investigated in as much detail as the former. As Inflation is taken as the scenario which generates density fluctuations, Cosmic Defects are not discussed here.

Inflation

The first and very simple question is: Why would there be density fluctuations at all after the Big Bang? Suppose one assumes that there must have been some fluctuations because this is the only way to explain why the Universe is not completely homogeneous on small scales but contains galaxies, galaxy clusters, and voids. Then the next question that arises is: If causality holds, how can the temperature variation of the CMB be only about $\Delta T/T \approx 10^{-5}$ from regions on the sky which were causally disconnected at recombination? And why is the Universe so close to being flat, i.e. why is $\Omega_{\rm tot} \approx 1$ (neglecting for the moment the debate about its actual value)? In addition, after the phase transition in the very early Universe (symmetry breaking) a huge number of topological defects such as monopoles should have been created; why is the density in these monopoles so low today? In addition, one may wonder what the details of the density fluctuations are? How can they be described in a statistical sense, i.e. what does the density fluctuation spectrum look like? Inflation provides answers to all these questions in a rather simple fashion which allows one to connect the measurements of the CMB with detailed models.

In spontaneously broken gauge theories which are used to describe the state of the very early Universe, the vacuum energy plays a very important role. It can be described as an cosmological constant. The idea, first proposed by Guth (1981), is to let this vacuum energy inflate a single causally connected region in a de Sitter–like cosmology to a gigantic scale.

Consider a very simple universe which could look like this: It is empty (i.e. $\rho = 0$), has a vanishing curvature ($k = 0$), and a positive cosmological constant ($\Lambda > 0$) – the de Sitter cosmology. The solution of Friedmann's equation is then simply

$$a = a_0 \exp[Ht] , \tag{2.38}$$

where the Hubble parameter is constant $H = \sqrt{\Lambda/3}$. Thus, this universe would expand exponentially due to the effective pressure of space time itself which is described by Λ.

It can be shown that this period of inflation not only solves the flatness problem, in addition $\Omega_{\rm tot} = 1$ is nearly inevitable – some extra work is required to allow an open cosmological model with $\Omega_{\rm tot} < 1$ (c.f. Turok & Hawking 1998). The monopole problem is also solved because the enormous expansion of a small region reduces their number density drastically.

Inflation itself is controlled by the potential of a scalar field ϕ (inflaton field). As mentioned above, the vacuum energy of ϕ drives inflation. Quantum fluctuations in ϕ give rise to the density fluctuation needed for the gravitational collapse scenario later on. The fluctuations in ϕ

of different regions of the same size complete the phase transition to the Friedmann phase at different times. This time spread $\Delta t \approx \delta\phi/\dot\phi$ can be obtained from the equation of motion of ϕ (which is the free Klein–Gordon equation in an expanding universe) and it is directly connected to the density fluctuations $\delta_H = \delta\rho/\rho \propto H\Delta t$. Now the assumptions which have to be made for the inflaton field (essentially inflation has to last long enough in order to achieve its goals – the so–called slow roll approximation – so that the potential must not vary much) yield δ_H =constant. Thus, inflation predicts a constant curvature spectrum δ_H =constant of adiabatic fluctuations (known as Zel'dovich spectrum). In addition, the quantum fluctuations in ϕ have random phases and therefore are Gaussian.

It should be noted again that newer variants of inflation manage to result in $\Omega_{\rm tot} < 1$, too. This may be important because it is not yet clear that $\Omega_{\rm tot} = 1$. So inflation not only solves some nasty problems but predicts the spectrum of density fluctuations to be $P(k) \propto k$. One of the disadvantages it has is that it cannot *uniquely* predict the amplitude of the fluctuations. There are many variants of inflation each having different choices of ϕ. They vary in different aspects and some of them produce results which are unlikely to be testable. However, they all have the above features in common and all yield different amplitudes. This leads to the question of how this amplitude can be determined from observations.

2.3.4. The Fluctuation Spectrum and the Amplitude of Mass Fluctuations

In addition to the generation of the primordial spectrum of density fluctuations a second physical process must be taken into account. Small scale density pertubations (with $\lambda < \lambda_{\rm eq}$) enter the horizon prior to the epoch of equivalence between matter and relativistic particles ($\lambda_{\rm eq} \approx 13/\Omega_0 h^2$ Mpc is the comoving horizon scale at that epoch). They are damped and the spectrum develops a bend at the scale $\lambda_{\rm eq}$. The processes which change the shape of the primordial fluctuation spectrum are usually combined in the so–called transfer function $T(k)$ which relates the primordial spectrum to the actual spectrum through:

$$P(k) = T^2(k)P_p(k)\,, \tag{2.39}$$

where $P_p(k)$ now denotes the primordial spectrum and $P(k)$ the actual one.

The parametric form for $T(k)$ used in this work was introduced by Bond & Efstathiou (1984). In their notation, the power spectrum is given by

$$P(k) = \frac{Ak}{(1 + [ak/\Gamma + (bk/\Gamma)^{3/2} + (ck/\Gamma)^2]^\nu)^{2/\nu}}\,, \tag{2.40}$$

where $a = 6.4\,h^{-1}\,{\rm Mpc}$, $b = 3.0\,h^{-1}\,{\rm Mpc}$, $c = 1.7\,h^{-1}\,{\rm Mpc}$, and $\nu = 1.13$. A is the yet unknown normalization and Γ gives the typical scale of the spectrum. This is $\Gamma = \Omega_0 h$ for all pure CDM models (for a CDM model which deviates from this see section 2.3.5).

As discussed above, the amplitude A of the power spectrum cannot be predicted uniquely from inflationary models. Thus, it has to be obtained from measurements. This can be done in two different ways, either by using the CMB measurements of the COBE satellite (as explained in Efstathiou et al. (1992), see also Bunn et al. 1995), or by relating it to the *rms* linear

fluctuations in the mass distribution on scales of $8\,h^{-1}$ Mpc, σ_8, defined by

$$\sigma_8^2 \equiv \frac{1}{(2\pi)^3} \int P(k,\Gamma) \left(\frac{3}{kR_8} j_1(kR_8)\right)^2 d^3k \,, \tag{2.41}$$

where $R_8 = 8\,h^{-1}$ Mpc, and j_1 is a spherical Bessel function.

COBE has an angular resolution of about $7°$ which corresponds to scales much larger than any scale of interest in current cosmological investigations and simulations. Hence, a model which links these scales to much smaller ones is needed. This cannot be done unambiguously. For example, the amount of gravitational waves is still uncertain in inflationary scenarios. This could change A dramatically. Obtaining values for A from the mass distribution on cluster scales does not suffer from this problem. The basic idea behind this is rather simple: The mass function, that is the number of objects of some mass as a function of mass, is falling very steeply at its high mass end, i.e. high mass objects like rich clusters of galaxies are very rare (compare Chapter 6). As the mass function itself depends on the amplitude of fluctuations, the overall amplitude A of the power spectrum can be fixed by matching the observed abundance of rich clusters in computer simulations.

Values for σ_8 can be obtained by using either the mass (White et al. 1993b) or the X–ray temperature functions (Eke et al. 1996, Viana & Liddle 1996) of rich clusters. The different studies carried out this way more or less agree that

$$\sigma_8 \approx 0.6\,\Omega_0^{-0.6} \,. \tag{2.42}$$

2.3.5. Cold Dark Matter Models

> Die Welt ist unabhängig von meinem Willen.
>
> Ludwig Wittgenstein
> Tractatus logico–philosophicus 6.373

In the following, the four models used in the VIRGO simulations will be introduced. In addition, some of their features will be discussed. A concluding section summarizes the present *status quo* of measurements of the density parameter Ω_0. Despite several indications at this time no decisive point can be made whether or not the density parameter is unity or smaller than unity.

SCDM

In principle, the simplest cosmological model, named Standard CDM (SCDM), is a no parameter model where all quantities are fixed either from the predictions of inflation or from measurements. These are $n = 1$, $\Omega_0 = 1$, and $h = 0.5$[9]. h cannot be chosen to be larger because otherwise the age of the Universe would be smaller than the age of the oldest stars. This is still very uncertain, though. For a recent review of determinations of the Hubble Constant c.f. Branch (1998). As introduced above, SCDM has $\Gamma = \Omega_0 h = 0.5$.

---

[9]The Hubble constant is usually expressed as $H_0 = 100\,h$ km/sec/Mpc.

Nowadays, it has become *en vogue* to state that the SCDM model does not work and that it has to be substituted by some variant. But SCDM in most cases is wrong only by a factor of two or so – which is rather small compared with the usual uncertainties in astrophysics/cosmology.

So what actually is wrong with SCDM? As already stated in section 2.3.4, the normalizations obtained by COBE and via clusters disagree strongly. The amount of small scale power relative to large scale power is too large. Thus, if normalized to COBE, SCDM predicts too high an abundance of galaxy clusters. If normalized to give the correct abundance of clusters, the correlation function is too steep (Davis et al. 1985, Jenkins et al. 1998) and COBE fluctuations are underpredicted. Problems like this show up in many other topics (galaxy–galaxy and cluster–cluster correlation functions (Bahcall & Cen 1992, Efstathiou et al. 1990), genus statistics (Springel et al. 1997) to name just a few. For a detailed discussion of this topic c.f. Ostriker 1993). Probably the simplest way to understand why SCDM has these problems is its typical scale, specified by $\Gamma = 0.5$. On the basis of galaxy clustering, Peacock & Dodds (1994) found $\Gamma \approx 0.25$. Thus, the power spectrum of SCDM has a peak which is at too large a wave number. From this it is clear why the above normalization problems show up.

τ**CDM**

As indicated above, $\Gamma \approx 0.25$ is needed to match the clustering statistics of galaxies and galaxy clusters. For a model with $\Omega_0 = 1$ this cannot be easily achieved without invoking additional physics because the obvious solution, to lower the Hubble constant to $h = 0.25$, is in conflict with observational limits (Bartlett et al. 1995). One possibility is to assume that massive neutrinos which existed in the early Universe have now decayed into other neutrinos. The τ neutrino is a candidate for such a particle, hence the name of the model. A decaying neutrino species leads to an enhancement of the content of relativistic particles in the Universe. This changes the power spectrum of density fluctuations. In any model without such a decay process, the early Universe is radiation dominated, but matter starts to dominate later because the densities of radiation and matter scale differently with a. In the τCDM model this process is changed as follows. In the early stages of the Universe the energy density of the massive neutrinos is the same as that of a massless species. As the Universe expands, the massive neutrinos become nonrelativistic, and their energy density starts to increase relative to their massless counterparts. This leads to an epoch in which the density of the Universe is dominated by massive neutrinos. Later, they decay, and their rest energy is converted into energy for relativistic particles – thereafter the Universe starts to evolve like a SCDM Universe, but with a higher energy density in relativistic particles which causes equipartition to occur later hence reducing Γ.

The shape parameter Γ of the power spectrum can be expressed as follows (Bardeen et al. 1986):

$$\Gamma \simeq \Omega_{m0} h \times \left(\frac{\Omega_{r0} h^2}{4.18 \cdot 10^{-5}} \right)^{-1/2} . \tag{2.43}$$

$\Omega_{r0} = \rho_{r0}/\rho_{\mathrm{crit}}$, where ρ_{r0} is the present energy density in relativistic particles, and Ω_{m0} stands for the matter that can clump at small scales. For SCDM (where $\Omega_{r0} = 4.18 \cdot 10^{-5}$, $\Omega_{m0} \equiv \Omega_0$) $\Gamma = 0.5$ as introduced above. An increase in the density of relativistic particles – as in the case of the decaying neutrinos introduced above – lowers Γ. So, in order to obtain the desired

spectrum, the necessary density in relativistic particles has to be achieved.

It can be shown that Γ is a function of the mass and the lifetime of the massive neutrinos as follows

$$\Gamma = \Omega_0 h / [0.861 + 3.8 \, (m_{10}^2 \, \tau)^{2/3}]^{1/2} \tag{2.44}$$

This fitting formula is given by White et al. (1995). m_{10} is the mass of the neutrino in units of $10\,\mathrm{keV}$ and τ is its lifetime in years. Obviously, the τCDM model requires additional physics beyond the Standard Model of High Energy Physics. For more details about scenarios with decaying neutrinos and their cosmological implications c.f. Bharadwaj & Sethi (1998).

The parameters of the Virgo τCDM model are $\Omega_0 = 1$, $h = 0.5$, $\Gamma = 0.21$.

ΛCDM

Evidence is mounting that Ω_0 is actually smaller than unity and that the Hubble constant is larger than $h = 0.5$. The latter is still rather controversial. For the former, the situation is somewhat clearer. See below for a discussion of the value of Ω_0. Introducing a comological constant is the only solution which allows a low density in matter *and* a flat Universe (e.g. Efstathiou 1990b).

The introduction of a cosmological constant has immediate consequences which are often taken as a motivation itself. The age of globular clusters is often taken as evidence for a Universe which is significantly older than a universe described by a model with $\Omega_0 = 1$ – despite the large systematic errors in these measurements. If one assumes a flat universe (or if one believes in a Universe which has an age of around 15 Gyrs and $\Omega_{tot} = 1$) then a cosmological constant would have dominated the expansion of the Universe from $z \leq 0.6$. As already indicated above, the age of the universe is greater than the age of a matter dominated universe with $\Omega_{tot} = 1$, $t_0 = 2/(3H_0)$. Objects today have had more time to evolve in a Universe with a cosmological constant. Structure starts to grow earlier in the past, and later the growth of structure stops.

Estimates of the matter density on cluster scales usually yield $\Omega_0 \approx 0.3$. If one assumes that the universe is flat, that there is no additional matter in the Universe, and that the ages of globular clusters are correct, this leads to the following set of parameters for the ΛCDM model: $\Omega_0 = 0.3$, $\Lambda_0 = \Omega_{tot} - \Omega_0 = 0.7$, and $h = 0.7$. Obviously, this gives $\Gamma = 0.21$, close to what is desired.

However, the model has some limitations which will be mentioned briefly. Several measurements give rather strict limits on Λ_0. First of all, including a cosmological constant enhances the volume of the Universe itself. Hence, one gets an estimate of the number of lensed objects. Comparing this with observations one is able to deduce a limit of $\Lambda_0 < 0.6$ at 95 % c.l. (for a detailed paper see Kochanek 1996 and references therein). Also, there is no explanation for Λ_0 on the basis of particle physics. The model requires an extreme fine tuning to achieve the desired energy density of the vaccuum.

A second way of determining Λ_0 comes from measurements of space time itself. One takes so–called standard candles, whose behaviour is (assumed to be) well understood, and compares local measurements of these objects with ones at high redshift. Supernovae of type Ia are a promising candidate for this. This needs the observation of the lightcurves of a sufficient

number of distant supernovae, that is the brightness of the supernova as a function of time, beginning before they reach their maximum and extending well beyond this maximum. One then computes the effects of space time and fits the parameters Ω_0 and Λ_0 to a model for the apparant bightness–distance relation. Riess et al. (1998) reported on data for about 34 nearby and 16 high–redshift supernovae. They find that the data favours eternally expanding models with $\Lambda_0 > 0$ and a current acceleration, that is $q_0 \equiv \frac{\Omega_0}{2} - \Lambda_0 < 0$. A Universe closed by ordinary matter ($\Omega_0 = 1$) is ruled out at the 7σ level. It may still be flat, though, with a contribution of Λ_0.

OCDM

In terms of simple models, an open Universe model (OCDM, c.f. e.g. Ratra & Peebles 1994) is probably as simple as the original SCDM. Using the parameters $\Omega_0 = 0.3$, $\Lambda = 0$, and $h = 0.7$ is consistent with most observational constraints (see below). Also, the shape of the power spectrum is in the desired range, and there are no additional parameters which require extra physics. As already mentioned, variants of inflationary scenaria can produce open Universes (e.g. Turok & Hawking 1998). The open model has quite a similar behaviour to the model with the cosmological constant. As in the ΛCDM model, structure starts to grow earlier in the past, and later the growth of structure stops.

The Value of Ω_0

Determining the value of the density parameter has been one of the main goals of cosmology for decades. Despite enormous effort, so far no decisive point can be made[10]. In the following, some of the arguments are presented. Obviously, either some of the measurements or the models themselves must be wrong – simply because Ω_0 cannot be unity and smaller than unity at the same time. Only the results themselves and an outline of the arguments will be given. A thorough discussion of all the uncertainties involved is far outside the scope of this work (for more details on this topic c.f. Coles & Ellis 1997).

Dynamical mass of clusters: Assuming that the galaxies in a cluster may be regarded as test particles, the cluster mass can be measured (assuming virial equilibrium). Alternatively, cluster masses can be determined by gravitational lensing effects. Then, the mass–to–light ratio can be determined. Clusters are systems which formed from a large region in the initial density field. Therefore, it is *assumed* that their properties are the same as that of the Universe as a whole. Hence, converting the mass–to–light ratio into a value of Ω_0 should give the global value of Ω_0. For instance, Carlberg et al. (1996) get a value of $\Omega_0 = 0.24 \pm 0.05$ which is typical for studies like this.

Baryon Fraction in clusters: This study also assumes that because of the way clusters form measuring a property of the cluster gives the global value. White et al. (1993a) compared the mass in baryons (in galaxies and in the hot intracluster gas) with the total

---

[10]This statement is phrased as conservatively as possible. In the field, strong opinions exist about the value of Ω_0. However, in most cases these opinions are based on *one* indication. There still is enough room for the value of Ω_0 to lie between about 0.1 and 1, though recent evidence seems to favour smaller values.

dynamical mass in the Coma cluster. Following the argument that a cluster is a typical system, the baryon fraction must not be larger than its global value – given by the nucleosynthesis constraint. Using this logic, White et al. get the constraint

$$\Omega_0 \leq \frac{0.15\,h^{-1/2}}{1 + 0.55\,h^{3/2}}\,, \tag{2.45}$$

which is much less than unity for any likely value of h. This is generally referred to as the "baryon catastrophe" although it is only a catastrophe if one believes that $\Omega_0 = 1$.

Strong arcs in clusters: Using galaxy clusters from the GIF simulations introduced in Chapter 3, Bartelmann et al. (1998) investigated the number of strong arcs produced by the four cosmological models. Crudely speaking, to produce strong arcs a cluster needs a high concentration of mass in its center and it has to have formed by the redshift which is most efficient for the production of strong arcs ($z \approx 0.3$). Bartelmann et al. find that only the open model can account for the total number of arcs produced on the whole sky. In particular, the two high density models are two orders of magnitude less efficient producers of strong arcs. The ΛCDM model is intermediate.

High redshift supernovae: As already mentioned in the section on the ΛCDM model, the constraints from this technique favour eternally expanding models with $\Lambda_0 > 0$ and a current acceleration, that is $q_0 \equiv \frac{\Omega_0}{2} - \Lambda_0 < 0$. A Universe closed by ordinary matter ($\Omega_0 = 1$) is ruled out at the 7σ level (Riess et al. 1998).

Evolution of the cluster abundance: Due to the dependence on Ω_0 in the dynamical equations, low density Universes form massive galaxy clusters at earlier redshifts than high density Universes. This point will be examined in detail in section 6.3.

Peculiar Velocities of Galaxy Clusters: This will be investigated in detail for the different models in Chapter 5. Observationally, the *rms* peculiar velocities of samples of galaxy clusters are relatively low. This is (incorrectly) claimed to favour a low value of Ω_0 (e.g. Borgani at el. 1997).

Velocity–density reconstructions: In the linear theory, the velocity field is curl–free and can therefore be expressed as the gradient of a potential. One can thus map the potential from the observable radial peculiar field and so solve for the density field. This technique called POTENT (c.f. Dekel 1994 for a detailed discussion) suggests that the Universe has a high density.

From this short and incomplete list it is clear that to measure Ω_0, predictions have to be made which should be as precise as possible. Simulations can be used to do this – and in Chapters 5 and 6 the simulations presented in this work will be used to shed light on some of the points mentioned above. However, the use of simulations of structure formation in a gravitational instability scenario is not just restricted to measuring Ω_0. They can be used to achieve a better understanding of whether and how linear theory works (c.f. Chapter 5), and they can be used to investigate the distribution of mass as a whole. Before turning to this point in Chapter 4, in the following Chapter, the simulation sets will be introduced. The technical background will be given in Chapter 8.

Bibliography

[1] Bahcall N.A., Cen R., ApJ Lett. **398**, L81 (1992)

[2] Bardeen J.M., Bond J.R., Kaiser N., Szalay A.S., ApJ **304**, 15 (1986A)

[3] Bartelmann M., Huss A., Colberg J.M., Jenkins A., Pearce F.R., A&A **330**, 1 (1998)

[4] Bartlett J.G., Blanchard A., Silk J., Turner M.S., Science **267**, 980 (1995)

[5] Bharadwaj S., Sethi S.K., ApJS **114**, 37B (1998)

[6] Bond J.R., Efstathiou G., Silk J., Phys. Rev. Lett. **45** (1980)

[7] Bond J.R., Efstathiou G., ApJ **285**, L45 (1984)

[8] Borgani S., Da Costa L.N., Freduling W., Giovanelli R., Haynes M.P., Salzer J., Wegner G., ApJ **482**, 121L (1997)

[9] Branch D., ARAA **36** (1998)

[10] Bunn E.F., Scott D., White M., ApJ **441**, 9B (1995)

[11] Carlberg R.G., Yee H.K.C., Ellingson E., Abraham R., Gravel P., Morris S., Pritchet C.J., ApJ **462**, 32 (1996)

[12] Coles P., Ellis G.F.R., Is the Universe Open or Closed?, Cambridge Lecture Notes in Physics, Cambridge University Press, Cambridge (1997)

[13] Copi C.J., Schramm D.N., Turner M.S., Phys. Rev. Lett. **75**, 3981 (1995)

[14] Davis M., Efstathiou G., Frenk C.S., White S.D.M., ApJ **292**, 371 (1985) (DEFW)

[15] Dekel A., ARAA **32**, 371 (1994)

[16] Efstathiou G., Cosmological Perturbations, in Physics Of The Early Universe, ed.s Peacock J.A., Heavens A.F., Davies A.T., Proceedings of the Thirty–Sixth Scottish Universities Summer School in Physics 1989, SUSSP Publications, University of Edinburgh (1990a)

[17] Efstathiou G., Sutherland W.J., Maddox S.J., Nature **348**, 705 (1990b)

[18] Efstathiou G., Bond J.R., White S.D.M., MNRAS **258**, 1 (1992)

[19] Efstathiou G., MNRAS **274**, 73 (1995)

[20] Eke V.R., Cole S., Frenk C.S., MNRAS **282**, 263 (1996)

[21] Guth A.H., Phys. Rev. D **23**, 347 (1981)

[22] Jenkins A., Frenk C.S., Pearce F.R., Thomas P.A., Colberg J.M., White S.D.M., Couch-man H.M.P., Peacock J.A., Efstathiou G., Nelson A.N. (The Virgo Consortium), ApJ **499**, in press (1998)

[23] Kochanek C., ApJ **466**, 638 (1996)

[24] Ostriker J.P., ARAA **31**, 689 (1993)

[25] Ostriker J.P., Steinhardt P.J., Nature **377**, 600 (1995)

[26] Peacock J.A., Dodds S.J., MNRAS **267**, 1020 (1994)

[27] Primack J.R., Dark Matter and Structure Formation, in Formation of Structure in the Universe, Proceedings of the Jerusalem Winter School 1995, ed.s Dekel A. and Ostriker J.P., Cambridge University Press (in press)

[28] Ratra B., Peebles P.J.E., ApJ **432**, L5 (1994)

[29] Riess A.G., Filippenko A.V., Challis P., Clocchiattia A., Diercks A., Garnavich P.M., Gilliland R.L., Hogan C.J., Jha S., Kirshner R.P., Leibundgut B., Phillips M.M., Reiss D., Schmidt B.P., Schommer R.A., Smith R.C., Spyromilio J., Stubbs C., Suntzeff N.B., Tonry J., to appear in ApJ, also astro-ph/9805201

[30] Springel V., White S.D.M., Colberg J.M., Couchman H.M.P., Efstathiou G., Frenk C.S., Jenkins A., Pearce F.R., Nelson A.N., Peacock J.A., Thomas P.A., submitted to MNRAS (astro-ph/9710368)

[31] Turok N.G., Hawking S.W., hep-th/9803156

[32] Viana P.T.P., Liddle A.R., MNRAS **281**, 323 (1996)

[33] White S.D.M., Frenk C.S., Davis M., ApJ **274**, L1 (1983)

[34] White S.D.M., Frenk C.S., ApJ **379**, 52 (1991)

[35] White S.D.M., Navarro J.F., Evrard A.E., Frenk C.S., Nature **366**, 429 (1993a)

[36] White S.D.M., Efstathiou G., Frenk C.S., MNRAS **262**, 1023 (1993b)

[37] White D.A., Fabian A., MNRAS **273**, 72 (1995)
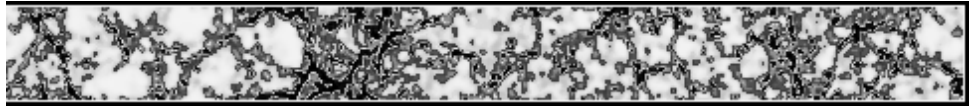
The Simulation Sets

In this Chapter, the simulation sets will be introduced. In addition, image processing techniques will be discussed. These techniques will then be combined to give pictorial impressions of the different cosmologies.

Apart from the Hubble Volume Simulations, which will be introduced separately in Chapter 6, two sets of simulations were run. They feature the models introduced in section 2.3.5. All the simulations were run as part of the Virgo Supercomputing Consortium which is based in Britain, Germany, and Canada and which consists of scientists from these countries. Its (core) members are Frenk, Jenkins, and Pearce (Durham, UK), White, Colberg (Garching, D), Thomas (Sussex, UK), Couchman (London, CAN), Efstathiou (Cambridge, UK), and Peacock (Edinburgh, UK).

The two simulation sets were primarily done for different purposes although they have been used for a plethora of applications since they were finished. They will be referred to as the Virgo and the GIF simulations for reasons which will be clear in the following.

The code used to run these simulations will be discussed in Chapter 8, where a summary of code development done during the course of this work will also be given.

3.1. The Virgo Simulations

The first set of simulations was run in late 1995 and early 1996. It made use of the 128 (256) processor CRAY T3D at the computer center of the Max–Planck–Gesellschaft, the Rechenzentrum Garching, RZG (at the Edinburgh Parallel Computer Center, EPCC). It consists of the four models introduced in section 1.3.5 following the evolution of 256^3 particles in cubic boxes of size $240\,\mathrm{Mpc}/h$ each. All four models were run with the same phases for the initial density field. The gravitational softening is $30\,\mathrm{kpc}/h$. The parameters of the Virgo simulations are summarized in Table 1.1. As can be seen, the high and low density models have different mass resolutions. The simulations are all cluster normalized (c.f. section 1.3.4). The *rms*

Model	Ω	Λ	h	Γ	σ_8	l	m_{p}
SCDM	1.0	0.0	0.5	0.50	0.51	240	22.1
τCDM	1.0	0.0	0.5	0.21	0.51	240	22.1
ΛCDM	0.3	0.7	0.7	0.21	0.90	240	6.8
OCDM	0.3	0.0	0.7	0.21	0.85	240	6.8

Table 3.1.: The parameters of the Virgo simulations. The cosmological parameters are noted as introduced in Chapter 2. l denotes the size of the box in one dimension and is given in Mpc/h. m_{p} is the mass of a single particle in units of $10^{10} \, h^{-1} \, \mathrm{M}_\odot$.

Model	Ω	Λ	h	Γ	σ_8	l	m_{p}
SCDM	1.0	0.0	0.5	0.50	0.60	85	1.0
τCDM	1.0	0.0	0.5	0.21	0.60	85	1.0
ΛCDM	0.3	0.7	0.7	0.21	0.90	141	1.4
OCDM	0.3	0.0	0.7	0.21	0.85	141	1.4

Table 3.2.: The parameters of the GIF simulations. The cosmological parameters are noted as introduced in Chapter 2. l denotes the size of the box in one dimension and is given in Mpc/h. m_{p} is the mass of a single particle in units of $10^{10} \, h^{-1} \, \mathrm{M}_\odot$.

mass fluctuations in spheres of size $8\,\mathrm{Mpc}/h$ originally were $\sigma_8 = 0.6$, 0.6, 0.9, and 0.85 for SCDM, τCDM, ΛCDM, and OCDM, respectively. However, with this normalization – which adopts the Eke et al. (1996) and the White et al. (1993) normalizations for the low and high density models, respectively – the abundances of massive clusters in the models do not agree. The high Ω_0 models produce three times more massive clusters than their low density counterparts. This was found during the course of this work and by Thomas (private communication). It is (partly) reflected in the numbers given in Thomas et al. (1997). Because of this the SCDM and τCDM models were rescaled such that the earlier outputs at $z = 0.2$ were taken to be $z = 0$. This yields $\sigma_8 = 0.51$ and makes the abundances agree. When the code for the T3E became available in 1997, the high density models were re–run in order to get the desired *rms* mass fluctuations at $z = 0$. This was also a good test of the new code. The new code exactly reproduced the results of the old one.

Jenkins et al. (1998) contains an introduction to further technical details of these simulations, pictures (see below), and a discussion of the power spectra, correlation functions, bulk flows, and pairwise velocity statistics. The simulations were also used to study the internal properties of galaxy clusters (Thomas et al. 1997) and to compute genus statistics (Springel et al. 1998).

3.2. The GIF simulations

The second set of simulations was run with the same mass resolution for each model. In each of the simulations, a single particle has a mass of $2.0 \cdot 10^{10}\,M_\odot$. Again, each simulation follows the evolution of 256^3 particles. Hence, the sizes of the simulated volumes are different for the low and high density models. Table 1.2 summarizes the parameters of the GIF models. Note, that for the GIF models the original cluster normalization is used. The simulation set was run with the same phases for the initial density field, too. The gravitational softening is again $30\,\mathrm{kpc}/h$. The simulations were all started on the CRAY T3D at the RZG and, once the clustering required more memory, transferred to the bigger T3D at the EPCC.

These GIF simulations were originally run to be used as part of the GIF collaboration[1] which consists of scientists from Germany and Israel. In order to be able to extract accurate merger histories of objects which are used for so–called semi–analytical models, 50 output dumps between $z = 20$ and $z = 0$ were produced and stored. This amounts to around $50\,\mathrm{GByte}$ if only the compressed data, which is used for the analysis, is summed up. Kauffmann et al. (1998) contains the first implementation of the semi–analytics into the ΛCDM and τCDM models. The simulations were also used to compute arc statistics (Bartelmann et al. 1998), and they also appear in Jenkins et al. (1998).

3.3. Visualization Techniques

The usual visual representation of N–body simulations in the pre–Virgo days had been the use of simple particle (dot) plots. For low resolution simulations where only massive objects are well resolved this is probably the best way to show the structure. However, for high resolution simulations like the Virgo and especially the GIF simulations, better representations had to be found[2]. The adopted solution for this problem was the adaptive smoothing algorithm which will be motivated and discussed in more detail in the following.

Note that all high resolution colour pictures can be found in the Appendix!

3.3.1. Adaptive Smoothing

The first improvement to black and white dot plots is to compute densities on a grid and to code the result with colours. A typical slice through one of the Virgo simulations could then look like figure A.1. This shows the particles in a slice of thickness $22.5\,\mathrm{Mpc}/h$ through the whole Virgo SCDM box. It contains about 1.5 million particles which were assigned to a grid using a nearest grid point assignment (NGP, see e.g. Hockney & Eastwood 1981). For this picture, already, a further improvement was implemented. The density contrast between the dark low density

---

[1] GIF stands for German Israeli Foundation which was the supposed funding organization. Ironically, the proposal was turned down.

[2] This is interesting for works which appear on astro-ph, too. Dot plots with millions of particles lead to huge postscript files. Few people seem to notice that the size of a dot plot can usually be decreased quite massively by simply converting the postscript plot into a high resolution GIF or JPEG picture. A postscript plot can have several dots at the same position (postscript has one command for each dot), a GIF can't. Converting it back then leads to a postscript plot with at most one dot at any position.

regions and the bright particle knots is so large that the logarithm of the particle densities on the mesh was used to set up the colour table.

Despite the low resolution of this test case, the result of the efforts so far still leaves a lot to be desired. The particle knots all look quite nice, but the low density regions are dominated by noise. This leads naturally to the idea of smoothing. Figure A.2 shows the same slice smoothed with a Gaussian filter with a kernel size of $2.5\,\mathrm{Mpc}/h$. This has removed the noise from the voids, but on the other hand it has smeared out the knots completely. Obviously, a uniform change in the kernel size would not solve the problem – in order to resolve the knots the size of the kernel should be very small which again leads to particle noise in the low density regions.

The ideal way to deal with a picture like the one in Fig. A.1 would be to leave the knots as they are and smooth the regions of low density. Such a procedure, in a slightly different context, is well known in Smoothed Particle Hydrodynamics (SPH). There, the continous fluid is modelled by particles. Each particle represents some region in space. Very crudely speaking, the size of this region is determined by the local density at the particle position. This is exactly what is needed for the smoothing. Particles in high density regions do not need to be smoothed, whereas for particles in low density regions a smoothing has to be found which depends on the local density itself. That way, a non–global smoothing is achieved.

Technically, the problem is solved on the grid. A different approach would be to find the local densities for the particles themselves (as in SPH) and then assign them to a grid using these densities to define a filter radius. However, this procedure does not lead to pictures which are different from the ones obtained with the method used here (Jenkins, private communication). Starting from a configuration like the one shown in figure A.1, for each grid point a smoothing length is found as follows. If the contents of the grid point exceeds N particles, no smoothing is applied. If it is lower than N particles, the contents of the neighbouring eight mesh cells are added using a weighting which takes into account that the ideal neighbouring region of the mesh cell should be a sphere rather than a square. The procedure is stopped if N particles are now reached, and it is continued going further out otherwise. The number of particles required, N, is a free parameter. Numbers between $N = 20$ and $N = 30$ turn out to give very similar and satisfactory results. Thus, a smoothing radius is computed for each mesh cell. In the second stage of the algorithm, this radius is used as the size of a Gaussian filter to redistribute the mass in the cell onto the mesh. Mass conservation is ensured which will be important for the discussion of the three–dimensional distribution of matter in the following Chapter.

Figure A.3 shows the result for the test case. As can be seen, the low density regions no longer contain significant particle noise, the particle knots are clearly resolved, and a plethora of filaments connecting the high density regions shows up.

This adaptive smoothing algorithm was coded on a three–dimensional mesh, too. It will be used in the following Chapter for the investigation of the mass distribution. However, finding a good three–dimensional representation of the mass distribution is very difficult for reasons which will be become evident in Chapter 7. Two–dimensional representations of the mass distribution in slices yield probably the maximum amount of information *at the same time* – which is why the attention is focused on such two–dimensional visual representations in the following section, which concludes this Chapter.

3.3.2. Cosmology with Pictures

In Chapter 2, the basic cosmological equations and notions, and our four cosmological models were introduced. From the equations themselves, a couple of points became clear. Pictures obtained with the adaptive smoothing can shed further light onto this.

Figure A.4 shows a slice of thickness 8.5 Mpc/h through the τCDM GIF simulation. A variety of structure elements can be seen. Right in the middle of the picture a very large underdense region, a void, can be seen. The void is surrounded by a complicated network of mass conglomerates. To the South there is a huge galaxy cluster, accompanied by many smaller objects. The South–Western boundary of the void is formed by a sheet – as will be shown in Chapter 7. Clearly, regardless of their size the majority of objects are part of the network. Big objects appear to be clustered, and they are surrounded by smaller ones. The bridges between them, filaments and sheets, are mainly populated by small objects and a smooth component. This network will be investigated in considerably more detail in the following Chapter. Such structures can be seen in galaxy surveys, too (see e.g. the Las Campanas Redshift Survey, Shectman et al. 1996). There too, galaxies line up in filaments and sheets which surround voids.

Figure A.5 shows slices of thickness 22.5 Mpc/h through the four Virgo models at $z = 0$. For each picture, after the smoothing the *mass* density was divided by the mean, and then the logarithm was taken. The same colour tables were used. The pictures look quite similar but there is a big difference between the low and high density models. In general, the voids in the low density models are emptier than in their high density counterparts. This lets the low density models appear darker. Note that, in a region of fixed size, high and low density models contain different amounts of total mass. From the pictures, it can be seen that most of the additional mass of the $\Omega = 1$ models is in the voids. The two low density models, OCDM and ΛCDM, are hardly distinguishable. The same is true for the two $\Omega = 1$ models. τCDM appears to be slightly smoother than SCDM. Recall that these two models differ by the relative amounts of large and small–scale power. SCDM has more small scale power which leads to the appearance of more small objects than in τCDM.

Apart from SCDM, which is known to be a poor fit to several observations (compare Chapter 2, section 2.3.5), the models all have parameters which lie within the observational bounds. Clearly, there are differences between the τCDM and the two low density models which have to be explained. If it were possible to identify locations of galaxies in the Dark Matter distributions, pictures of the galaxy distributions would have to look identical. This leads to the notion of *bias*. It is beyond the scope of this work to go into the details of biased galaxy formation. In the following, only a very general and brief introduction is given which explains the problem with the difference in appearance of the models.

The simplest *Ansatz* for the relationship between the distribution of the density field of the Dark Matter, δ_{DM}, and that of the galaxies, δ_{g}, would be to assume that "light traces mass", that is, galaxies are found in the bright spots[3]. Thus, galaxies and Dark Matter have the same clustering properties. However, under this hypothesis the differences between the τCDM and

---

[3] Occam's Razor which is often used as an argument for $\Omega = 1$ (because the equations of such a cosmology can be solved so easily; see e.g. Dekel et al. 1997) here would actually say that $\Omega < 1$. In most low density models currently under consideration, no bias or only a very small bias is needed. The assumption that light traces mass is clearly much simpler than a complicated relationship between them.

the OCDM and ΛCDM models do not appear. Clearly, in order to get the same galaxy distribution for the high and low density models, the clustering properties of the Dark Matter and the galaxies must be different in τCDM. The simplest *Ansatz* is to assume a linear relationship independent of scale

$$\delta_{\mathrm{DM}} = b\, \delta_{\mathrm{g}}, \tag{3.1}$$

where b is the so–called bias parameter. The *rms* fluctuation in the number counts of galaxies on a scale of $8\,\mathrm{Mpc}/h$ is $\sigma_{8,\mathrm{g}} \approx 1$ (Davis & Peebles 1983). Hence, in order to reproduce the observed clustering of the galaxies, a high density model has to have a positive bias whereas a low density model is not at all or only mildly biased.

As discussed in sections 2.3.3 and 2.3.5, the simulations are set up using Gaussian initial conditions with the amplitudes required to yield the observed abundance of rich clusters. Figure A.6 shows slices of thickness 1/10th of the box size through the four GIF models at $z = 0$ obtained in the same fashion as the slices for the Virgo models. The GIF models look identical! Of course, they are not completely identical. Very small differences in the concentrations of the massive objects can be seen, and subtracting the pictures of, say, the SCDM and τCDM model from each other displays offsets in the positions of the overall structure.

On the other side, the pictures *must* look identical by construction of the models. Because the models were cluster normalized and run with with the same phases, the same objects form at about the same position in each of the models – which is why they look nearly identical at $z = 0$. The sizes of the void regions are different for the low and high density models, but because the mass evacuated into the clusters and walls, they look the same with the scaling adopted in these pictures.

Clear differences between the models appear if slices at earlier redshifts are taken. Figure A.7 shows the same slice through the four models at $z = 1$. Here, the difference in the evolution between high and low density universes shows up. OCDM and ΛCDM still look quite similar. However, a difference between the two high Ω_0 models becomes visible. In the τCDM model, matter is distributed over wider regions in space than in the SCDM model. In addition, objects appear to be brighter and more massive in the low Ω_0 models than in their high density counterparts. Apparently, this is due to the formation time of these objects which is at higher redshifts. Chapter 6 will come back to this point when the appearance of massive galaxy clusters at a redshift of $z = 0.8$ is investigated for the Hubble Volume Simulations.

Figure A.7 shows slices through the four models at $z = 3$. The differences between the models are now even stronger. From these pictures it can seen that

1. low density models start to form structure earlier than models with $\Omega_0 = 1$. In particular, the open model starts first, followed by ΛCDM. As a consequence, there should be relatively few massive objects at high redshifts in a high density Universe (see section 6.3).

2. the growth of structure saturates for low density models near $z = 1$. That is, it is hard to distinguish between OCDM and ΛCDM in the late stages of their evolution, and there is very little difference between these models after about $z = 1$.

3. the difference in the power spectra of the two high density models shows up as a difference in the clustering strength. SCDM has more power on small scales which makes it

form more objects (due to the way the simulations are normalized, they all form the same number of objects corresponding to rich clusters. Below that mass limit, SCDM forms more objects). The τCDM model forms structure latest among these four models.

In the next Chapter, the three–dimensional mass distribution in the GIF models at $z = 0$ is investigated. This addresses questions related to the ones discussed above, albeit from a different angle. Is the mass distribution really as similar in the models as the pictures (Fig. A.6) suggest?

Bibliography

[1] Bartelmann M., Huss A., Colberg J.M., Jenkins A., Pearce F.R., A&A, **330**, 1 (1998)

[2] Couchman H.M.P., ApJ **368**, L23 (1991)

[3] Davis M., Peebles P.J.E., ApJ, **267**, 465 (1983)

[4] Dekel A., Burstein D., White S.D.M., in "Critical Dialogues in Cosmology" (Princeton 250th Anniversary), ed. Turok N., World Scientific

[5] Eke V.R., Cole S., Frenk C.S., MNRAS **282**, 263 (1996)

[6] Hockney R.W., Eastwood J.W., "Computer simulation using particles", McGraw–Hill 1981

[7] Jenkins A., Frenk C.S., Pearce F.R., Thomas P.A., Colberg J.M., White S.D.M., Couchman H.M.P., Peacock J.A., Efstathiou G., Nelson A.N. (The Virgo Consortium), ApJ **499**, in press (1998)

[8] Kauffmann G.A.M., Colberg J.M., Diaferio A., White S.D.M., astro-ph/9805283

[9] MacFarland T.J., Couchman H.M.P., Pearce F.R., Pichlmaier J., submitted to New Astronomy, astro-ph/9805096

[10] Pearce F.R., Couchman H.M.P., New Ast **2**, 411 (1997)

[11] Peebles P.J.E., The Large–Scale Structure of the Universe, Princeton University Press (1980)

[12] Shectman S.A., Landy S.D., Oemler A., Tucker D.L., Lin H., Kirshner R.P., Schechter P.L., ApJ, **470**, 172 (1996)

[13] Springel V., White S.D.M., Colberg J.M., Couchman H.M.P., Efstathiou G., Frenk C.S., Jenkins A., Pearce F.R., Nelson A.H., Peacock J.A., Thomas P.A., accepted by MNRAS, astro-ph/9710368

[14] Thomas P.A., Colberg J.M., Couchman H.M.P., Efstathiou G., Frenk C.S., Jenkins A.R., Nelson A.H., Hutchings R.M., Peacock J.A., Pearce F.R., White S.D.M. (The Virgo Consortium) accepted by MNRAS, astro-ph/9707018

[15] White S.D.M., Efstathiou G., Frenk C.S., MNRAS **262**, 1023 (1993)
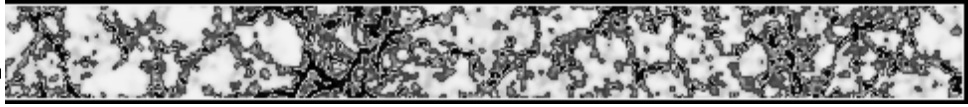
The Distribution of Mass

4.1. Introduction

As soon as the first large catalogs of galaxies were assembled it was realized that on scales of a few megaparsecs and larger the distribution of galaxies is not homogeneous. Maps of the distribution show a complicated network, and there have been nearly as many suggestions of what can be seen as there are galaxy catalogs. One of the most famous features, the so–called "Great Wall", dates back to the second CfA redshift survey: De Lapparent et al. (1986) argued that the structures that can be seen are cuts through large sheets of galaxies, rather than filaments, because one would not expect to find many long parts of filaments in the slices which represent the catalog. Other authors, however, have argued that galaxies preferentially lie in filaments (c.f. e.g. Haynes 1986). The situation may be clearer for those regions where no or few galaxies can be found, the so–called voids (Kirshner et al. 1981). These voids are not completely empty (Lindner et al. 1996).

One of the main assumptions in Cosmology is that the Universe is homogeneous on large scales (see Chapter 2). With current galaxy surveys, this scale of homogeneity has not been reached, yet. It will require the forthcoming very large galaxy surveys like the *Sloan Digital Sky Survey* to get there.

The first large N–body simulation of the Cold Dark Matter (CDM) model led to a qualitative appearance of the distribution of matter which was similar to the one in galaxy catalogs. For instance, Davis et al. (1985) noted that "structure appears very rapidly, and filaments, superclusters of clumps, and large low–density regions" developed in their simulations, which had 32^3 particles. Since then, it has been possible to run larger and larger simulations, making use of the latest generations of computers. During the last couple of years it finally became possible to run simulations with a very large number of particles in large computational volumes. The GIF simulations introduced in the preceding Chapter are ideal for detailed studies of Large–Scale Structure (LSS) because of their very high mass resolution in a sufficiently large volume. Thus, it will be possible to discuss the spatial distribution of matter in the computa-

tional volume in detail. As a starting point, the connectedness of the matter will be investigated. This is done on an adaptively smoothed density grid rather than on the point distribution of the particles. Overdensity is used in order to discriminate between over–dense and under–dense regions: For each value of the overdensity used as threshold a set of volume cells filled with matter is obtained. Each pair of cells which shares an adjacent face is treated as being part of a bigger object. Thus, a set of objects is obtained for each overdensity threshold. What are the properties of this set? Imagine a reef. At low tide, the whole structure of the reef can be seen. As the tide rises, more and more of the reef will be covered and eventually, at high tide, only a few islands are still visible. How does the distribution of matter look like if it is treated in a similar fashion? How much mass is above the threshold? And how much volume is occupied by this mass? And what can be said about what LSS consists of? These questions will be addressed in the following.

4.2. The Distribution of Mass

4.2.1. Introduction

In order to investigate the distribution of mass the density field is obtained by binning the distribution of particles on a three dimensional mesh of size 256^3 using a nearest gridpoint scheme. The mesh cells themselves are smoothed adaptively as described in the preceding Chapter requiring 30 neighbours. It will be checked later that the number of particles used does not affect the results.

The smoothed density field is then transformed into a field which contains overdensities by dividing by the mean density and subtracting 1. Different threshold values of the overdensity are used to define overdense and underdense regions. They are marked by replacing the overdensities with 1 and 0, respectively.

Unless a very large value for the threshold is taken some of the mesh cells will be part of a bigger object. For instance, as the length of a mesh cell is smaller than the typical size of a galaxy cluster, the cluster will consist of a set of cells. In order to find connected mesh cells pairs have to be found which have an adjacent face. This can be achieved quite nicely. Treating the centers of overdense mesh cells as particles, there is a set of particles where all pairs of particles with a distance of 1 (in units of the mesh) are members of the same group. A friends–of–friends (FOF) group finder is run to get all connected mesh cells. Such a group finder will be used in various parts of this work. It works as follows. Imagine a set of particles. The aim is to find all particles which are part of a group. This is only a well–defined object if a criterion is given what a group actually is. A FOF group finder treats two particles as friends (and thus part of a group) if their separation is smaller than some given value. A third particle which may be a friend of one of the two particles, then becomes a friend of the other one, too, etc. So the FOF group finder finds all particle pairs whose separation is smaller than some given number and then constructs the groups. The maximum separation required is an input parameter. Usually, a fraction of the mean inter–particle separation is taken. In Chapter 6, the "standard" value of 20% (which is usually noted as $b = 0.2$) is taken which more or less yields virialized objects[1].

---

[1]The fact that this yields virialized objects is, of course, empirical.

Lowering the maximum separation yields smaller groups. That way, in Chapters 5 and 6 only the densest knots of groups are found. For the mass distribution considered here, the maximum separation is well–defined. If the overdense mesh cells are considered to be small cubes, two cubes which have an adjacent face are part of a bigger object. That is, two cubes are part of an object if their centers have a separation of 1 in units of the mesh size. Using this, the group finder is run on the set of cube centers for each overdensity threshold.

Having stored the mass in each cell the masses of the objects can be computed. The volume is obtained by multiplying the number of cells per object with the volume of an individual mesh cell.

4.2.2. Visual Impression

As a starting point, a visual impression of what is obtained once this procedure is applied to the smoothed density field is given. Fig. A.9 shows all objects in the τCDM box at an overdensity of 2. It is hard to see much from the picture. It is clear that there is a huge number of very small objects. However, there appears to be one big object which extends all across the simulation box, too. All the other models look exactly the same if they are displayed in this fashion. It is impossible to tell the difference visually, which is the same situation already known from the smoothed two–dimensional pictures seen in the preceding Chapter.

In Fig. A.10 only the biggest object is shown. It consists of a very complicated network of filaments. The filaments themselves come in various sizes. Some of them appear to be thick, others are very thin. Note that the small lumps which appear isolated are in fact connected to the single large object because periodic boundary conditions are used. The biggest object extends all across the simulation volume, a phenomen known as *percolation* (which was introduced in the cosmological context by Zel'dovich 1982). Fig. A.11 shows the biggest object from different angles. A zoom of an eighth of the object in fig. A.10 is shown in Fig. A.12. Clearly, the structure is filament–like.

As will be seen later, the visual impression from Fig.s A.9 and A.10 is slightly misleading. The biggest object contains about 90% of the total overdense mass and occupies about 80% of the overdense volume. This amounts to about 50% of the total mass in the simulation box but only to 2.5% of the total volume.

What happens to this object if the overdensity threshold is increased? Fig. A.13 shows the biggest object in the τCDM box at an overdensity of 3. Percolation still occurs, but some of the thin bridges which can be seen in Fig. A.10 must have been broken so that the big object was disassembled into smaller pieces of which the biggest is displayed here. This resulted in the loss of quite a lot of the complicated network. In a sense, the biggest object at this threshold marks the backbone of the one seen before. In particular, the thick filaments which form a pentagon with two large extensions stand out. The object now contains about 30% of the total mass and about 1% of the total volume. Note that due to periodic boundaries the big chunk of the object at the rightmost edge of the picture is in fact connected to the rest. Now, it is easier to get an idea of what kind of structure is formed by the biggest object.

If the overdensity threshold is increased even further, the biggest object starts to break up into much smaller pieces. Fig. A.14 shows the biggest object at an overdensity of four, and it is not clear anymore whether it extends across the box or not. Eventually, when the threshold

is increased even further, this object crumbles into many smaller pieces. The biggest one is identical with the biggest cluster in the box. All big clusters are part of the network seen in Fig. A.10.

So there are no sheets in the simulations? At least there are no sheets which have an overdensity of two or more. They may have smaller overdensities but the structure of the biggest objects becomes so complicated at, say, an overdensity threshold of one that it is impossible to get a good visual impression of it. Thus, if sheets do exist in the simulations their mean density must be very small.

In a sense, the visual impression from the pictures shown above could be misleading because at the overdensities which can be displayed nicely only filaments appear and no sheets. In the preceding Chapter, the four GIF models looked completely identical on adaptively smoothed two–dimensional pictures. Could it be that this impression is misleading, too? In the following section, percolation, and mass and volume fractions will be investigated in more detail. If the mass distributions in the models really were identical, these quantities should show the same behaviour.

4.2.3. Total Mass and Volume Fractions

The total overdense mass and its occupied volume obviously depend on the overdensity threshold. Figure 4.1 shows the fraction of the overdense mass as a function of the overdensity threshold. An isooverdensity contour of 0, i.e. mean density, encloses around 80 to 85% of the mass for all the models. As the threshold is increased the mass fractions decrease. The models which all looked completely identical on the two dimensional pictures of the preceding Chapter, show some differences. The two low density models are nearly indistinguishable. However, the two high density models differ significantly. τCDM, which has the same shape parameter Γ, has less mass above the threshold. SCDM has more mass above it. The difference between the two high density models which differ in their shape parameter but not in the overall normalization of the power spectrum is pretty impressive. SCDM has more small scale power and, thus, more collapsed objects. This clearly shows up when compared with τCDM. The difference to the two low density models is smaller because these have a higher normalization than τCDM.

For large thresholds ($\delta \sim 180$), the order of the mass fractions is unchanged. However, the differences become very small in terms of the total overdense mass. SCDM has the highest mass fraction (about 0.3%), ΛCDM and OCDM have about the same one (about 0.28%), and τCDM has the smallest mass fraction (about 0.2%).

How does the overdense volume occupied by the mass behave in the four models? Fig. 4.2 shows the overdense volume as a function of the overdensity threshold for the four models. Here, the change with an increase of the threshold is much more dramatic. At mean density, the volume occupied by the overdense mass is only 12% to 14%. It then falls rapidly to below 1%. The τCDM models stands out for low overdensity thresholds. Its overdense volume is about 10% (relative to the overdense volume) larger than for the other three models (for $\delta < 4$).

Thus, these volume fractions reveal some of the differences between the four cosmological models which cannot be seen on the two dimensional representations of the preceding Chapter, and must be due to the differences in their power spectra. The two low density models are very nearly indistinguishable. τCDM has less overdense mass in a larger region than the
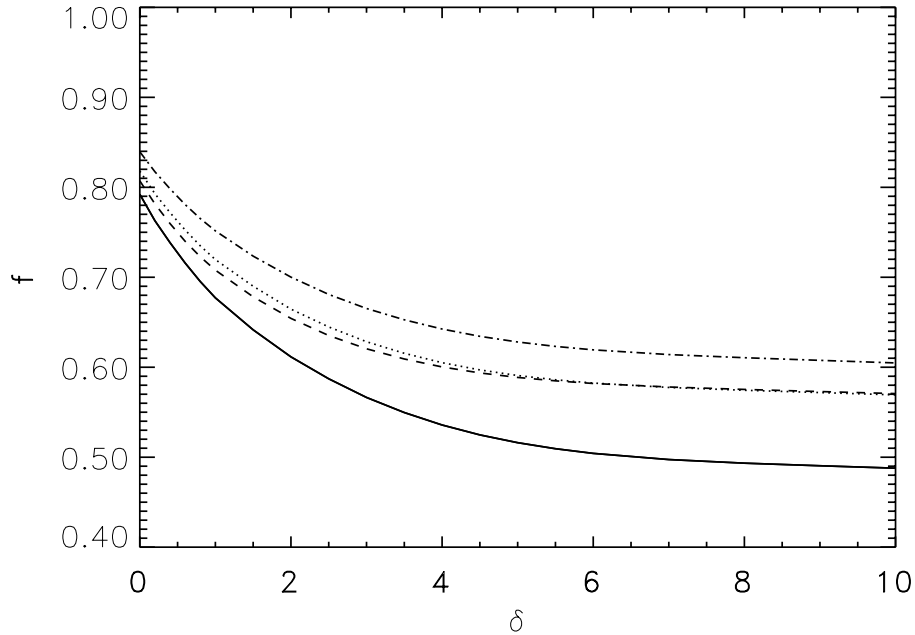
Figure 4.1.: Fraction of overdense mass as a function of the overdensity for the four models: τCDM (solid), ΛCDM (dotted), OCDM (dashed), and SCDM (dot dashed).

other three models. These occupy about the same volume. SCDM, which has more small–scale power, has more overdense mass than the two low density models – probably a reflection that it has formed more small haloes. Further insight can be gained if the properties of the largest overdense object are investigated. These should reflect the explanations given above. In the following section, the attention is thus focused on the largest overdense object.

4.2.4. Percolation

In this section, only the overdense mass is considered. As described above, the largest object is constructed by means of the friends–of–friends group finder. Fig. 4.3 shows the fraction of the overdense mass which is in the largest object as a function of the overdensity threshold. The general behaviour is the same in all models. For low values of the overdensity ($\delta < 1.5$), most of the overdense mass is part of one object. As the threshold is increased, the fraction of overdense mass in the largest object decreases rapidly to reach only a few percent for $\delta = 10$. The overdensity at which the largest object breaks down varies for the models. τCDM stands out. Here, the largest object dominates for relatively high overdensity thresholds. For instance, at $\delta \approx 3.2$ 50% of the overdense mass in the τCDM model is still in the largest objects whereas for the other models this number is down to 10% or even less. The three other models are very similar although small differences are visible between them. The largest object is the least pronounced in the SCDM model. This clearly reinforces the explanation of the model's behaviour in terms of the total overdense mass and volume discussed above. SCDM has more power on small scales, that is it forms more small haloes. The three models with the same shape parameter of the power spectrum should differ due to the different normalizations and
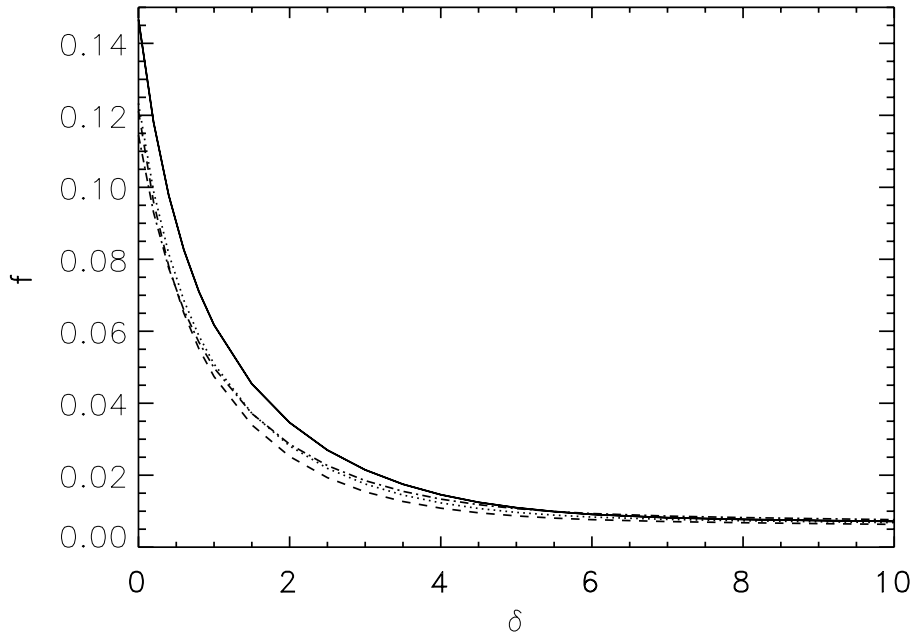
Figure 4.2.: Fraction of the volume occupied by all objects above overdensity threshold as a function of the overdensity for the four models: τCDM (solid), ΛCDM (dotted), OCDM (dashed), and SCDM (dot dashed).

their different formation histories. This point of view is supported by fig. 4.3 where the open model is the closest to the SCDM model.

Clearly, at low overdensities ($\delta < 1.5$) most of the overdense mass is in one single object which occupies most of the overdense volume. That is, the biggest object extends all across the simulation volume – it percolates (Zel'dovich 1982). This was already seen pictorially in the three dimensional representations shown in the pictures above. A slightly different way to show percolation and how it breaks down for different overdensities is by plotting the quantity $\Sigma m^2 / \Sigma m$, where the summation is over all objects above the overdensity threshold, see fig. 4.4. In this plot the abruptness of the percolation transition is very evident. For very low overdensities, $\Sigma m^2 / \Sigma m$ approaches the total mass in the volume.

Dividing the mass in the biggest object by the volume it occupies yields its density, which is displayed in fig. 4.5 in units of the particle masses. Here, a well known behaviour shows up. The objects in the OCDM model have the largest density, τCDM has the lowest one. The density of an object depends on its formation time. OCDM forms objects the earliest which is why its objects have the largest densities.

How much do these results depend on the particular circumstances of the chosen parameters? In particular, what happens if parameters like the number of neighbours required for the adaptive smoothing is changed? In order to investigate this, a couple of systematic checks were done.

The first set of checks investigates the influence of the mass resolution of the simulation itself. Taking the OCDM simulation as a test case, the above analysis is repeated with subsets which contain 50%, 30%, and 13% of the particles in the simulation. This appears to have

48
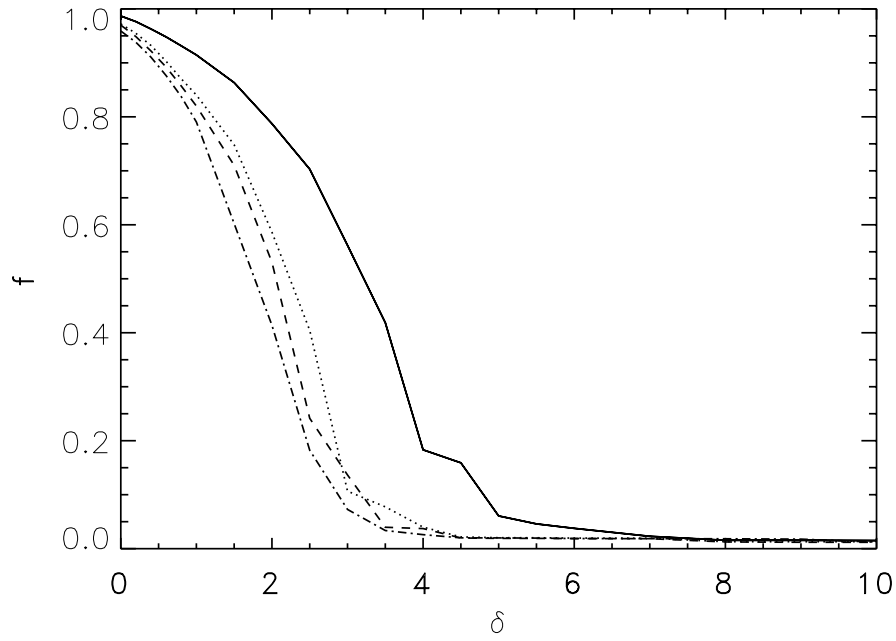
Figure 4.3.: Fraction of the overdense mass in the largest object as a function of the overdensity for the four models: τCDM (solid), ΛCDM (dotted), OCDM (dashed), and SCDM (dot dashed).
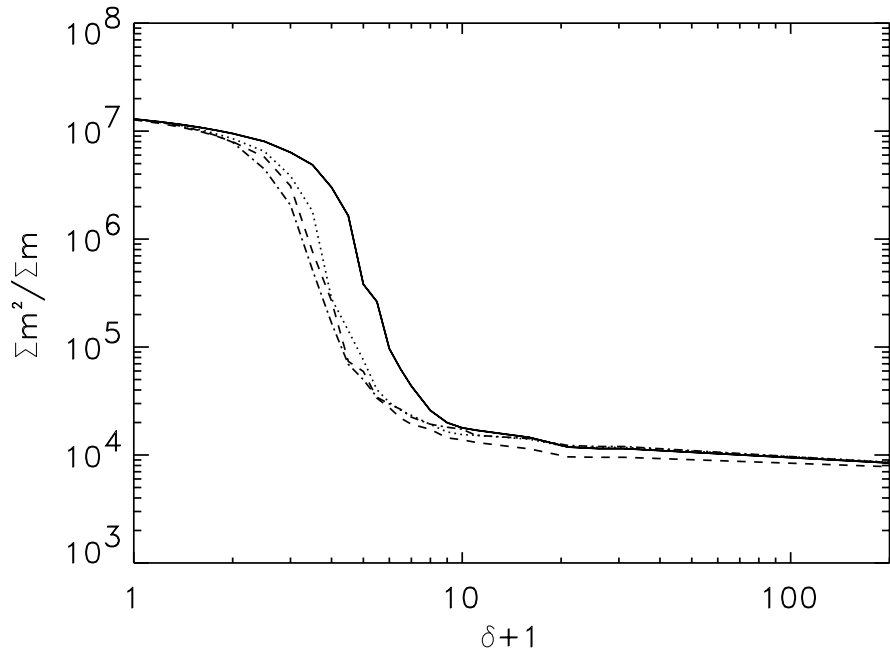
Figure 4.4.: $\Sigma m^2/\Sigma m$ (where the sum is over all objects) as a function of the overdensity for the four models: τCDM (solid), ΛCDM (dotted), OCDM (dashed), and SCDM (dot dashed).
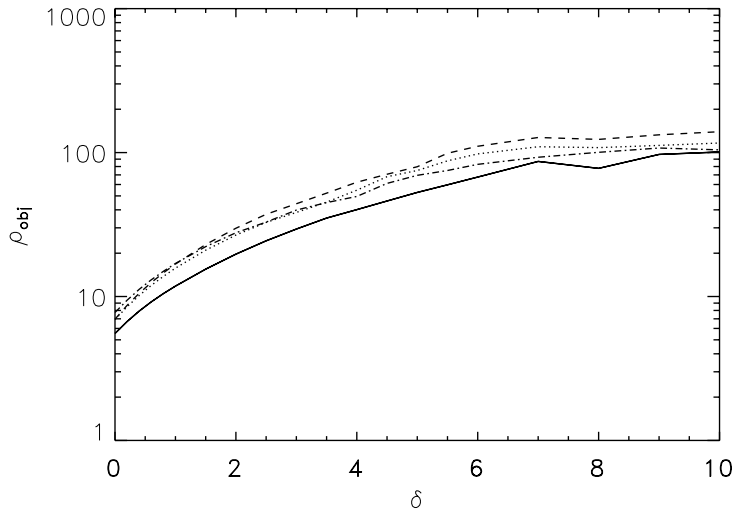
Figure 4.5.: Density of the largest object (in units of the particle masses) as a function of the overdensity for the four models: τCDM (solid), ΛCDM (dotted), OCDM (dashed), and SCDM (dot dashed).
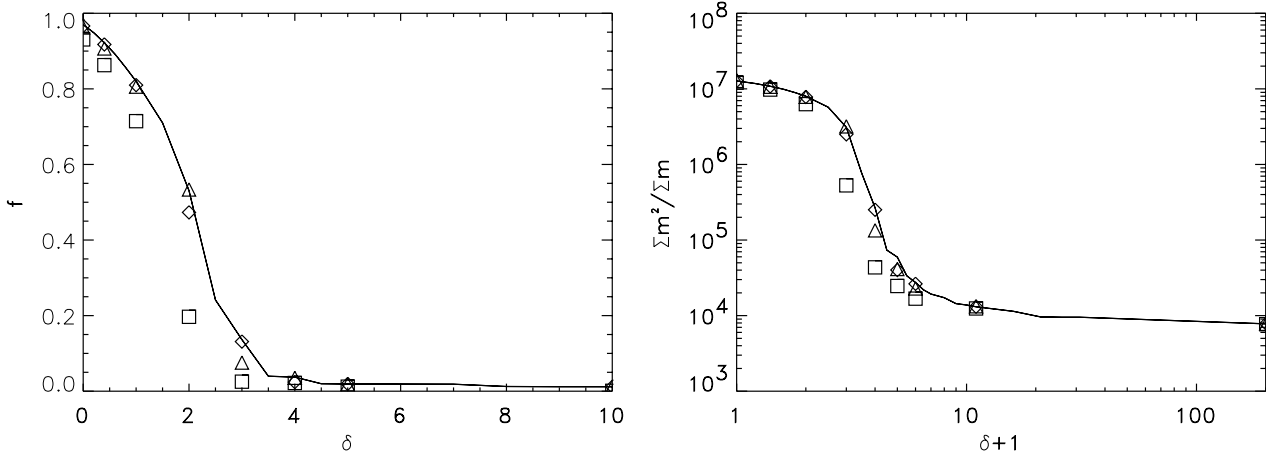
Figure 4.6.: Lefthand panel: Fraction of the overdense mass in the largest object as a function of the overdensity for OCDM (solid line). Righthand panel: $\Sigma m^2/\Sigma m$ (where the sum is over all objects) as a function of the overdensity for OCDM (solid line). Symbols denote sets with 50% (diamonds), 30% (triangles),and 12.5% (boxes) of all particles.
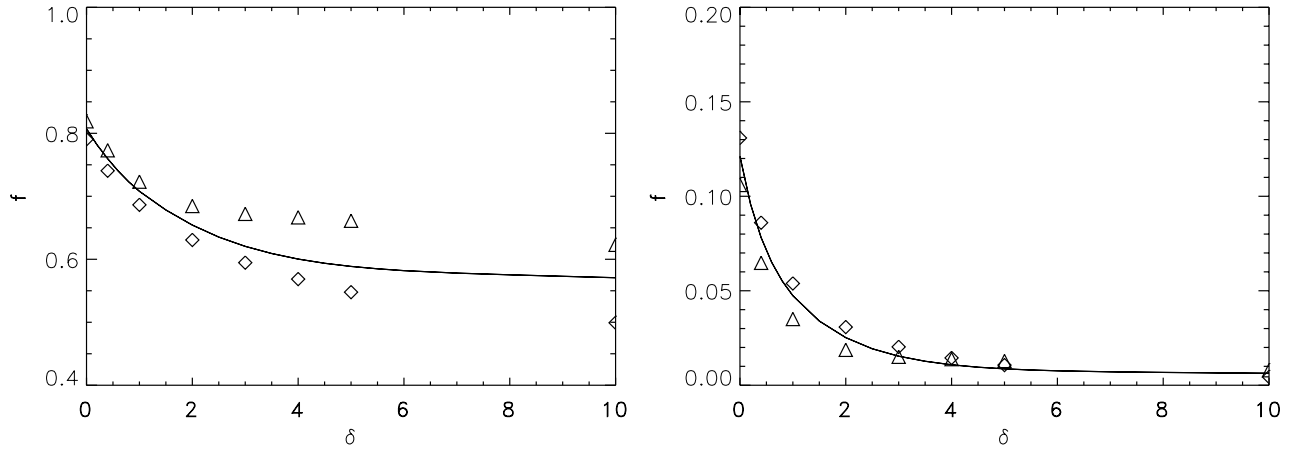
Figure 4.7.: Lefthand panel: Fraction of mass above overdensity threshold as a function of the overdensity for OCDM (solid line). Righthand panel: Fraction of the volume occupied by all objects above overdensity threshold as a function of the overdensity for OCDM (solid line). The solid lines give the results if 30 neighbours are required for the adaptive smoothing. Symbols denote density fields obtained with 15 (triangles) and 60 (diamonds) neighbours.

no effect at all on the total overdense volume. Only for the most extreme downsampling is the total overdense mass slightly increased (a few %). The lefthand panel of fig. 4.6 shows the change in the fraction of overdense mass in the largest obect. The change in the occupied volume looks similar. The righthand panel of fig. 4.6 gives $\Sigma m^2/\Sigma m$. Decreasing the number of particles has a significant effect only for the sparsest sample. There, percolation stops at a lower overdensity threshold. This must be clearly due to the destruction of some of the thin bridges which can be seen in the visual representations of the largest object seen above. The general result, however, remains unchanged.

As already indicated above, the number of neighbours required for the adaptive smoothing is arbitrary. In order to investigate the effect a change in this number has two test cases were carried out. The number of neighbours was doubled and halved. Recall that the number of neighbours influences the size of the smoothing kernel. Fig. 4.7 shows the effect the change in the required number of neighbours has on the total overdense mass (lefthand panel) and its occupied volume (righthand panel). Decreasing the number of neighbours decreases the occupied volume and increases the total overdense mass while increasing the number of neighbours has the opposite effect. If more neighbours are required the region into which the matter is smeared out becomes larger. In addition, more of massive objects falls below threshold after smoothing. These two points account for the decrease in the overdense mass and the increase in the occupied volume. The same argument can be inverted and then adapted to the corresponding case.

An increase in the number of required neighbours should not effect the percolation properties much. Recall that these properties depend mainly on the coherence of the mass, that is on detecting the thin bridges. However, decreasing the number of neighbours destroys some of the very thin bridges. Fig. 4.8 supports this point of view. It can be concluded that the number

51
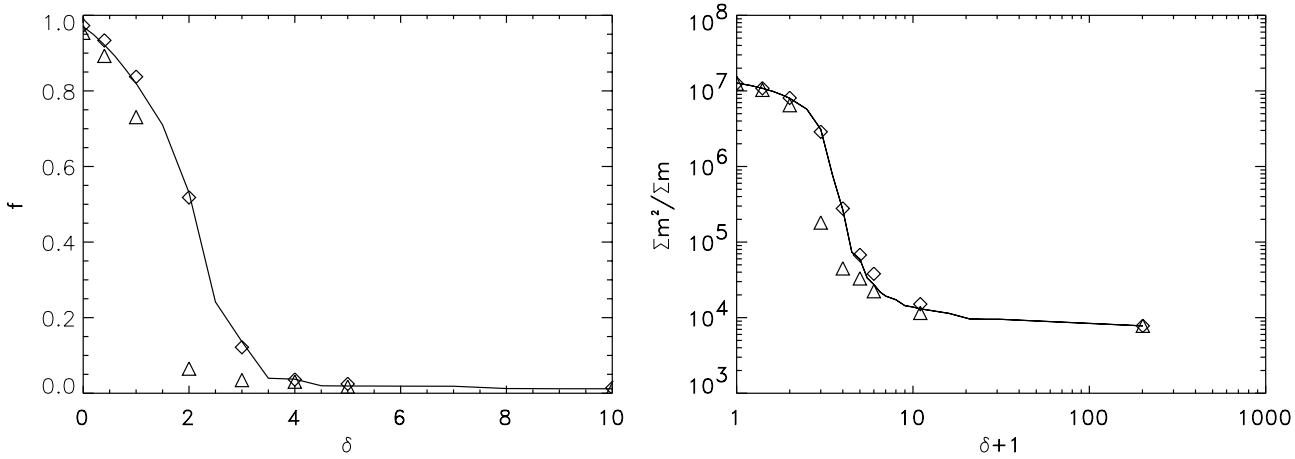
Figure 4.8.: Lefthand panel: Fraction of the overdense mass in the largest object as a function of the overdensity for OCDM (solid line). Righthand panel: $\Sigma m^2/\Sigma m$ (where the sum is over all objects) as a function of the overdensity for OCDM (solid line). The solid lines are obtained by requiring 30 neighbours for the adaptive smoothing. Symbols denote density fields obtained with 15 (triangles) and 60 (diamonds) neighbours.

of neighbours chosen here is appropriate to guarantee that bridges stay intact.

4.2.5. Shape Diagnostics

Introduction

For more than a decade now the topology and geometry of Large–Scale Structure (LSS) have been a topic of interest. The basic underlying question was and still is whether any of the cosmological models reproduces the observed coherent structure. If this were the case would it then be possible to distinguish between different cosmologies and even to favour a particular cosmology? Generally speaking, the idea was to invoke an alternative descrption to the two–point correlation function which will be introduced in detail in Chapter 6 and to describe both the connectedness of the structure in galaxy catalogs and in simulations and the geometry of the structure. For instance, if structure in the Universe grew from a cosmic string scenario rather than the Cold Dark Matter (CDM) scenario it could be expected that the distribution of mass is significantly different than what is found in CDM simulations.

In 1986, Gott et al. introduced the genus statistics in cosmology. The genus statistics gives the number of topological holes minus the number of connected regions. So a sphere has genus -1, a doughnut 0, etc. About a decade later, in the most recent study Springel et al. (1998) showed that even the usage of the most sophisticated techniques in combination with the Virgo simulations and the IRAS 1.2–Jy Redshift Survey cannot decisively distinguish among the models which have a power spectrum consistent with galaxy clustering, that is τCDM, ΛCDM, and OCDM (for earlier works see references in Springel et al.; essentially the same analysis was done for the Point Source Catalogue Redshift Survey in Canavezes et al. 1998 which lead to the same conclusions). As pointed out by Springel et al. the genus statistics may be only really

useful to test the random phase hypothesis, and τCDM, ΛCDM, and OCDM all resemble the observational data quite closely.

Various other methods have been proposed to describe the geometrical properties of LSS. They assume that LSS consists of either sheets, filaments, or clusters, or a mix of them. Thus, different functionals were developed with a supposed strong discriminative power amongst these three structure elements (see e.g. Sahni et al. 1998 and references therein). However, most of these methods suffer from the fact that they work nicely only for the simplest test cases. It is nice to see that some functional indeed gives more or less the expected behaviour for, say, a cylinder, but three dimensional representations of LSS like the ones shown above look much more complicated. This effect usually lead to the problem that results obtained with these functionals are very hard to interpret.

Minkowski functionals, introduced by Mecke et al. (1994) into cosmology, have a sound mathematical background. It can be shown that the morphological properties of a compact surface can be described by four functionals. The Minkowksi functionals are the volume V, the surface area S, the integrated mean curvature $C = \frac{1}{2} \int (\kappa_1 + \kappa_2) \, \mathrm{d}S$, and the genus $G = -1/4\pi \int \kappa_1 \kappa_2 \, \mathrm{d}S$, where $\kappa_1 = 1/R_1$ and $\kappa_2 = 1/R_2$ are the principal curvatures of the surface. Applications of the Minkowski functionals to galaxy or cluster catalogs have so far yielded results quite similar to those ones obtained with the genus statistics alone (e.g. Kerscher et al. 1998).

Apart from the shape statistics with its inherent problems, the genus statistics and Minkowski functionals have mainly suffered from the fact that existing galaxy catalogs and simulations too sparsely sample the underlying density field. Thus, the possible signal was dominated by noise. In addition, the discriminative power between cosmological models is rather small. These methods are used here to study the adaptively smoothed density fields already investigated above. Sampling is not an issue.

Applications

First, the Minkowski functionals of the adaptively smoothed density field for all objects above the overdensity threshold are computed[2]. The same is done for the largest object only. As an example, Fig. 4.9 shows the Minkowski functionals of the τCDM simulation. Shown are the functionals of all objects (dotted line), of the largest object (solid line), and of the difference of the two (dashed line). Note that the volume and the surface given here are in fact volume and surface fractions (see Schmalzing & Buchert 1997 for the definitions of the functionals used here). The volume (top left) agrees with what was already seen above (fig. 4.2). All of the functionals very nicely show how percolation breaks down for large overdensities. The genus is particularly interesting. Recall that it gives the number of holes minus the number of connected regions. Not surprisingly, the largest object has a huge number of holes for overdensities $\delta < 2$. The dashed line gives the combined genus of all other objects. The genus is an additive quantity. As can be seen from the figure, the combined genus of these objects is negative for these overdensities. The visual impression of fig. A.9 already showed that apart from the largest object a plethora of small rather simple objects exists. The number of these

---

[2]The code used here was kindly provided by Schmalzing and is described in Schmalzing & Buchert (1997).
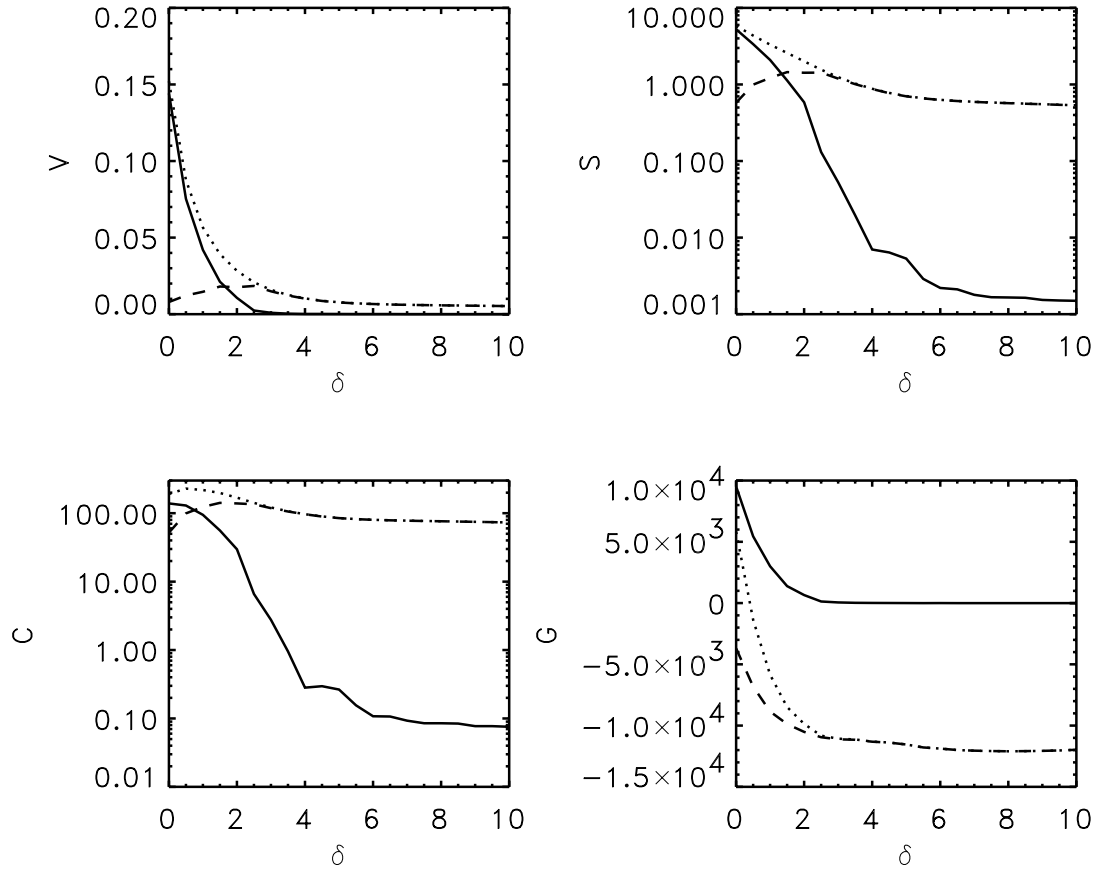
Figure 4.9.: The Minkowski functionals for the adaptively smoothed density field of the τCDM simulation: Volume V (top left), surface area S (top right), integrated mean curvature C (bottom left), and genus G (bottom right). Shown are largest object (solid line), all objects (dotted line), and the difference between these two (dashed line).
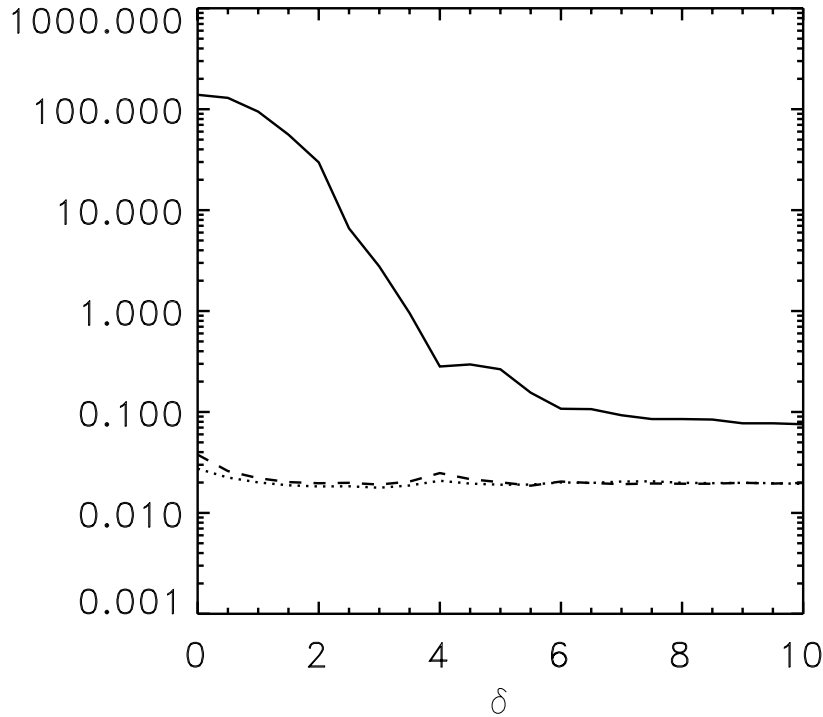
Figure 4.10.: The quantities $H_1 = V/S$ (dotted line), $H_2 = S/C$ (dashed line), and $H_3 = C$ (solid line) where V, S, and C are Minkowski functionals of the biggest object as shown in fig. 4.9.

objects can be seen from the dashed line because each of such objects contributes -1 to the total genus.

Apart from the connectedness and geometry of LSS, the sizes of typical objects are of particular interest. In principle, these should be measurable – at least on average. Assume the only object is a perfect filament, i.e. a cylinder of length l and radius r (where $l \gg r$). The cylinder's volume and surface then are $V = \pi r^2 l$ and $S = 2\pi r l$, respectively. Dividing these by each other gives $V/S = r/2$. Thus, if the volume and surface are know, the radius can be computed. Sahni et al. (1997) used such considerations to propose the three functionals $H_1 = V/S$, $H_2 = S/C$, and $H_3 = C$ where V, S, and C are the Minkowski functionals discussed above. These three functionals all have dimensions of a length. For the simplest cases, i.e. sheets, filaments, or spheres, the functionals H_i represent the three major axes so that $H_1 \ll H_2 \simeq H_3$, $H_1 \simeq H_2 \ll H_3$, and $H_1 \simeq H_2 \simeq H_3$ for a sheet, filament, and sphere, respectively. As seen in the pictorial representations of LSS, the biggest object is definitely not such a simple object. Filaments of various sizes and thicknesses tend to dominate. Thus, by computing the functionals H_i, averages will be obtained. These may nevertheless yield some information about, say, an average thickness of the filaments – if filaments really are dominant. In fig. 4.10, these three functionals of the biggest object as computed from the Minkowski functionals shown in fig. 4.9 are plotted. For high overdensities, say $\delta = 100$, which is outside the plot range $H_1 \simeq H_2 \simeq H_3$. The three curves reinforce the visual impression that filaments clearly dominate for overdensities of about $\delta < 4$. At high overdensities, the biggest object seems to be more or less spherical. The latter point is not surprising because

55

at high overdensities, the biggest objects coincide with the most massive clusters which have elliptical shapes (for a discussion of such properties, see Thomas et al. 1998). The quantity H_1 drops slightly from $\delta = 0$ to $\delta = 1.5$ and then remains roughly constant. Using the conventions for the normalizations of the Minkowski functionals (see Schmalzing & Buchert 1997) H_1 can be transformed into absolute length scales – which amounts to dividing its value in fig. 4.10 by six. As indicated above, for low overdensities, the biggest object appears to be filamentary. In this case, the transformed length scale corresponds to $r/2$. r would then be of the order of around just 2.5 (2.0) mesh cells for $\delta = 0$ ($\delta = 1$). Of course, this is an *average* number. But it shows that a much finer mesh would be necessary to infer more precise information about typical length scales of the structure. With the techniques used here, that is a three-dimensional mesh, this is simply beyond the computational resources of the post–processing computers at the RZG.

4.3.   Conclusions

Large–Scale Structure in the high–resolution GIF simulations has emerged as a very complex network for overdensities of about $\delta < 4$ for the four cosmological models. For very low overdensity thresholds, most of the overdense mass is contained in one single object which extends all across the simulation volume – it percolates. In addition, a plethora of small isolated objects is present, too. The overall overdense volume is only slightly above the 10% level, though. If the overdensity threshold is increased, the overdense volume shrinks rapidly, the overdense mass decreases, albeit more gently, and the biggest object loses more and more mass. At overdensity thresholds of around $\delta \approx 4$, the biggest object contains only a few percent of the overdense mass. There are differences between the cosmological models which can be explained in terms of their power spectra and their different dynamical history. These results do not depend crucially on systematical effects.

Using Minkowski functionals sheds just a little bit more light onto the preceding. The genus allows estimates of the number of small objects. It appears as if the biggest object had an overall filamentary (spherical) structure for low (high) overdensities[3]. However, with the fixed grid used to obtain the adaptively smoothed density field, it is rather difficult to compute typical length scales of the biggest object. For mean density, the typical diameter of a filament is only about 2.5 mesh cells for the τCDM model. It then decreases to about 1.5 mesh cells for $\delta \approx 5$. Clearly, a much finer mesh is needed to get more precise results.

Acknowledgements

---

[3]Of course, for $\delta \approx 100$ and larger this can be seen from pictures, too.

Bibliography

[1] Canavezes A., Springel V., Oliver S.J., Rowan–Robinson M., Keeble O., White S.D.M., Saunders W., Efstathiou G., Frenk C.S., McMahon R.G., Maddox S., Sutherland W., Tadros H., accepted by MNRAS, 297, 777 (1998)

[2] Colberg J.M., White S.D.M., Jenkins A., Pearce F.R., submitted to MNRAS, astro-ph/9711040

[3] Couchman H.M.P., Thomas P.A., Pearce F.R., ApJ, 452, 797 (1995)

[4] Davis M., Efstathiou G., Frenk C.S., White S.D.M., ApJ, 292, 371 (1985)

[5] Efstathiou G., Davis M., Frenk C.S., White S.D.M., ApJS, 57, 241 (1985)

[6] de Lapparent V., Geller M.J., Huchra J.P., ApJ, 302, L1 (1986)

[7] Gott J.R., Melott A.L., Dickinson M., ApJ, 306, 341 (1986)

[8] Haynes M.P., Giovanelli R., ApJ, 306, L55 (1986)

[9] Hernquist L., Katz N., ApJ, 70, 419 (1989)

[10] Jenkins A., Frenk C.S., Pearce F.R., Thomas P.A., Hutchings, Colberg J.M., White S.D.M., Couchman H.M.P., Peacock J.A., Efstathiou G.P., Nelson A.H., "The VIRGO Consortium: Simulations of Dark Matter and Galaxy Clustering", in Dark and Visible Matter in Galaxies and Cosmological Implications, ed.s Persic M., Salucci P., ASP Conference Series (1996)

[11] Jenkins A., Frenk C.S., Pearce F.R., Thomas P.A., Colberg J.M., White S.D.M., Couchman H.M.P., Peacock J.A., Efstathiou G.P., Nelson A.H. (The Virgo Consortium), astro-ph/9709010

[12] Kerscher M., Schmalzing J., Buchert T., Wagner H., A&A, 333, 1 (1998)

[13] Kirshner R.P., Schechter P.L, Shectman S.A., ApJ, 248, L57 (1981)

[14] Lindner U., Einasto M., Einasto J., Freudling W., Fricke K., Lipovetsky V., Pustilnik S., Izotov Yu., Richter G., A&A, 314, 1 (1996)

[15] Mecke K.R., Buchert T., Wagner H, A&A, 288, 697 (1994)

[16] Pearce F.R., Couchman H.M.P., Jenkins A.R., Thomas P.A., 'Hydra – Resolving a parallel nightmare', in Dynamic Load Balancing on MPP systems (1995)

[17] Pearce, F.R., Couchman, H.M.P., "Hydra: A parallel adaptive grid code", submitted to New Astronomy (1997)

[18] Sahni V., Sathyaprakash B.S., Shandarin S.F., ApJ, 495, L5 (1998)

[19] Schmalzing J., Buchert T., ApJ, 482, L1 (1997)

[20] Shandarin S.F, Soviet Astron. Lett., 9, 104 (1983a)

[21] Shandarin S.F, Zel'dovich Ya.B., Comments Astrophys., 10, 33 (1983b)

[22] Springel V., White S.D.M., Colberg J.M., Couchman H.M.P., Efstathiou G.P., Frenk C.S., Jenkins A., Pearce F.R., Nelson A.H., Peacock J.A., Thomas P.A. (The Virgo Consortium), accepted by MNRAS

[23] Thomas P.A., Colberg J.M., Couchman H.M.P., Efstathiou G.P., Frenk C.S., Jenkins A., Nelson A.H., Hutchings R.M., Peacock J.A., Pearce F.R., White S.D.M. (The Virgo Consortium), MNRAS, 296, 1061 (1998)

[24] Vogeley M.S., Park C., Geller M.J., Huchra J.P., Gott J.R., ApJ, 420, 525 (1994)

[25] Yess C., Shandarin S.F, astro-ph/9605041

[26] Zel'dovich Ya.B., Soviet Astron. Lett., 8, 102 (1982)

Chapter 5
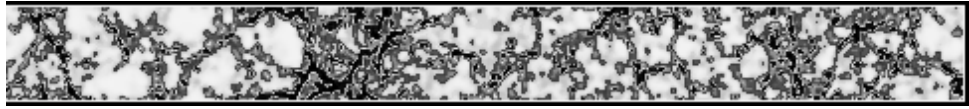
Peculiar Velocities of Galaxy Clusters

5.1. Introduction

Clusters of galaxies are well–studied objects. Observationally, they can be found rather easily. For example, they show up either as enhancements of the number density of galaxies on photographic plates or as strong enhancements in the X–ray flux on the sky. Though easy to find, they are rare ($N \approx 10^{-5} - 10^{-6} \, h^3 \, \mathrm{Mpc}^{-3}$), and their properties are difficult to study. Consider the mass of a cluster. Until the advent of X–ray astronomy, the masses of galaxy clusters were estimated from the motions of their constituent galaxies using the assumption of virial equilibrium. In addition to the possibility that this assumption is not always satisfied, the inclusion of galaxies in the foreground or background can lead to large errors.

X–ray astronomy, with satellites like *Einstein* and *ROSAT*, has made it possible to measure the X–ray emission of the hot intracluster gas. As the X–ray emission is proportional to ρ^2, where ρ is the density of the gas, the strongest contribution comes from the centers of clusters – unless two clusters are merging. For the latter case, strong shocks show up which, crudely speaking, appear at the collision front of the two colliding systems and which lead to a shock heating of the gas. The assumption of hydrostatic equilibrium again allows an estimate of the mass of a cluster once its X–ray temperature is given.

New telescopes, especially the Hubble Space Telescope, have made it possible to obtain images of galaxy clusters at very high resolution. On these images, some clusters show arcs, that is distorted images of background objects. This effect demonstrates that clusters act as gravitational lenses. The gravitational arcs can be used to measure the total mass or even the mass distribution of a cluster. The caveat here is that it is actually the *projected* mass that is is measured. So if two objects happen to lie along the same line–of–sight, lensing alone measures their combined mass. Independent measurements of lensing masses, galaxy velocity dispersions, and the X–ray temperature are desirable to provide consistency checks. However, the measurements do not always agree and quite often the source of the discrepancy is not obvious. The uncertainties arising from these measurements have to be borne in mind in this and

the following Chapter, where properties of galaxy clusters are investigated theoretically.

The measurement of the velocity of a cluster is also affected by some of the uncertainties mentioned above. In order to measure the velocity of a cluster, its distance must be determined independently from its redshift. This is because there are two contributions to a galaxy's observed redshift: the component associated with the expansion of the Universe, and the component arising from the galaxy's proper motion with respect to the local rest frame (peculiar velocity). As distance indicators, the empirical Tully–Fisher and $D_n - \sigma$ relations are used for spiral and elliptical galaxies, respectively. These relations relate the galaxy's luminosity to its kinematics. For spiral galaxies, the relation is an approximate consequence of their near constant surface brightness. If centrifugal equilibrium is assumed,

$$v_{\mathrm{rot}}^2 \propto \frac{M}{R} \,, \tag{5.1}$$

where v_{rot}, M, and R are the galaxy's rotation velocity, its mass, and radius, respectively. If a universal mass–to–light ratio (M/L) and a constant mean surface brightness $\bar{I}$ are assumed, so that

$$L \propto \bar{I} R^2 \,, \tag{5.2}$$

one gets

$$L \propto v_{\mathrm{rot}}^4 \,. \tag{5.3}$$

This is the Tully–Fisher relation in the infrared band. For other wavelengths, the exponent ("slope") changes slightly (see Strauss & Willick 1996 for a very detailed review of this subject). However, the observed scatter around the Tully–Fisher relation is remarkably small. For elliptical galaxies, similar arguments lead to the analogous $D_n - \sigma$ relation. Thus, if the rotation velocity (velocity dispersion) of a spiral (elliptical) galaxy is measured, its luminosity, and from this, its distance can be inferred as follows. The conventional notation of astronomers recasts eq. (5.3) as

$$M(\eta) = A - b\,\eta \,, \tag{5.4}$$

where $M = \mathrm{const.} - 2.5 \log L$ is the absolute magnitude, and

$$\eta \equiv \log[2\,v_{\mathrm{rot}}] - 2.5 \,, \tag{5.5}$$

is a conventional measure of the rotation velocity (which is measured in km/sec). A and b are called the zeropoint and the slope of the Tully–Fisher relation, respectively (for details see Strauss & Willick 1996). The observed quantity is the apparent magnitude m which is related to the absolute magnitude via

$$m = M + 5 \log r \,, \tag{5.6}$$

where r is the distance to the galaxy. The rotation velocities of spirals can be measured by analysis of HI 21 cm–profiles or by measuring the blueshifting and redshifting of the Hα emission line at the parts of the galaxy that are rotating towards or away from the observer. Once the distance to the galaxy is known, its peculiar velocity can be computed.

Theoretically, galaxy clusters are "nice" objects. They are massive; this mass must have assembled from a very large region in the early Universe. Therefore, it may be reasonable

to assume that e.g. the fraction of gas in clusters is the same as the global gas fraction. The assumption of an inflationary CDM cosmogony – as is made here – has further consequences. Depending on the actual value of the density parameter Ω_0, the median formation redshift of a cluster is $z \approx 0.3$ or later. This means that in the hierarchy of objects, galaxy clusters form last.

The motions of galaxy clusters are thought to result from gravitational forces acting over the very large scales on which superclusters are assembled. The *rms* deviations from uniformity on such scales appear to be small, and so may be adequately described by the linear theory of fluctuation growth. For a linear density field of given power spectrum the *rms* peculiar velocity is proportional to $\sigma_8 \Omega_0^{0.6}$ where σ_8 is the *rms* mass fluctuation in a sphere of radius $8\ h^{-1}$ Mpc as introduced in Chapter 2, section 2.3.4. There, it was mentioned that essentially the same parameter combination can also be estimated from the *abundance* of galaxy clusters. A comparison of the two estimates could in principle provide a check on the shape of the assumed power spectrum and on the assumption that the initial density field had Gaussian statistics. In practice this is difficult because of the uncertainties in relating observed cluster samples to the objects for which quantities are calculated in linear theory or measured from N-body simulations.

The standard linear model was introduced by Bardeen et al. (1986). It assumes that clusters can be identified with "sufficiently" high peaks of the linear density field after convolution with a "suitable" smoothing kernel. The peculiar velocity of a cluster is identified with the linear peculiar velocity of the corresponding peak extrapolated to the present day. In this Chapter, the limitations both of this model and of direct N–body simulations are studied by comparing their predictions for clusters on a case by case basis.

5.2. Linear Theory Predictions for the Peculiar Velocities of Peaks

5.2.1. The Growth of Peculiar Velocities

Chapter 2 decribed the growth of peculiar velocities according to linear theory. The following scaling was derived:

$$v \propto f(a)\, g(a)\, a^2 \sqrt{\Omega_0\, a^{-3} + (1 - \Omega_0 - \Lambda_0)\, a^{-2} + \Lambda_0}\,. \tag{5.7}$$

Here, $f \approx \Omega_0^{0.6}$, and g describes how much the growth factor D deviates from the $\Omega_0 = 1$ case, where $D = a$ and $g = 1$. For the simple Einstein-de Sitter case where $\Omega_0 = 1$ and $\Lambda = 0$, this formula reduces to the exact result $v \propto \sqrt{a}$.

5.2.2. The Velocities of Peaks

The idea that the statistical properties of nonlinear objects like galaxy clusters can be inferred from the initial linear density field was developed in considerable detail in the monumental paper of Bardeen et al. (1986). If the initial fluctuations are assumed to be Gaussian, they are

specified completely by their power spectrum, $P(k)$. Similarly, any smoothed version of this initial field is specified completely by its own power spectrum, $P(k)W^2(kR)$, where $W(kR)$ is the Fourier transform of the spherical smoothing kernel and R is a measure of its characteristic radius. In particular, Bardeen et al. showed how the abundance and *rms* peculiar velocity of peaks of given height can be expressed in terms of integrals over $P(k)W^2(kR)$. The difficulty in connecting this model with real clusters lies in the ambiguity in deciding what smoothing kernel, characteristic scale, and peak height are appropriate. Typically the smoothing kernel is taken to be a Gaussian or a Top–Hat, R is chosen so that the kernel contains a mass similar to the minimum mass of the cluster sample, and the peak height is assumed to be sufficiently high for a spherical perturbation to collapse by $z = 0$.

The smoothed initial peculiar velocity field is isotropic and Gaussian with a three-dimensional dispersion given by

$$\sigma_{\rm v}(R) \equiv H \, \Omega^{0.6} \, \sigma_{-1}(R) \,, \tag{5.8}$$

where, in the notation of Bardeen et al. (1986), σ_j is defined for any integer j by

$$\sigma_j^2(R) = \frac{1}{2\pi^2} \int P(k) \, W^2(kR) \, k^{2j+2} \, {\rm d}k \,. \tag{5.9}$$

The *rms* peculiar velocity at peaks of the smoothed density field differs systematically from $\sigma_{\rm v}$; Bardeen et al. show that it is given by

$$\sigma_{\rm p}(R) = \sigma_{\rm v}(R)\sqrt{1 - \sigma_0^4/\sigma_1^2\sigma_{-1}^2} \,. \tag{5.10}$$

Note that this expression does not depend on the height of the peaks. As shown in Bardeen et al. , the velocities of peaks are *statistically* independent of their height.

The parametric expression of the power spectrum used here was introduced in Chapter 2 (Bond & Efstathiou 1984),

$$P(k, \Gamma) = \frac{Ak}{\{1 + [ak/\Gamma + (bk/\Gamma)^{3/2} + (ck/\Gamma)^2]^\nu\}^{2/\nu}} \,, \tag{5.11}$$

where $a = 6.4 \, h^{-1} \, {\rm Mpc}$, $b = 3.0 \, h^{-1} \, {\rm Mpc}$, $c = 1.7 \, h^{-1} \, {\rm Mpc}$, $\nu = 1.13$. Γ is the shape parameter.

In the following, linear density fields are smoothed either with a Top–Hat ($W_{\rm TH}(x) = 3\,(x \sin x - \cos x)/x^3$) or with a Gaussian ($W_{\rm G}(x) = \exp[-x^2/2]$). It is unclear for either filter how R should be chosen in order to optimize the correspondance between peaks and clusters. Here, previous practice is followed in assuming that cluster samples contain all objects with mass exceeding some threshold $M_{\rm min}$, and then choosing R so that the filter contains $M_{\rm min}$. Hence, $M_{\rm min} = 4\pi\bar{\rho}R^3/3$ in the Top–Hat case and $M_{\rm min} = (2\pi)^{3/2}\bar{\rho}R^3$ in the Gaussian case. Cluster samples will be isolated at $M_{\rm min} = 3.5 \times 10^{14}h^{-1}{\rm M}_\odot$, the value appropriate for Abell clusters of richness one and greater (e.g. White et al. 1993). A detailed discussion of filtering schemes can be found in Monaco (1998) and references therein.

Table 1.1 gives characteristic filter radii R and values of $\sigma_{\rm v}$ and $\sigma_{\rm p}$ from equations (5.8) and (5.10) for both smoothings and for the set of Virgo models which is considered in this Chapter. The velocity dispersions are extrapolated to the linear values predicted at $z = 0$ using

Model	Top–Hat full $P(k)$			Gaussian full $P(k)$			Top–Hat simulated $P(k)$			Gaussian simulated $P(k)$		
	R	$\sigma_{\rm v}$	$\sigma_{\rm p}$	R	$\sigma_{\rm v}$	$\sigma_{\rm p}$	$\sigma_{\rm v}$	$\sigma_{\rm p}$	Δ	$\sigma_{\rm v}$	$\sigma_{\rm p}$	Δ
OCDM	10.3	390	349	6.6	366	315	351	300	0.94	321	258	0.96
ΛCDM	10.3	413	370	6.6	387	334	371	318	0.98	340	272	1.03
SCDM	6.9	381	334	4.4	349	290	375	325	0.58	342	278	0.60
τCDM	6.9	509	464	4.4	485	430	464	412	0.57	437	371	0.58

Table 5.1.: For each of the models, the following quantities are given: the radius R (second and fifth column) of the filter used in eq. (5.9), the three–dimensional velocity dispersions $\sigma_{\rm v}$ and $\sigma_{\rm p}$ (third, fourth, sixth, and seventh column) obtained using eq.s (5.8) and (5.10) with the given filter radii; the three–dimensional velocity dispersions $\sigma_{\rm v}$ and $\sigma_{\rm p}$ (eighth, ninth, eleventh, and twelvth column) obtained using eq.s (5.8) and (5.10) with the given filter radii and the power spectra of the simulations themselves; the *rms* linear overdensity Δ (tenth and thirteenth column) smoothed with the given filter radii and extrapolated to $z = 0$. The radii are in Mpc/h, and velocity dispersions are in km/sec.

eq. (5.7). The difference between $\sigma_{\rm v}$ and $\sigma_{\rm p}$ has often been ignored in the literature when predicting the peculiar velocities of galaxy clusters (e.g. Croft & Efstathiou 1994; Bahcall & Oh 1996; Borgani et al. 1997); for the models the two differ by about 15%. With the choice of filter radii adopted here, Gaussian smoothing predicts *rms* peculiar velocities about 10% smaller than Top–Hat smoothing. This is due to the Fourier transforms of the filters. A Gaussian transforms into a Gaussian in Fourier space. A Top–Hat transforms into an oscillating function which lets power from smaller scales leak in.

5.3.   The Simulation Set

For this Chapter, the set of Virgo simulations is used (see Chapter 3). Recall that these simulations follow the evolution of structure within a cubic region $240\ h^{-1}$ Mpc on a side using 256^3 equal mass particles. In all models the initial fluctuation amplitude, and so the value of σ_8, was set by requiring that the models reproduce the observed abundance of rich clusters. Note that each Fourier component of the initial fluctuation field had the same *phase* in each of these four simulations. As a result there is an almost perfect correspondance between the clusters in the four models.

Because of their finite volume, these simulations contain no power at wavelengths longer than $240\ h^{-1}$ Mpc. Furthermore, Fourier space is sampled quite coarsely on the largest scales for which they do contain power, and so realisation to realisation fluctuations on these scales can be significant. The size of the effects can be judged from Table 5.1 where the values of $\sigma_{\rm v}$ and $\sigma_{\rm p}$ are listed obtained for each model when the theoretical power spectrum is replaced in equations (5.8) and (5.10) by the initial power spectrum of the model itself. These are systematically smaller than the values found before. The difference is primarily a reflection of the

loss of large-scale power.

Model	Theory Top–Hat σ_{Peak}	Theory Gaussian σ_{Peak}	N_{Cl}	Simulations Top–Hat σ_{Peak}	Simulations Gaussian σ_{Peak}	σ_{lin}	$\sigma_{z=0}$
OCDM	300	258	62	253	266	280	407
ΛCDM	318	272	69	296	323	300	439
SCDM	325	278	92	308	318	307	425
τCDM	412	371	70	392	399	398	535

Table 5.2.: For each of the models, the following quantities are given: the three–dimensional velocity dispersions σ_{p} (second, third column) obtained using eq.s (5.8) and (5.10) with the power spectra of the simulations themselves (repeated from Table 5.1); the number of clusters N_{Cl} (fourth column) found in the simulations at $z = 0$; the three–dimensional velocity dispersions of peaks (fifth and sixth column) in the initial conditions of the simulations using the given filters; the three–dimensional linear velocity dispersions of clusters extrapolated to $z = 0$; and the three–dimensional measured velocity dispersion of clusters at $z = 0$. The radii are given in Mpc/h, the velocity dispersions in km/sec.

5.3.1. The Selection of Peaks

Peaks in the initial conditions of the simulations are identified by binning up the initial particle distribution on a 128^3 mesh using a cloud–in–cell (CIC) assignment (see e.g. Hockney & Eastwood 1981) and then smoothing with a Gaussian or a Top–Hat with characteristic scale R corresponding to $M_{\mathrm{min}} = 3.5 \times 10^{14} h^{-1} \mathrm{M}_\odot$. A peak is then taken to be any grid point at which the smoothed density is greater than that of its 26 nearest neighbours. The dimensionless height of a peak, ν, is defined by dividing its overdensity by the *rms* overdensity, Δ, which is listed in Table 5.1. Again, within the matched set there is a close correspondance between the peaks found in the four models. In addition, the peaks found with Gaussian smoothing correspond closely to those found with Top–Hat smoothing. Fig. 5.1 shows a slice through the density field of the SCDM simulation which contains a $\nu \approx 2.9$ peak and its environment.

Particle peculiar velocities are binned up and smoothed in an identical way and the peculiar velocity of a peak is taken to be the value at the corresponding grid point. In Table 5.2 the *rms* peculiar velocities of the peaks found in each model are listed. Again this is scaled up to the value expected at $z = 0$ according to linear theory. It differs slightly from the value predicted by inserting the power spectrum of the simulation directly into equation (5.10) because there are realisation to realisation fluctuations depending on the *phases* of the Fourier components. As it should, the *rms* peculiar velocity averaged over all grid points agrees very well with the value found by putting the simulation power spectrum into equation (5.8).
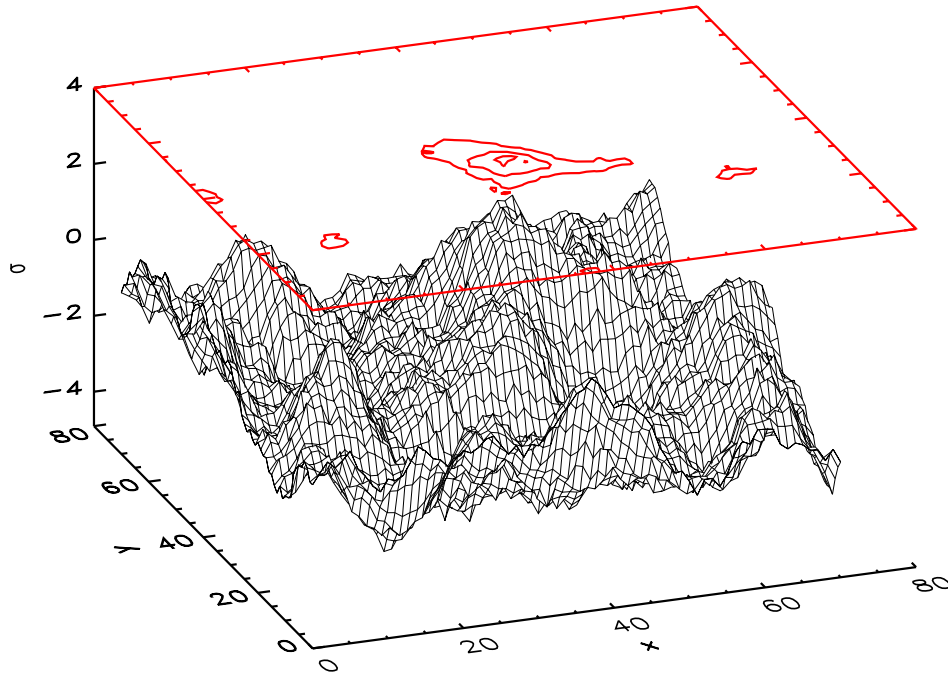
Figure 5.1.: A slice through the smoothed density field. The height of each mesh point is given in units of the *rms*. The contour levels shown are 1.0, 2.1, and 2.8. Right in the middle a peak with $\nu \approx 2.9$ shows up.

5.3.2. The Selection of Clusters

Clusters in the simulations are identified in the same way as in Croft & Efstathiou (1994). High-density regions at $z = 0$ are located using a friends–of–friends group finder with a small linking length (b=0.05), and their barycentres are considered as candidate cluster centres. Any candidate centre for which the mass within $1.5\,h^{-1}\,\mathrm{Mpc}$ exceeds $M_{\min}$ is identified as a candidate cluster. The final cluster list is obtained by deleting the lower mass candidate in all pairs separated by less than $1.5\,h^{-1}\,\mathrm{Mpc}$. This way of finding a cluster mimics very roughly the algorithm Abell (1958) used to select clusters from photographic plates.

Fig. 5.6 shows the particle positions for one of the clusters in the ΛCDM simulation at five different redshifts. The way the cluster is built up is typical for these hierarchical CDM universes. Small objects form first and then merge. In this particular case, the cluster is formed between a redshift of $z = 1$ and $z = 0.3$. Note that at $z = 0$ some small substructure is visible.

In Fig. A.15 a comparison between the evolution of a single cluster in the τCDM and the ΛCDM model is shown. The sizes of the regions are $21 \times 21 \times 8\,h^{-3}\,\mathrm{Mpc}^3$ and $35 \times 35 \times 14\,h^{-3}\,\mathrm{Mpc}^3$, respectively. As discussed in Chapter 2 and shown pictorially in Chapter 3, structure starts to form earlier in a low density model like ΛCDM. However, at $z = 0$ the same objects have formed at the same locations – this is due to the same phases of the initial density fluctuations in all four models.

In the following, only clusters more massive than $M_{\min} = 3.5 \times 10^{14}\,h^{-1}\,\mathrm{M}_\odot$ will be con-

sidered. The number of clusters found in each simulation is listed in Table 5.2. As already noted, the individual clusters in the different simulations of the matched set correspond closely. Despite the normalisation to cluster abundance, it appears as though the SCDM model has significantly more clusters than the other models. This is a reflection of its steeper power spectrum together with the value of $M_{\min}$ chosen. For $M_{\min} = 5.5 \times 10^{14} \, h^{-1} \, \mathrm{M}_\odot$ – which is very close to the mass threshold usually taken to fix σ_8 – all the models have about 20 clusters.

The peculiar velocity of each cluster at $z = 0$ is defined to be the mean peculiar velocity of all the particles within the $1.5 \, h^{-1} \, \mathrm{Mpc}$ sphere. The peculiar velocity of the cluster at earlier times is taken to be the mean peculiar velocity of these same particles. Consistent with this, the position of the cluster at each time is defined to be the barycentre of this set of particles. At $z = 0$ this is very close to, but not identical with the cluster centre as defined above. The *rms* values of the initial (linear) and final ($z = 0$) peculiar velocities of the clusters in each of the models are given in Table 5.2. The initial values have been scaled up to the linear values predicted at $z = 0$. It is clear that these substantially underestimate the actual values, a result discussed in more detail below.

5.4. Comparison of the Peak Model with Simulations

5.4.1. The Cluster-Peak Connection

The extent to which dark haloes can be associated with peaks of the smoothed initial density field is somewhat controversial. Frenk et al. (1988) concluded that, for appropriate choices of filter scale and peak height, the correspondance is good, whereas Katz et al. (1993) claimed that "there are many groups of high mass that are not associated with any peak". The result of correlating the peaks in the initial conditions of the simulations with the initial positions of the clusters is illustrated in Fig. 5.2. A peak and a cluster are considered to be associated if their separation is less than $4 \, h^{-1} \, \mathrm{Mpc}$ (comoving). The barycenters of 70% and 80% of the clusters with masses exceeding $3.5 \times 10^{14} \, h^{-1} \, M_\odot$ are associated with a peak with $\nu > 1.5$ for the low and high Ω models, respectively.

Fig. 5.2 shows that there is, as expected, a correlation between the height of a peak and the mass of the corresponding cluster. However, there is a big scatter. There are many possible explanations why not all clusters have an associated peak. The peak threshold is *not* the reason – lowering the threshold does not decrease the number of "isolated" clusters. Merging peaks and peaks which are disrupted have been discussed in the past. This is beyond the scope of this Chapter.

5.4.2. Linear Theory Velocities of Peaks and Clusters

Given the good correspondance between peaks of the smoothed linear density field and the initial positions of clusters, it is natural to compare the smoothed peculiar velocity at a peak with the mean initial peculiar velocity of its associated cluster[1]. In Fig. 5.3, such a comparison is shown, again based on Top–Hat smoothing of both position and peculiar velocity fields using

---

[1]This is done only for those clusters for which a peak actually could be associated.
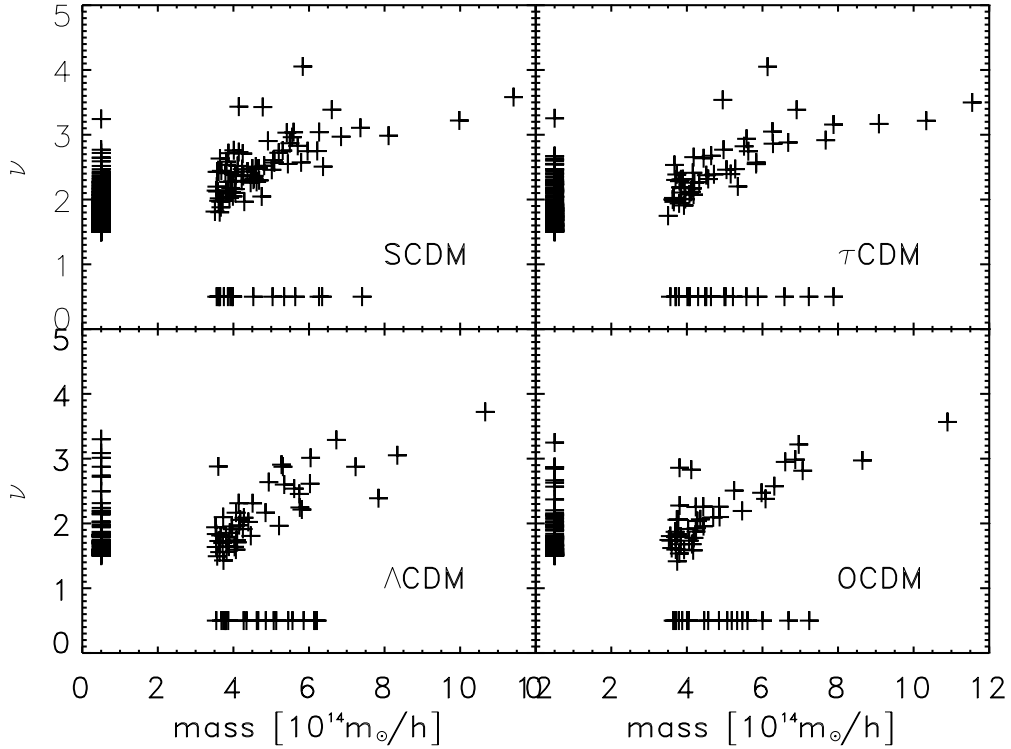
Figure 5.2.: The mass of the clusters in the simulations against the height of the corresponding peaks in the initial conditions, once these are smoothed with a Top–Hat with the characteristic radius listed in Table 5.2. All clusters with mass greater than $3.5 \times 10^{14} \, h^{-1} \, M_\odot$ and all peaks with height greater than $\nu = 1.5$ are shown. There are 351, 239, 84, and 83 unmatched peaks in the SCDM, τCDM, ΛCDM, and OCDM model, respectively. They are plotted at a mass of $0.5 \times 10^{14} \, h^{-1} \, M_\odot$. Unmatched clusters are plotted at $\nu = 0.5$.

the characteristic radii listed in Table 5.1. All velocities are scaled up to the expected value at $z = 0$ according to linear theory. The correlation is clearly very good in all cases, and is similar if Gaussian rather than Top–Hat smoothing is used. The *rms* difference in peculiar velocity between a cluster and its associated peak is 16%, 16%, 23%, and 17% of the corresponding σ_{p} value listed in Table 5.2 for the OCDM, ΛCDM, SCDM and τCDM simulations, respectively. The somewhat larger percentage for the SCDM model is probably a consequence of the greater influence of small–scale power in this case.

5.4.3. The Growth of Cluster Peculiar Velocities

If cluster peculiar velocities grew according to linear theory the scaled initial velocities discussed in the last section and plotted in Fig. 5.3 would correspond to the actual velocities of the clusters at $z = 0$. In Fig. 5.4 scatter diagrams are shown in which these two velocities are plotted against each other. It is evident that in fact the agreement is quite poor and that there is a systematic trend for the true cluster velocity to be larger than the extrapolated linear value. This
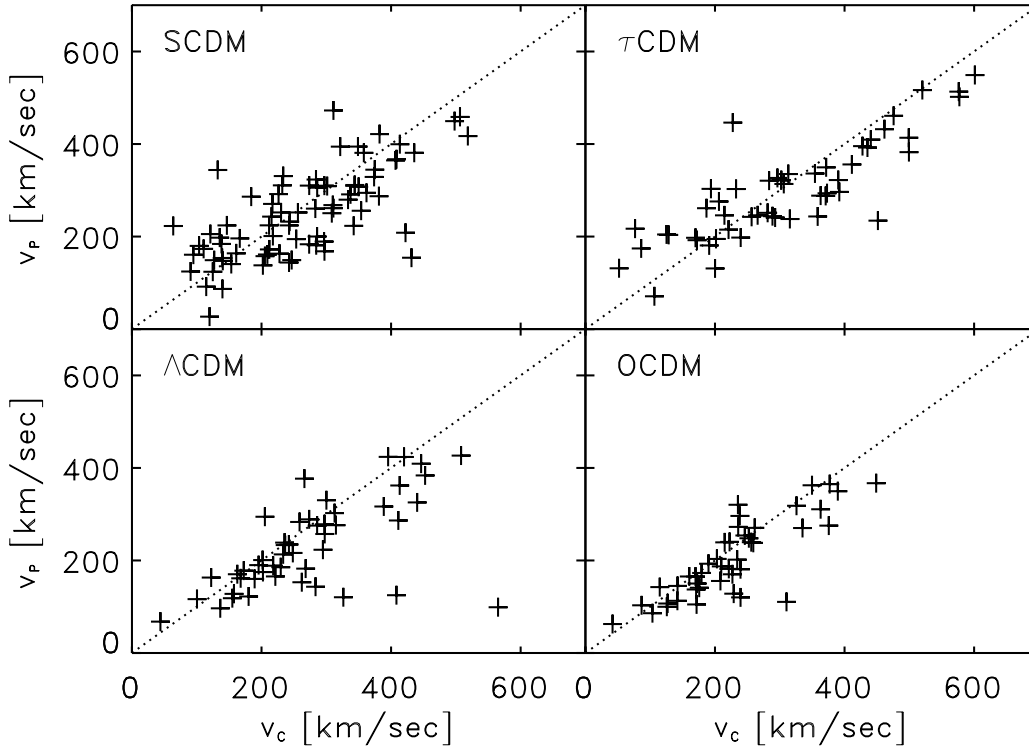
Figure 5.3.: The initial peculiar velocities of clusters in each of our four cosmogonies are compared to the linear peculiar velocities of their associated peaks. The linear peculiar velocity field was smoothed with a Top–Hat in the same way as the density field in order to obtain the peak peculiar velocities.

is reflected in the substantial difference between the *rms* values of these two quantities listed in Table 5.2. It is presumably a consequence of nonlinear gravitational forces accelerating the clusters.

Some confirmation of this is provided by Fig. 5.5 where the peculiar velocity in units of its initial value are plotted for five clusters from each of our cosmologies. At early times the peculiar velocities all grow as expected from linear theory (indicated in the figures by a dotted line) but at later times the behaviour is more erratic and most clusters finish with larger velocities than predicted.

Further evidence that late–time nonlinear effects are responsible for this discrepancy comes from Fig. 5.4. In this plot all clusters that have a neighbour within $10\,h^{-1}$Mpc are indicated with a diamond while more isolated clusters are indicated by a cross. It is evident that deviations from linear theory are substantially larger for the "supercluster" objects than for the rest. These objects also have systematically larger peculiar velocities at $z = 0$. Their *rms* peculiar velocity is around 20 to 30% larger than that of the sample as a whole.

For the τCDM model, a second realization of the power spectrum was run. A cluster sample was extracted in the same fashion as described above. The *rms* peculiar velocity of the clusters at $z = 0$ is $\sigma_{z=0} = 511\,$km/sec. The extrapolated *rms* linear peculiar velocity is $\sigma_{z=0} = 394\,$km/sec. These numbers are very close to the values obtained for the first real-
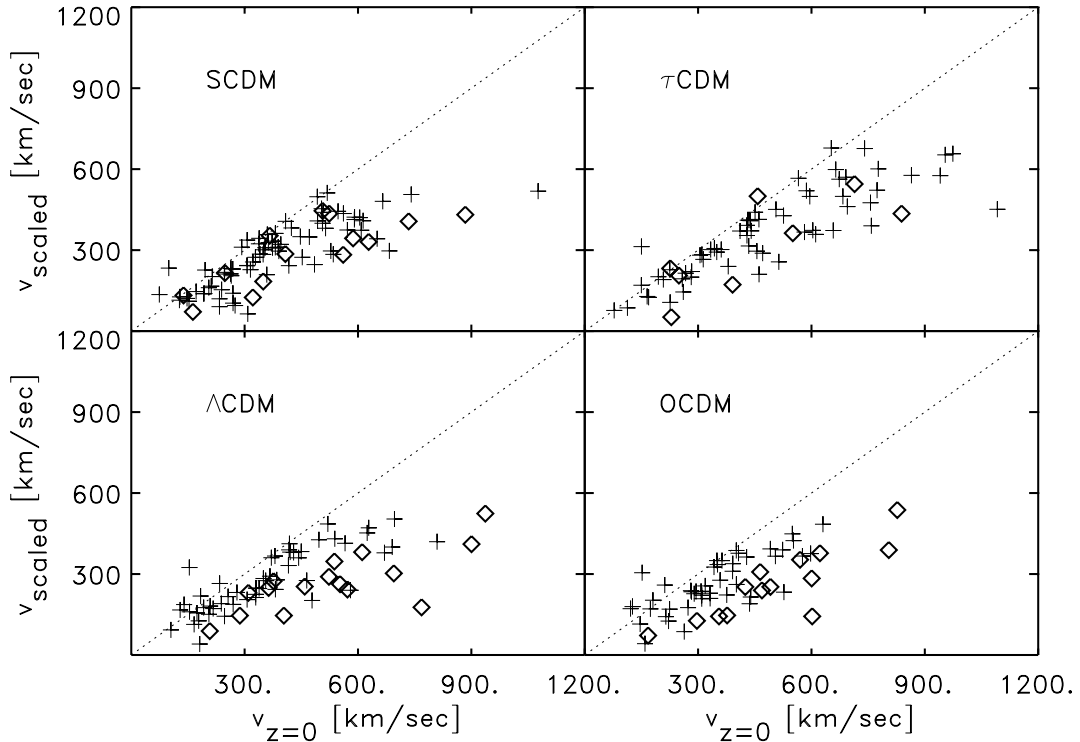
Figure 5.4.: The initial peculiar velocities of clusters in each of our four cosmogonies, scaled up to $z = 0$ using linear theory, are compared to their actual peculiar velocities at $z = 0$. Diamonds denote clusters which have a neighbour within $10\,h^{-1}$Mpc while crosses denote more isolated clusters.

ization. Although two simulations are not a good statistical sample, it can be concluded that there is no realization dependence of the mis–match between the extrapolated linear and the actual peculiar velocities of galaxy clusters.

It might be thought that this anomalous acceleration of clusters at late times was a consequence of the relatively small radius, $1.5\,h^{-1}$ Mpc, used to define the clusters. Material could perhaps be ejected asymmetrically from this region during the merging events by which clusters form. In order to check this, clusters have been redefined to be all the material contained within a radius of 3 or $5\,h^{-1}$ Mpc. Then, the analysis for the same set of objects has been repeated as before. In most cases this turned out to make very little difference to either the initial or the final velocities measured, and it did nothing to reduce the discrepancy between them. The relevant nonlinear effects are acting on significantly larger scales. This procedure was repeated going as far out as $25\,h^{-1}$ Mpc from the cluster center. At a radius of $10\,h^{-1}$ Mpc, the difference between the *rms* peculiar velocity and the extrapolated *rms* linear peculiar velocity is only 10%. By a radius of $20\,h^{-1}$ Mpc, the numbers have finally converged.

The discrepancy between the *rms* peculiar velocity of clusters and their extrapolated *rms* linear peculiar velocity is independent of any smoothing of the density field. With the choice of smoothing filter, the linear peculiar velocities of our clusters match those of their associated peaks as well as the *rms* value predicted by linear theory when the simulated realization of the
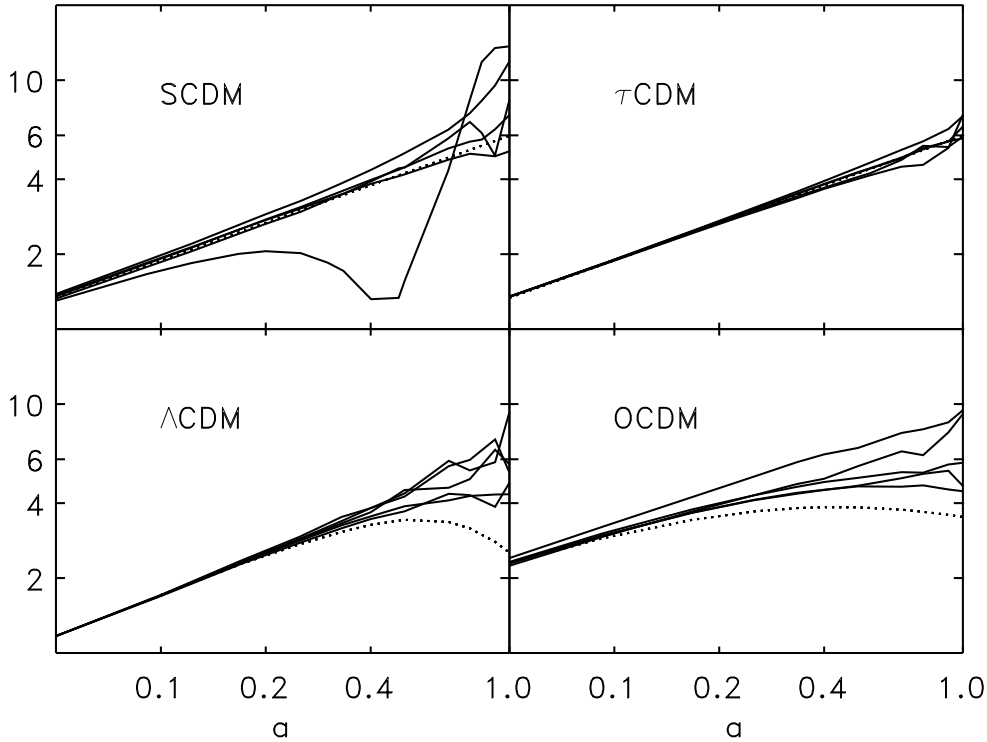
Figure 5.5.: The evolution with expansion factor a of the ratio $|\vec{v}(a)|/|\vec{v}_0|$ for five clusters from each of our four cosmogonies (solid lines) is compared with the evolution predicted by linear theory (dotted line). In some of the cases, merging leads to abrupt changes in this ratio – the most impressive case can be seen for one of the SCDM clusters.

power spectrum and the proper expression for the peculiar velocities (eq. 5.10) is used. Previous work (e.g. Borgani et al. 1997) has tried to match N–body data with linear theory by tuning the filter scale. The results obtained above undermine the physical basis for such a procedure. The goal of the paper by Borgani et al. is different from the one of this Chapter. They try to compare their simulation results with a sample of observed clusters. Tuning the filter scale does not change the *relative* differences between the *rms* peculiar velocities of different cosmogonies. However, it leads to completely misleading results about theory itself. In particular, it destroys the agreement between the different results obtained with linear theory described above.

5.5.   Summary

The peculiar velocities predicted for galaxy clusters by theories in the Cold Dark Matter family have been investigated. A widely used hypothesis identifies rich clusters with high peaks of a smoothed version of the linear density fluctuation field. Their peculiar velocities are then obtained by extrapolating the similarly smoothed linear peculiar velocities at the positions of these peaks. This has been tested in this Chapter using the set of VIRGO simulations. Galaxy

clusters are identified at $z = 0$ and then the particles they consist of are traced back to earlier times. In the initial density field, the barycenters of 70% and 80% of the clusters with masses exceeding $3.5 \times 10^{14} \, h^{-1} \, M_\odot$ lie within $4 \, h^{-1}$ Mpc (comoving) of a peak with $\nu > 1.5$ for the low and high Ω models, respectively. Furthermore, the mean linear peculiar velocity of the material which forms a cluster at $z = 0$ agrees well with the value at that peak.

However, the late–time growth of peculiar velocities is systematically underestimated by linear theory. At the time clusters are identified, i.e. at $z = 0$, the *rms* peculiar velocity is about 40% larger than predicted. Nonlinear effects are particularly important in superclusters; the *rms* values for clusters which are members of superclusters are about 20% to 30% larger than those for isolated clusters.

Acknowledgements
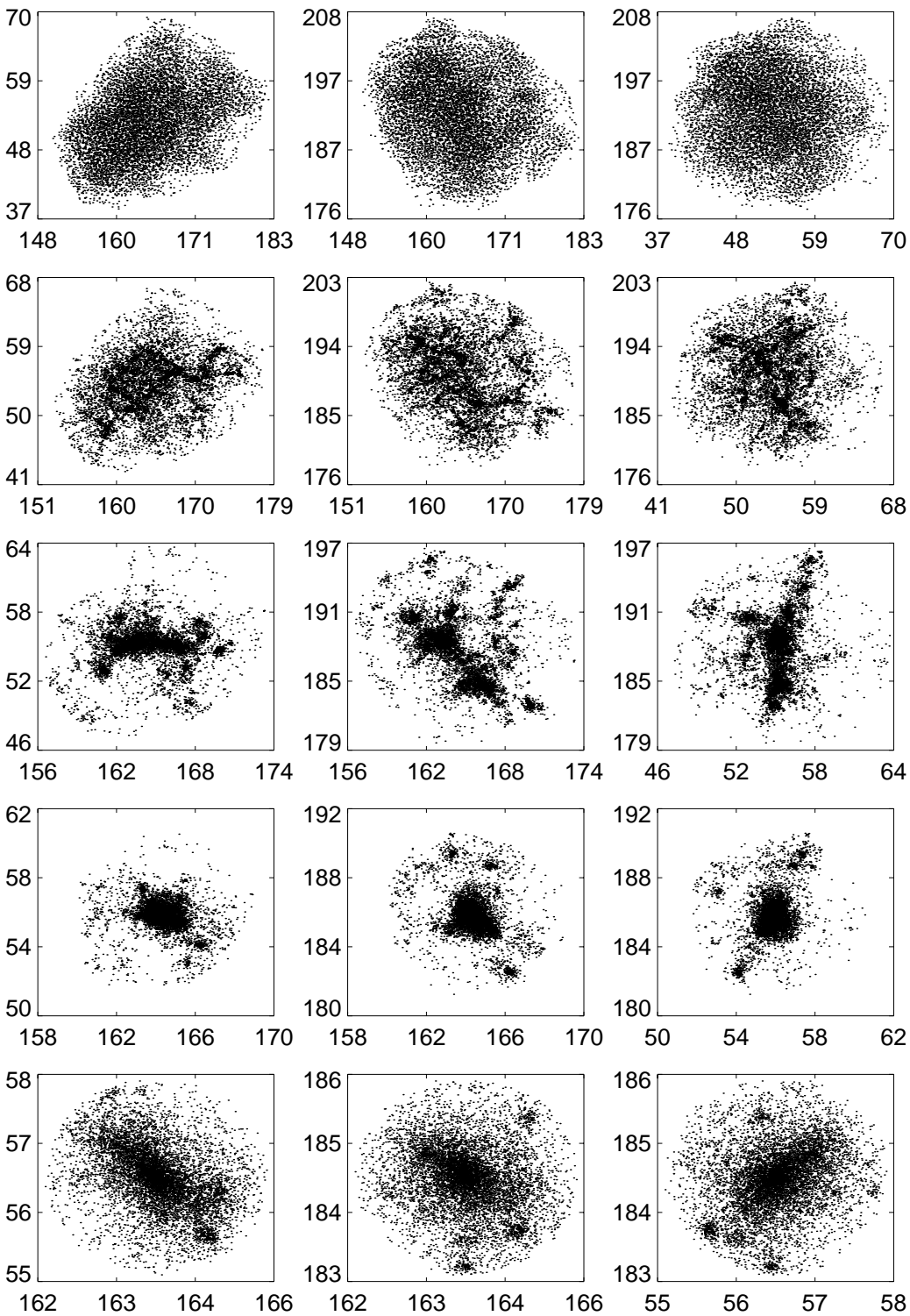
Figure 5.6.: Formation of a cluster in the ΛCDM simulation. The x–y (leftmost panels), x–z (middle panels), and z–y (rightmost panels) projections are shown. The sizes of the regions are in Mpc/h (comoving), the redshifts are 30, 3, 1, 0.3, and 0 (from top to bottom).

Bibliography

[1] Bahcall N.A., Oh S.P., ApJ, 462L, 49B (1996)

[2] Bardeen J.M., Bond J.R., Kaiser N., Szalay A.S., ApJ, 304, 15 (1986)

[3] Bharadwaj S., Sethi S.K., ApJS, 114, 37B (1998)

[4] Bond, J.R., Efstathiou, G., ApJ, 285, L45 (1984)

[5] Borgani S., Da Costa L.N., Freudling W., Giovanelli R., Haynes M.P., Salzer J., Wegner G., ApJ, 482, L121 (1997)

[6] Carroll S.M., Press W.H., Turner E.L., ARAA, 30, 499 (1992)

[7] Couchman H.M.P., Thomas P.A., Pearce F.R., ApJ, 452, 797 (1995)

[8] Croft R.A.C., Efstathiou G., MNRAS, 268, L23 (1994)

[9] Efstathiou G., Davis M., Frenk C.S., White S.D.M., ApJS, 57, 241 (1985)

[10] Eke V.R., Cole S., Frenk C.S., MNRAS, 282, 263 (1996)

[11] Frenk C.S., White S.D.M., Davis M., Efstathiou G., ApJ, 327, 507 (1988)

[12] Hockney R.W., Eastwood J.W., "Computer simulation using particles", McGraw–Hill 1981

[13] Jenkins A., Frenk C.S., Pearce F.R., Thomas P.A., Colberg J.M., White S.D.M., Couchman H.M.P., Peacock J.A., Efstathiou G.P., Nelson A.H. (The Virgo Consortium), ApJ, 499, in press (1998)

[14] Katz N., Quinn T., Gelb J.M., MNRAS, 265, 689 (1993) (KQG)

[15] Lahav O., Lilje P.B., Primack J.R., Rees M.J., MNRAS, 251, 128 (1991)

[16] MacFarland T., Couchman H.M.P., Pearce F.R., Pichlmaier J., submitted to New Astronomy, astro-ph/9805096

[17] Monaco P., Fund. Cosm. Phys., in press (1998)

[18] Pearce F.R., Couchman H.M.P., Jenkins A.R., Thomas P.A., 'Hydra – Resolving a parallel nightmare', in Dynamic Load Balancing on MPP systems

[19] Pearce, F.R., Couchman, H.M.P., "Hydra: A parallel adaptive grid code", submitted to New Astronomy (1997)

[20] Peebles, P.J.E., Principles of Physical Cosmology, Princeton University Press 1993

[21] Strauss, M.A., Willick, J.A., Phys. Rep., 261, 271 (1995)

[22] Sugiyama N., ApJS, 100, 281 (1995)

[23] Thomas P.A., Colberg J.M., Couchman H.M.P., Efstathiou G., Frenk C.S., Jenkins A.R., Nelson A.H., Hutchings R.M., Peacock J.A., Pearce F.R., White S.D.M. (The Virgo Consortium) accepted by MNRAS, astro-ph/9707018

[24] White M., Gelmini G., Silk J., Phys. Rev. D, 51, 2669 (1995)

[25] White S.D.M., Efstathiou G., Frenk C.S., MNRAS, 262, 1023 (1993)
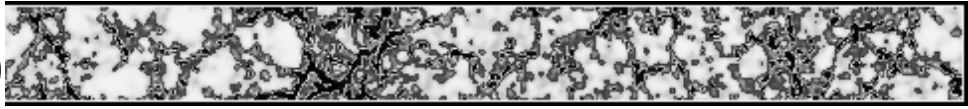
Galaxy Clusters in the Hubble Volume Simulations

*Tout ce monde visible n'est qu'un trait imper-
ceptible dans l'ample sein de la nature. Nulle
idée n'en approche. Nous avons beau enfler nos
conceptions, au delà des espaces imaginables,
nous n'enfantons que des atomes, au prix de la
réalité des choses. C'est une sphère dont le cen-
tre est partout, la circonférence nulle part.*

Blaise Pascal
Pensées, Sect. II 72

6.1. The Hubble Volume Simulations

The expansion of the Universe sets a time scale $(\dot{a}/a)^{-1}$ which corresponds to a length scale called the Hubble radius:

$$r = \frac{c}{H(t)} \,.$$

(6.1)

At present time, and for $\Omega_0 = 1$, this length scale amounts to $r = 3000\,\mathrm{Mpc}/h$. It gives the sale over which physical processes operate coherently and at which general relativistic effects become important (see e.g. Padmanabhan 1993). The volume inside the sphere of radius r is called the Hubble Volume. It amounts to the whole *observable* Universe because a galaxy at the distance of the Hubble radius has recession velocity equal to the speed of light.

The ideal cosmological simulation would enclose a region of the size of the whole observable Universe with as high a mass resolution as possible. The reason for this is clear from the two preceding Chapters. A high mass resolution is desirable in order to resolve Large–Scale Structure properly. A large simulation volume is needed in order to get as many massive

structures as possible. Generally speaking, a large region will enclose more rare objects than a smaller region. In particular, fluctuations on scales of the GIF boxes or even the Virgo boxes can only be investigated if the simulated volume itself is much larger than these scales. Is the Milky Way situated in a region which is under–dense with respect to the whole Universe (see e.g. Zehavi et al. 1998)? How likely is the appearance of such a region? Can Cold Dark Matter models account for the observed pattern of periodicity in the very deep pencil beam surveys (Broadhurst et al. 1991)? What is the mass of the most massive cluster which possibly can be found in the Universe? In particular, does the very nice agreement between the theoretical Press–Schechter mass function and the output of N–body simulations still hold at the very high end of the mass function? Questions like these obviously need a very large simulation volume.

As will be discussed in Chapter 8, the first version of the simulation code which can be run on a CRAY T3E is P^3M. This code is *very* inefficient if there are too many particles in individual high density regions. An obvious way to overcome such a problem is to simulate a large volume with only a moderately high mass resolution. The re–run of the high Ω_0 Virgo models had shown that if the most massive clusters contain only a few thousand particles the simulation can be carried out quite efficiently. In addition, MacFarland had estimated that if 512 processors of the T3E were used and the code was stripped of all parts which were redundant (like e.g. storing the masses of particles if they all have the same mass) then as many as 1024^3 particles could fit into the T3E (compare MacFarland et al. 1998). So the idea of simulating the entire observable Universe was born. The project, named "The Hubble Volume", needed further work on the code which took about half a year of intense work[1]. In December 1997, the first Hubble Volume Simulation, a τCDM model with the same parameters as the GIF simulation but with 10^9 particles and a box size of $2\,Gpc/h$ (and thus a particle mass of about $2 \cdot 10^{12}\,M_\odot/h$), was started. During the first 24 hour run it produced about 140 GByte of data and completely flooded the mass storage system of the RZG. After solving the problems with the data, the run was finished in a little bit more than 70 hours of CPU time on 512 processors – it had generated about 600 GByte of raw data. The second run, a ΛCDM model, again with the same parameters as the corresponding GIF model and with a box size of $3\,Gpc/h$, was started a little later.

Figure A.16 shows a thin slice of thickness $20\,Mpc/h$ through the τCDM Hubble Volume simulation at $z = 0$. On these scales, the first visual impression really is that on large scales the distribution of matter is homogeneous. On smaller scales, most of the features already seen in Chapter 3 show up again. There is a complicated network of filaments surrounding large voids. The network seems to show a very large coherence – the same can be seen for the voids. Some of the regions which seem to be denser or less dense than the average appear to be larger than the size of a region corresponding to, say, the Virgo simulations. Clearly, the investigation of this will be of major importance for future galaxy surveys.

Quite obviously, one of the main points of interest in the Hubble Volume Simulations is the study of galaxy clusters. In the following sections, several points will be addressed. After

---

[1] Apart from Tom MacFarland who did the bulk of the programming, the following people contributed work to the project: Adrian Jenkins (Initial Conditions Generator), Frazer Pearce ("stripping" the code from all redundant parts), August Evrard (an additional subroutine for output of data), Andrzej Kudlicki (reducing the light cone data), and myself (running and maintaining the simulation plus what's described in this Chapter and Chapter 8).

a description of the actual selection of two different catalogs of galaxy clusters (section 6.2), the presence of massive clusters at high redshift and its implications for the cosmogonies will be investigated (section 6.3). In addition, the mass function of the cluster catalogs will be briefly compared with the analytical Press–Schechter theory. The final point of the Chapter will be the clustering of galaxy clusters using the two–point correlation function (section 6.4).

6.2. Extracting Galaxy Clusters

Extracting galaxy clusters from the Hubble Volume Simulations is not an easy task. This is due to two facts. The first one is the sheer amount of data. Each output dump includes the indices, positions, and velocities of the 10^9 particles, which, in total, yields about $27\,\mathrm{GByte}$ of data. The second problem is related to the definition of a galaxy cluster in the simulations itself. As these simulations contain only Dark Matter, a simple count of galaxies is, of course, impossible, because there are no galaxies there. However, identifying the most massive objects in the simulations critically depends on the scheme adopted for this purpose. This will be studied in more detail in the following. A strategy will be developed which finally yields catalogs of galaxy clusters for the simulations at redshifts of $z = 0.78$, $z = 0.44$, and $z = 0$. The scheme chosen here deviates from the one used in Chapter 5. There, galaxy clusters were found by locating high density regions and then placing spheres of size $1.5\,\mathrm{Mpc}/h$ around them. Here, two schemes are taken which are closer to getting virialized objects.

As a first step of the group finding, the particle distribution is assigned to a coarse[2] mesh of size 512^3. This mesh is then used to identify high density regions. If the contents of a mesh cell plus the one of its nearest neighbours exceeds 64 particles these mesh cells are marked as regions from which all particles have to be extracted[3]. For these, only their positions are stored. For the τCDM run, this amounts to about 400m, 500m, and 600m particles for the output redshifts of $z = 0.78$, $z = 0.44$, and $z = 0$, respectively.

On this subset of particles, a standard friends–of–friends (FOF) group finder with a dimensionless linking length of $b = 0.2$ times the mean inter–particle separation is run (this is referred to as $\mathrm{FOF}_{0.2}$ in the following) using ten overlapping slices[4]. Finding objects in such a way, however, is problematic. The $\mathrm{FOF}_{0.2}$ group finder has the tendency to connect smaller objects if there is a bridge of particles between them. This may lead to the situation where a galaxy cluster has two (or more) dense subclumps and is centered on a region where the particle density is low. Not only do such "clusters" not have anything in common with clusters in the real Universe – these are usually found either by an enhancement of galaxies or of X–ray emission so that their centers are high density regions – in addition their masses and spatial extents are misleading. For instance, at $z = 0.78$ the most massive object found with $\mathrm{FOF}_{0.2}$ in the τCDM model has a mass of $1.14 \times 10^{15}\,M_\odot/h$. A visual inspection shows that it consists of at least three connected objects. The size of this object is about $6\,\mathrm{Mpc}/h$. So it looks like

---

[2]Coarse here means that the size of an individual volume cell is *much* larger than a typical galaxy cluster at $z = 0$.

[3]As periodic boundary conditions are used and the loop runs over the whole mesh the choice of only the rightmost neighbouring cells does not miss any high density region but significantly speeds up the process.

[4]Of course, the mean inter–particle separation is computed taking all particles in the whole volume.

a supercluster, that is a group of clusters. Of course, this does not mean that a galaxy cluster in the simulation must never consist of more than one dense knot of particles. But it has to be ensured that it is centered on a high density region and it must not consist of two objects which are connected by a thin bridge of particles.

In order to refine the group finding the FOF group finder is run again with a dimensionless linking length of $b = 0.05$ (this is referred to as $FOF_{0.05}$ in the following) times the mean inter–particle separation. This selects objects which are part of the $FOF_{0.2}$ clusters. The way the particles are extracted ensure that no objects are missed. Due to the algorithm of the FOF group finder, all objects found with a small linking length are always a subset of objects found with a larger linking length. The $FOF_{0.05}$ group finding yields only the densest particle knots, that is candidates for the centers of clusters. As the final step, particles out to a virial radius from each such proto–center are collected. The way this is done is essentially the same as for the Spherical Overdensity (SO) group finder (Lacey & Cole 1994). The idea is to find objects whose mean overdensity is 178 (97) for $\Omega_0 = 1$ ($\Omega_0 = 0.3, \Lambda_0 = 0.7$). The value of 178 (97) results from the expected overdensity of a top–hat perturbation at virialization (e.g. White 1996, Eke et al. 1996). Starting from the barycenter of the proto–cluster, the nearest particle which is not yet a member of the cluster is added and the mean overdensity is computed. If this is larger than 178 (97) the process is repeated. The way objects are found does not necessarily construct spherical objects. The final step then is to check whether there are pairs of clusters which are so close together that they actually belong to the same object – this may indeed be the case for *some* clusters. The criterion of whether two clusters are only subclusters of a bigger one is arbitrary. The criterion adopted here is the following. For each cluster, its mass and its virial radius are known. Two clusters are now taken as members of the same object if the center of one of them lies within the virial radius of the center of the other one. The smaller one of the pair is then deleted from the list because a large fraction of its mass is already contained in the mass of the other cluster. This process is very similar to how galaxy clusters are found in surveys of the real Universe. The main difference, of course, is that here it can be done using full three–dimensional information which is not the case for observations.

Two catalogs of clusters are thus obtained for the models. They will be referred to as $FOF_{0.2}$ clusters and virial clusters for the objects found with the $FOF_{0.2}$ group finder and with the $FOF_{0.05}$ group finder plus subsequent identification of virial masses, respectively. For the ΛCDM model, only the virial clusters are obtained. In the following section, both these catalogs will be compared to theoretical estimate of the mass function. This will lead to a qualitative insight into the contamination of the $FOF_{0.2}$ due to flukes of the group finder itself.

6.3. The Mass Function

6.3.1. Massive Objects at High Redshifts

Introduction

Clusters of galaxies are the largest virialized objects in the Universe. For decades now they have been studied observationally as well as theoretically in order to determine the cosmological parameters which describe the Universe. The density parameter, Ω_0, affects several proper-

ties of galaxy clusters. For instance, if $\Omega_0 = 1$ clusters should form at considerably lower redshifts than for $\Omega_0 < 1$ (Richstone et al. 1992, Bartelmann et al. 1993), have more substructure, and should be less centrally concentrated. Here, the first of these points will be studied. As the formation time of clusters is strongly dependent on Ω_0, the evolution of the cluster abundance should be a sensitive probe of it. However, the situation is still very unclear as can be seen from the plethora of papers which appeared recently about this very point. From the evolution of the cluster abundance, there is currently no consensus whether a high or a low Ω can be excluded (Henry 1997, Carlberg et al. 1997, Bahcall et al. 1997, Blanchard & Bartlett 1997, Gross et al. 1997, Sadat et al. 1998, Eke et al. 1998 (ECFH hereafter)). As was stated in ECFH the wide range in values for the density parameter "is presumably a suggestion that unaccounted–for systematic errors are lurking beneath the surface in at least one of these analyses". The mass function itself will be investigated in the next subsection. In this subsection, the presence of high redshift objects in the simulations is investigated. In particular, lensing mass estimates for three observed galaxy clusters are used. Before turning to the simulations, these clusters are briefly described in the following.

The Most Massive Clusters at high z in the Universe

Over the last couple of years, the number of observed galaxy clusters at high redshift has been increasing steadily. Massive clusters at high redshift pose a major threat to an $\Omega_0 = 1$ universe. For three clusters, MS 1054–03, MS 1137+66, and RXJ 1716+67, redshifts ($z \approx 0.8$), mass estimates, and X–ray temperatures have been obtained.

Luppino & Kaiser (1997) detected a weak lensing signal of the cluster MS 1054–03, which is at $z = 0.83$. Assuming that the population of lensed Faint Blue Background Galaxies (FBG's) is at $z = 3$, they derive a mass within 0.5 Mpc/h of $(5.9 \pm 1.2) \cdot 10^{14} \, M_\odot/h$. This is a *lower* limit because if the redshift of the FBG's is lowered, the mass of the cluster is increased. Donahue et al. (1998) measured the X–ray temperature of this cluster and found it to be $12.3^{+3.1}_{-2.2}$ keV. They note that this temperature is consistent with the mass Luppino & Kaiser give and with an estimate of the velocity dispersion of the cluster ((1360 ± 450) km/sec at 90% confidence level; using spectra of 12 cluster members). However, MS 1054–03 does not look like a relaxed system. Its light distribution and its mass distribution are elongated. *ROSAT* imaging shows "two or three clumps and an extended component, clearly indicating that this cluster is not regular." King model fits are rejected by the data. Donahue et al. end the discussion of the spatial structure by noting "We found that the cluster is at least bimodal at greater than 99.9% confidence level." This indicates that the properties of this cluster have to be taken with a grain of salt.

Clowe et al. (1998) detected a weak lensing signal for the other two clusters, MS 1137+66 at $z = 0.78$ and RXJ 1716+67 at $z = 0.81$. They found respective masses within a radius of 0.5 Mpc/h of $(2.45 \pm 0.8) \cdot 10^{14} \, M_\odot/h$ and $(2.6 \pm 0.9) \cdot 10^{14} \, M_\odot/h$ assuming the background galaxies lie in a sheet at $z = 2$. Whereas MS 1137+66 has a compact mass and light distribution, RXJ 1716+67 looks like an ongoing merger.

These observations will be taken as a guideline in the following. The masses of the most massive simulated objects within a radius of 0.5 Mpc/h will be measured. The fact that lensing was able to provide the masses of the three observed clusters allows a test of the CDM models.

The Most Massive Clusters at high z in the Simulations

For this study, only the dumps at $z = 0.78$ are taken. The algorithm used in order to find the most massive objects is changed as follows. Starting from the $FOF_{0.05}$ objects, the particle counts within spheres of size $0.5\,\mathrm{Mpc}/h$ are obtained. This yields objects which are directly comparable to the clusters described above without *any* assumption about virialization or the like.
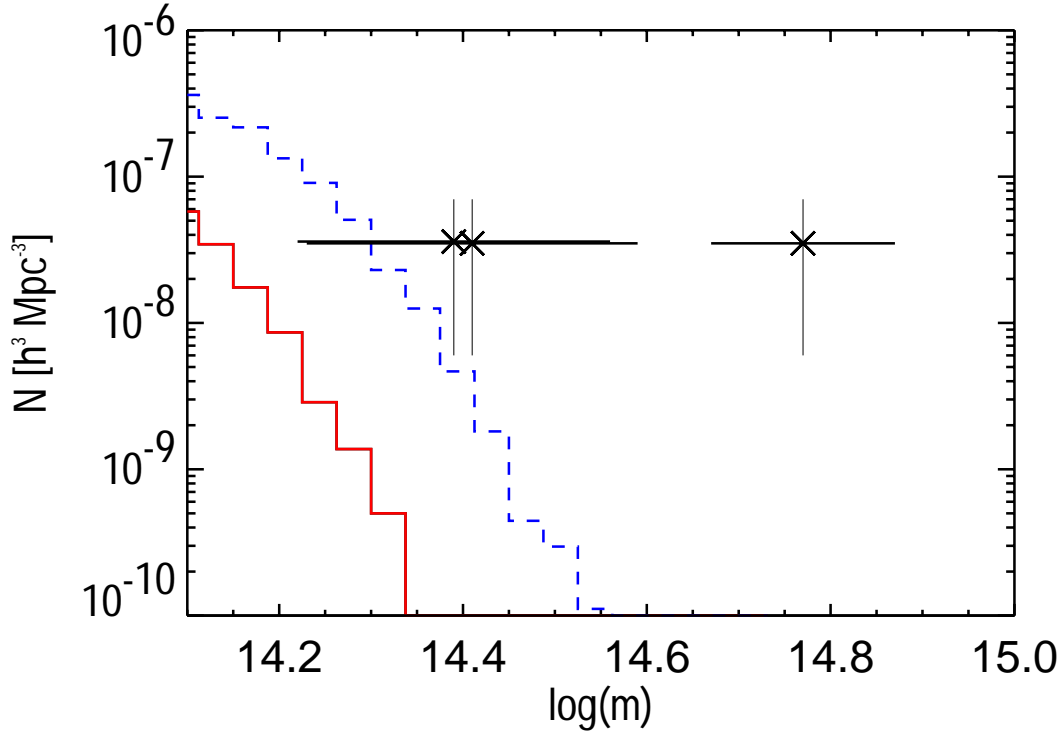
Figure 6.1.: The differential number density distribution of the masses within $0.5\,\mathrm{Mpc}/h$ for the most massive objects at $z = 0.78$ in the τCDM (solid histogram) and the ΛCDM (dashed histogram) simulation. The three crosses with the errorbars show the corresponding masses of the three clusters mentioned in the text.

Figure 6.1 shows the differential number density distribution of the masses within $0.5\,\mathrm{Mpc}/h$ for the most massive objects in the τCDM (solid line) and the ΛCDM (dashed line) simulations. Also given, as crosses with errorbars, are the three clusters MS 1054–03, MS 1137+66, and RXJ 1716+67. The number densities are taken from Bahcall & Fan (1998; Donahue et al. 1998 give similar numbers) and should be taken as indicative. Apparently, as indicated already in Chapter 2 and pictorially shown in Chapter 3, there are substantially more massive objects in the low density model than in the high density one at this redshift. The two clusters MS 1137+66 and RXJ 1716+67 lie at the extreme high mass end of the τCDM distribution and within the distribution of the ΛCDM model. Their number densities are too high for

τCDM. The cluster MS 1054–03 lies way outside the mass ranges covered by either model.

Conclusions about this can still not be made without discussing possible problems of the modeling and the clusters themselves. The normalization, $\sigma_8 = 0.6$, chosen for the τCDM simulation is at the high end of what is generally considered to be a good normalization for an $\Omega_0 = 1$ universe (see Chapter 2). Adopting a lower normalization amounts to a scaling in time. E.g., if the normalization is adopted which was taken in the simulations discussed in Jenkins et al. (1998), then the redshift of the output time considered here is lowered to $z = 0.5$. As haloes build up by accretion and merging, at a higher redshift the masses of the most massive clusters would be smaller than what is found for $\sigma_8 = 0.6$. One would then get a distribution of masses which ends at a lower mass than what is found, making the distribution more incompatible with the three high mass clusters. For the ΛCDM model, the case is not that clear. A higher value of σ_8 may still be possible because of the scatter in the $\Omega_0 - \sigma_8$ relation. This would then shift the distribution to higher masses.

In addition, high density regions from a very large volume have been picked – it is a complete sample. The galaxy clusters mentioned above are no complete sample. Any further cluster with such a high mass as MS 1054–03 will aggravate the discrepancy between the masses predicted by the τCDM simulation and the observations. However, in principle projection effects may lead to the observation of high mass clusters if two clusters happen to lie behind each other or if a filament is observed in the direction of its longitudinal extent. Oke et al. (1998) note that about 30% of all high redshift clusters are misidentified that way. However, for the most massive cluster, MS 1054–03, the lensing mass agrees with mass estimates from the X–ray temperature and from the velocity dispersion of 12 cluster members. Obviously, at this redshift the latter cannot be taken very seriously. If it is assumed that the cluster is in fact two clusters behind each other, the high lensing mass can be accounted for, but the X–ray temperature still poses a problem. An ongoing merging could account for this – when two clusters merge strong shocks in the colliding gas are formed. As noted above, given the appearance of this cluster it should not be treated as a relaxed system.

Conclusions

From the above, it is a safe statement to say that $\Omega_0 = 1$ ceases to be a viable model for the formation of structure in the Universe because the number densities of massive clusters at high redshifts are much too small in such models. At this stage, it would be premature to judge the ΛCDM model. The number densities of massive clusters are high enough. More mass measurements of clusters at $z \approx 0.8$ are needed in order to see whether MS 1054–03 is a typical object or just happens to be a merging cluster viewed from an unfortunate angle. If, however, more clusters like MS 1054–03 are found a big problem arises. With the normalization used here ΛCDM cannot account for objects with such high masses at $z = 0.8$. In addition, at this redshift an open model produces only slightly more clusters and thus would have the same problems. Very massive virialized clusters at redshifts of $z \approx 0.8$ may well topple the CDM models discussed here – if these clusters really exist.

6.3.2. The Press–Schechter Mass Function

The derivation of the mass function can be found in many textbooks. Here, the one from White (1996) is followed. The most convenient way to describe the linear density field is to consider its Fourier decomposition

$$\delta(\mathbf{x}) = \sum_k \delta_\mathbf{k} \exp(i\mathbf{k}\mathbf{x}) .$$ (6.2)

For a Gaussian random field, the different Fourier amplitudes $\delta_\mathbf{k}$ are independent random variables with random phases. The mean square density fluctuation in spheres of radius R at time t is then

$$\Delta^2(R, t) = \langle \delta_s^2 \rangle_\mathbf{x} = \int \mathrm{d}^3 k |\delta_k|^2 |\tilde{W}(\mathbf{k}R)|^2 ,$$ (6.3)

where $\tilde{W}(\mathbf{k}R)$ is the Fourier transform of the window function used. In Linear Theory, Δ scales like the growing mode of the linear fluctuations $\Delta \propto D(t) \propto a(t)$, and it can be separated as $\Delta(R, t) = a(t)\Delta_0(R)$.

The fraction of points at which a Gaussian random field exceeds some given value is known. Thus at a time t, the fraction of points which are surrounded by a sphere of radius R within which the mean density is larger than δ_c is given by

$$f(R, t) = \int_{\delta_c}^{\infty} \mathrm{d}\delta \frac{1}{\sqrt{2\pi}D(t)\Delta_0} \exp\left[-\frac{\delta^2}{2D(t)^2\Delta_0^2}\right] .$$ (6.4)

Press & Schechter (1974) now assumed that this expression gives the fraction of particles which are part of an object with mass exceeding $M = 4\pi \bar{\rho} (a(t)R)^3 /3$. For δ_c they took the extrapolated *linear* overdensity at collapse of a spherical perturbation, $\delta_c = 3/20(12\pi)^{2/3} \approx 1.69$. However, Press & Schechter had to multiply the mass fraction by a factor of 2 because as M approaches zero F approaches $1/2$, that is only half of the mass in the Universe is predicted to be in any object. The mass function then is

$$n(M, t)\,\mathrm{d}M = -\sqrt{\frac{2}{\pi}} \frac{\bar{\rho}}{M} \frac{\delta_c}{D(t)\Delta_0^2} \frac{\mathrm{d}\Delta_0}{\mathrm{d}M} \exp\left[-\frac{\delta_c^2}{2D(t)^2\Delta_0^2}\right] \mathrm{d}M ,$$ (6.5)

where $\bar{\rho}$ is the present mean mass density of the Universe. Bond et al. (1991) later found a derivation which naturally led to the missing factor of 2 for sharp windows in k space. The cumulative mass fraction in objects above some mass M is given by

$$P(> M, t) = \mathrm{erfc}\left[\frac{\delta_c}{\sqrt{2}D(t)\Delta_0}\right] .$$ (6.6)

Figures 6.2 and 6.3 show a comparison of the τCDM FOF$_{0.2}$ and virial clusters with the analytical cumulative mass function, respectively. The solid, dotted, and dashed lines were obtained using eq. (6.6) at $z = 0$, $z = 0.44$, and $z = 0.78$, respectively. The virial clusters in general are better fit by the analytical prediction. Both cluster samples lie above it. At $z = 0.44$ and $z = 0.78$, the discrepancy is worse. The deviations of the FOF$_{0.2}$ clusters are quite large. As already discussed above, the FOF$_{0.2}$ tends to link groups artificially. Obviously, this shows up here. Jenkins independently applied the same procedure with a different code to the simulations. The groups he found agree with the ones given here (Jenkins, private communication).
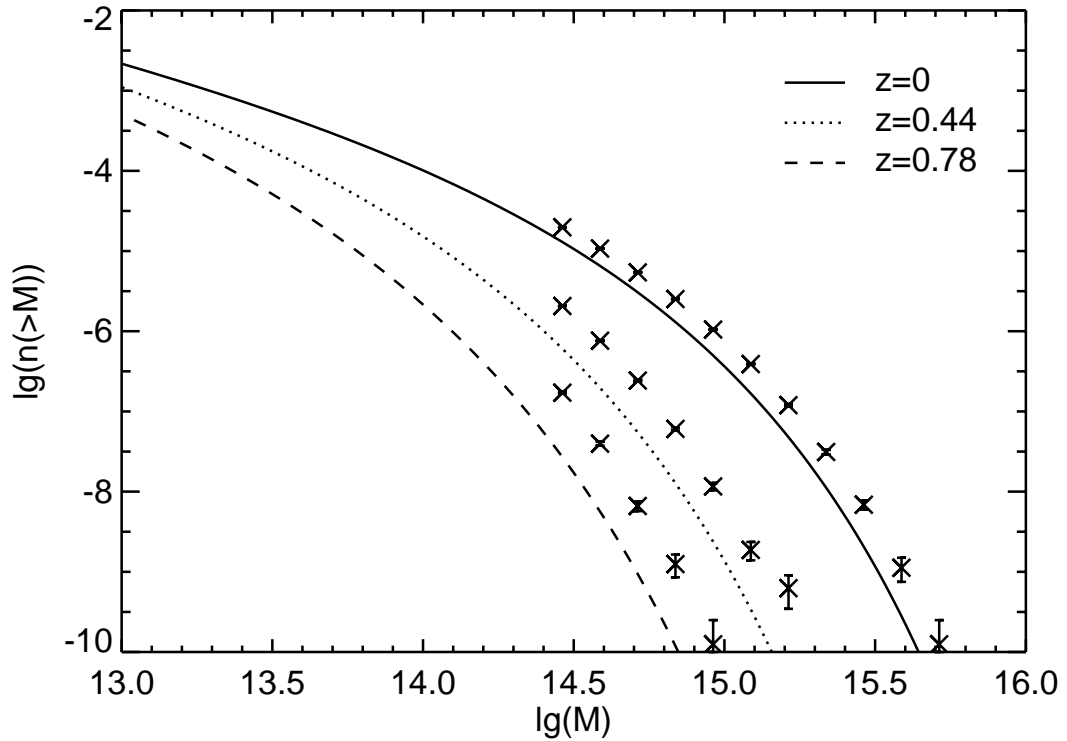
Figure 6.2.: The cumulative mass function of the τCDM FOF$_{0.2}$ catalog (crosses with error-bars) against the prediction of the Press–Schechter theory for the three redshifts (solid, dotted, and dashed lines). The masses are given in units of $M_\odot/h$.

6.4. The Cluster Correlation Function

As discussed in the preceding Chapter, clusters form from the highest peaks in the initial density field of the early Universe. If one assumes that the small fluctuations from which large–scale structure grows were a Gaussian random field then peaks/clusters themselves are clustered (Kaiser 1984). A tool to describe the strength of the clustering is the two–point correlation function which will be discussed in the next section.

6.4.1. Introduction

The two–point correlation function of galaxy clusters has been controversial for decades now. Since the early work of Hauser & Peebles (1973) it has been known that rich galaxy clusters are more strongly clustered than galaxies. However, the amplitude of the two–point correlation function and its dependence on cluster richness have been the subject of controversy.

The correlation function depends on cluster richness. Richer clusters are rarer, hence their mean space density, n_c, is smaller. Usually this is expressed using the mean intercluster sepa-
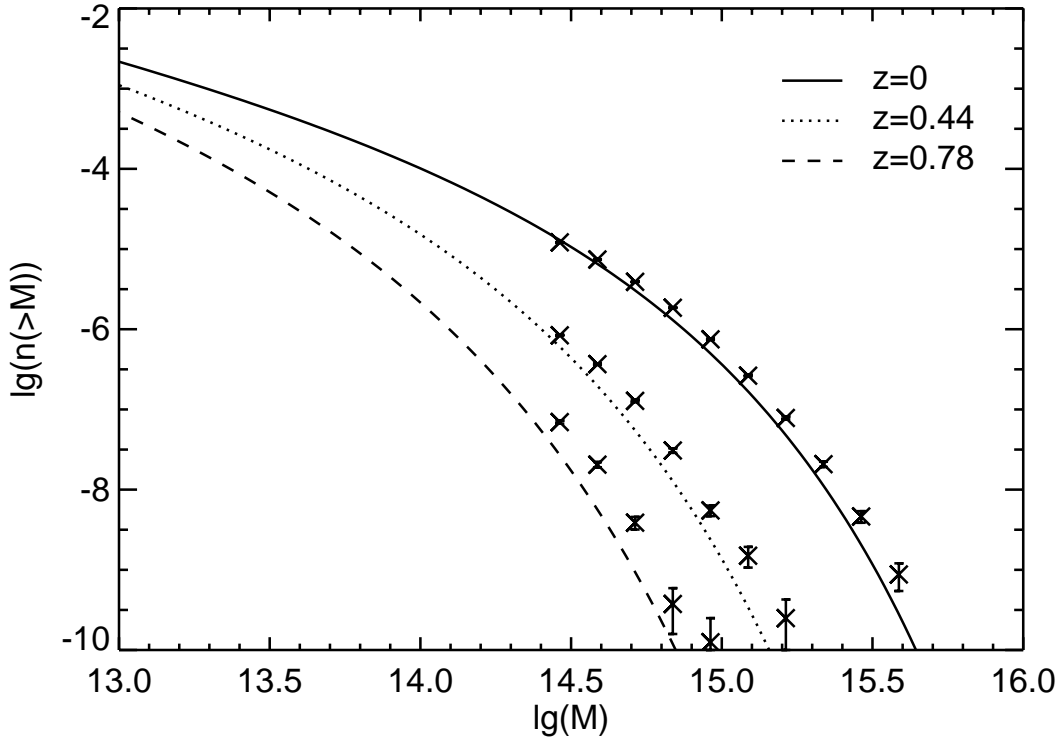
Figure 6.3.: The cumulative mass function of the τCDM virial mass catalog (crosses with errorbars) against the prediction of the Press–Schechter theory for the three redshifts (solid, dotted, and dashed lines). The masses are given in units of $M_\odot/h$.

ration $d_c = n_c^{-1/3}$. Bahcall (e.g. in Bahcall & Cen 1992, Bahcall & West 1992) has argued that the correlation length, r_0, defined via $\xi(r_0) = 1$, scales linearly with d_c,

$$r_0 = 0.4\,d_c\,. \tag{6.7}$$

This *Ansatz* is based on self–similar scaling. Early measurements of $\xi(r)$ for the Abell cluster sample (Abell 1958, Abell et al. 1989) seemed to confirm this scaling (e.g. Bahcall & Soneira 1983, Peacock & West 1992). However, it was already pointed out by several works (e.g. Peacock & West 1992, Efstathiou et al. 1992) that incompleteness of the Abell cluster catalog artificially enhances the clustering amplitude by producing significant line–of–sight correlations. A means to investigate this is to use $\xi(\sigma, \pi)$, where σ and π are the pair separations perpendicular and parallel to the line–of–sight, respectively. Peacock & West found a very strong anisotropy signal for clusters of richness class R=0 in the Abell catalog whereas for R$\geq$1 the effect was absent. Efstathiou et al. came to the same conclusion for the redshift survey of 351 Abell clusters from Postman et al. (1992) (see Efstathiou 1996 for a detailed review of these issues).

Quite surprisingly, both camps have used N–body simulations of CDM–type models to support their views. Bahcall & Cen (1992) found that their simulation agreed with their scaling

proposed for clusters in the real Universe. Using ensembles of simulations, Croft & Efstathiou (1994) found that the amplitude of $\xi(r)$ depended only weakly on cluster richness. They suggested that Bahcall & Cen's conclusions were a consequence of having run a single simulation with a low resolution N–body code. In addition, Croft & Efstathiou noted that the cluster correlation function is *insensitive* to Ω and weakly dependent on the normalization of the power spectrum, σ_8, but depends strongly on its shape, parameterized via Γ. Recently, Eke et al. (1996a) studied the systematics of the cluster correlation function in simulations, in particular the influence of the group finding algorithm. They ran several realizations of the same cosmology and compared several cluster finding algorithms with each other. Their overall result supported the findings of Croft & Efstathiou (1992). However, the simulation work up to the present date suffered significantly from the restrictions in the volumes so that so far no conclusive answer could be reached about the relation between the mean intercluster separation and the correlation length in CDM–type models.

Croft et al. (1997) analyzed the cluster catalog selected from the APM Galaxy Survey. The APM clusters are comparable in richness and space density to $R \geq 0$ Abell clusters. They found a weak richness dependence of $\xi(r)$ which is inconsistent with the linear scaling proposed by Bahcall.

Using a Press–Schechter type *ansatz*, Mo & White (1996) derived expressions for the clustering of Dark Matter haloes. In particular, they showed that the two–point correlation function of haloes of Lagrangian radius R is related to that of the Dark Matter, ξ_{DM}, by

$$\xi(r) = b^2(R)\,\xi_{\mathrm{DM}}(r)\,, \tag{6.8}$$

where $\xi_{\mathrm{DM}}(r)$ is the two–point correlation function of the mass, and $b(R)$ is a bias factor which will be introduced in more detail below. Mo et al. (1996) tested this *ansatz* on a set of N–body simulations and found that the analytical result agreed with their N–body output.

In the following two sections, the two–point correlation function and the Mo & White model will be introduced. Then, they will be applied to the Hubble Volume cluster catalogs.

6.4.2. The Two–point Correlation Function

Given a set of points, the two–point correlation function is defined as follows. The probability $\mathrm{d}P$ that a point is found centered within an arbitrarily placed volume element $\mathrm{d}V$ is proportional to the size of the element

$$\mathrm{d}P = n\,\mathrm{d}V\,, \tag{6.9}$$

where n is the number density of the points. The joint probability of finding points centered within two volume elements $\mathrm{d}V_1$ and $\mathrm{d}V_2$ separated by a distance r is proportional to the sizes of the elements

$$\mathrm{d}P = n^2[1 + \xi(r/r_0)]\mathrm{d}V_1\,\mathrm{d}V_2\,. \tag{6.10}$$

Here, r_0 denotes a characteristic clustering length usually defined via $\xi(r = r_0) = 1$. In a random Poisson process, $\xi(r/r_0) = 0$. Thus, the two–point correlation function describes how much the set of points differs from a pure random Poisson process.

The definition (6.10) is equivalent to the following definition. The two–point correlation function is the conditional probability of finding a point in the element dV at a distance r from another point,

$$dP = n[1 + \xi(r/r_0)]dV . \qquad (6.11)$$

That is, it gives the excess probability of finding a pair of points separated by a distance r compared with a random Poisson process. The code used here to compute the two–point correlation function counts the numbers of such pairs as a function of separation and from that computes $\xi(r/r_0)$.

6.4.3. The Mo & White Model

Starting from a Press–Schechter type *ansatz*, Mo & White (1996) develop an analytical theory to describe the spatial clustering of haloes. In particular, they find that the two–point correlation function of Dark Matter haloes of Lagrangian radius R is related to that of the mass, ξ_{DM}, by

$$\xi(r) = b^2(R)\,\xi_{\mathrm{DM}}(r)\,, \qquad (6.12)$$

where

$$b(R) = 1 + \frac{\delta_{\mathrm{c}}}{\sigma^2(R)} - \frac{1}{\delta_{\mathrm{c}}}\,. \qquad (6.13)$$

Here, $\delta_{\mathrm{c}} = 1.69$ as introduced above and $\sigma(R)$ is the *rms* mass fluctuation on the scale of the halo (using a Top–Hat filter; compare the preceding Chapter). Note that a similar relationship is derived in Bardeen et al. (1986; BBKS hereafter) for peaks

$$\xi_{\mathrm{pp}}(r) = \left(\frac{\langle\bar{\nu}\rangle}{\sigma(R_{\mathrm{s}})}\right)^2 \xi_{\mathrm{DM}}(r)\,, \qquad (6.14)$$

where $\bar{\nu}$ is the mean peak height and R_{s} here is the size of the Gaussian filter used to smooth the density field. This was used by Croft & Efstathiou (1994) to derive the scaling of r_0 with d_{c}. As already seen in the preceding Chapter there is a relationship between the peak height and the mass of a cluster, albeit with a big scatter. In addition, it is not clear whether a Gaussian or a Top Hat filter should be taken. Using two different schemes to fix ν_{s}, the threshold height of the peaks, and its corresponding smoothing radius R_{s}, Croft & Efstathiou find that the derived scaling lies above the result of their N–body output. However, they seem to be too pessimistic with regard to the power of eq. (6.14). For instance, they did not try a different filter. They still state, though that qualitatively, the observed trend of the amplitude with richness is reproduced by the BBKS model.

Mo et al. (1996) test the analytical prediction on a set of N–body simulations and find very good agreement. It has to be noted that their way of constructing cluster samples is different from the procedure used by all other authors mentioned here (including this work). Mo et al. use ranges in halo (cluster) masses rather than constructing cluster samples from a given number density. They compute the bias factor (eq. 6.13) by weighting over the range of halo masses in each sample using the theoretical Press–Schechter mass function (Mo, private communication).

6.5. Results from the Hubble Volume
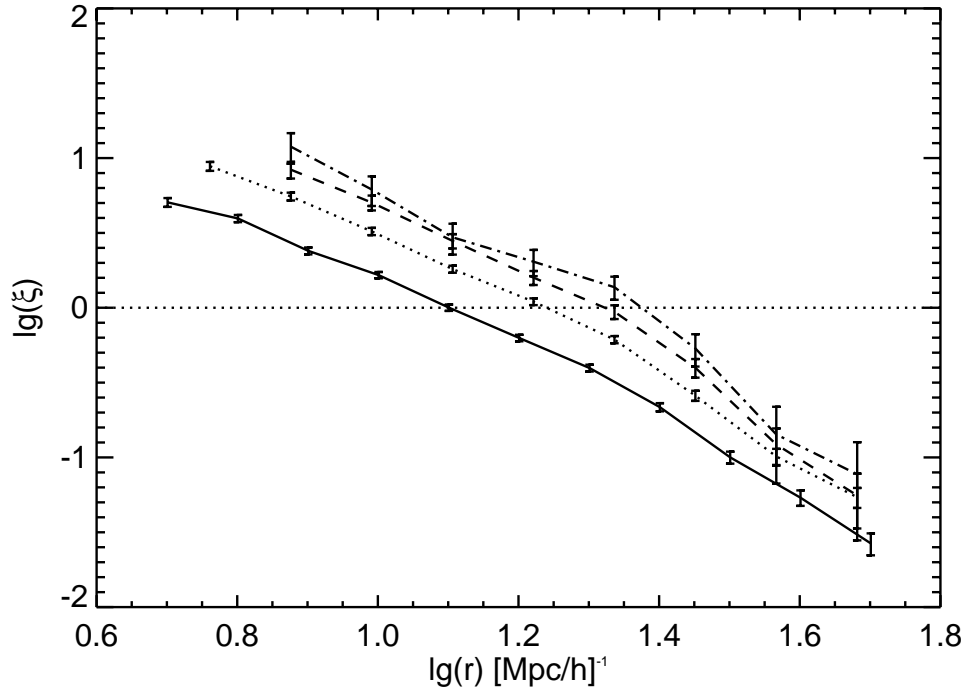
Figure 6.4.: The two–point correlation functions of the τCDM model for the $d_c = 40 \, \text{Mpc}/h$ (solid), $d_c = 70 \, \text{Mpc}/h$ (dotted), $d_c = 100 \, \text{Mpc}/h$ (dashed), and $d_c = 130 \, \text{Mpc}/h$ (dot dashed) samples. The plotted 1σ errorbars are derived from the number of pairs in each bin.

Figure 6.4 shows the cluster correlation functions for the $d_c = 40 \, \text{Mpc}/h$, $d_c = 70 \, \text{Mpc}/h$, $d_c = 100 \, \text{Mpc}/h$, and $d_c = 130 \, \text{Mpc}/h$ sample from the τCDM simulation. 1σ errors have been computed from the numbers of pairs. As can be seen, the amplitude of the clustering increases with the sparseness of the sample. Figure 6.5 gives the correlation functions for the $d_c = 50 \, \text{Mpc}/h$ samples from the two simulations. Superimposed are the linear and nonlinear mass correlation functions scaled with the appropriate biasing factor (for details of the mass correlation function c.f. Jenkins et al. 1998). Note that the ΛCDM case is offset by one order of magnitude for clarity. For the τCDM model, the Mo & White prediction fits the results from the simulation rather well. The amplitude of the ΛCDM case, though, is slightly over-predicted. The *shapes* of the correlation functions, however, do agree well. This means that while the amplitude of the correlation function increases for sparser samples the slope at the zero crossing does *not* remain constant but increases, too. Quite obviously, a fixed slope would lead to misleading results for the sparsest sample.

In order to compute the correlation length, in the vicinity of $\xi(r) = 1$, the correlation func-
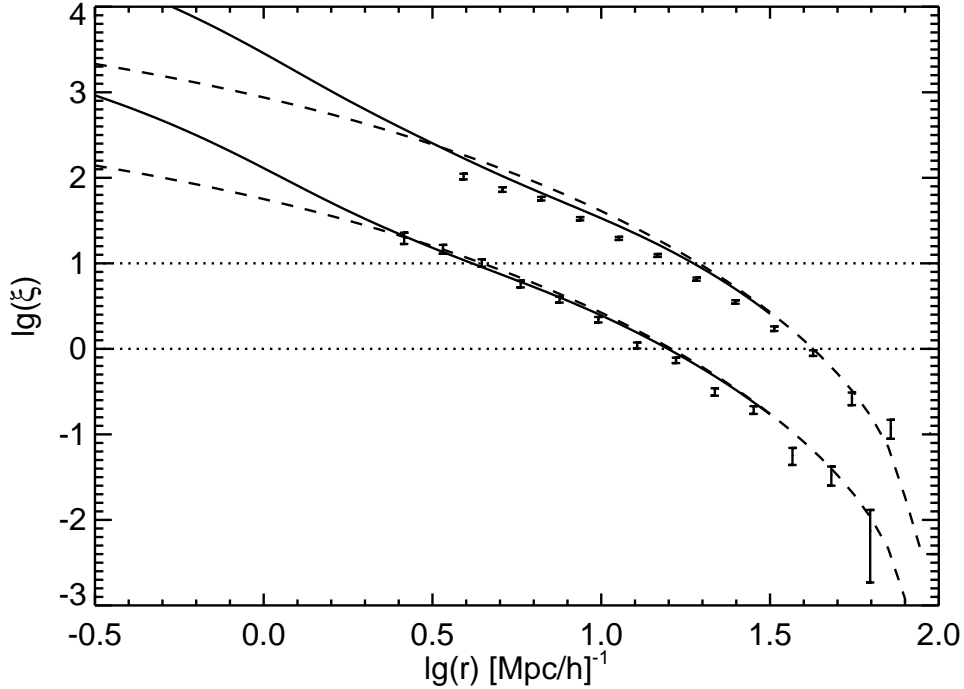
Figure 6.5.: The two–point correlation functions of the τCDM (lower part) and the ΛCDM model (upper part) for the $d_c = 50$ Mpc/h samples. This figure compares the results from the simulations (dots with errorbars), and the linear (dashed line) and nonlinear (solid line) Dark Matter correlation functions with the bias factors as specified by eq. 6.12. For the ΛCDM model, all quantities were shifted upwards by one order of magnitude. 1σ errorbars are plotted, as in fig. 6.4.

tion is fitted with a power law of the following form

$$\xi(r) = \left(\frac{r}{r_0}\right)^\gamma ,$$
(6.15)

where γ and r_0 are free parameters. Figure 6.6 gives the results of the fits for the correlation lengths. The boxes and diamonds are for the τCDM and ΛCDM simulation, respectively. The dotted and dot–dashed line are the results for the Mo & White *ansatz* using eq. (6.12) and the definition $\xi(r_0) = 1$. Also given are the results of Croft et al.'s analysis of the APM clusters and the linear scaling, eq. (6.7), proposed by Bahcall. The linear scaling fails to reproduce the relation between the cluster sample density and the correlation length completely. Interestingly, the analytical prediction by Mo & White (1996) lies above the simulation results. As already mentioned above, a similar trend was noted by Croft & Efstathiou (1994) when they used the model introduced in BBKS.

The APM clusters analyzed in Croft et al. (1997) follow the trend of the simulated clusters but have slightly larger amplitudes than the ΛCDM model. Probably only very large cluster
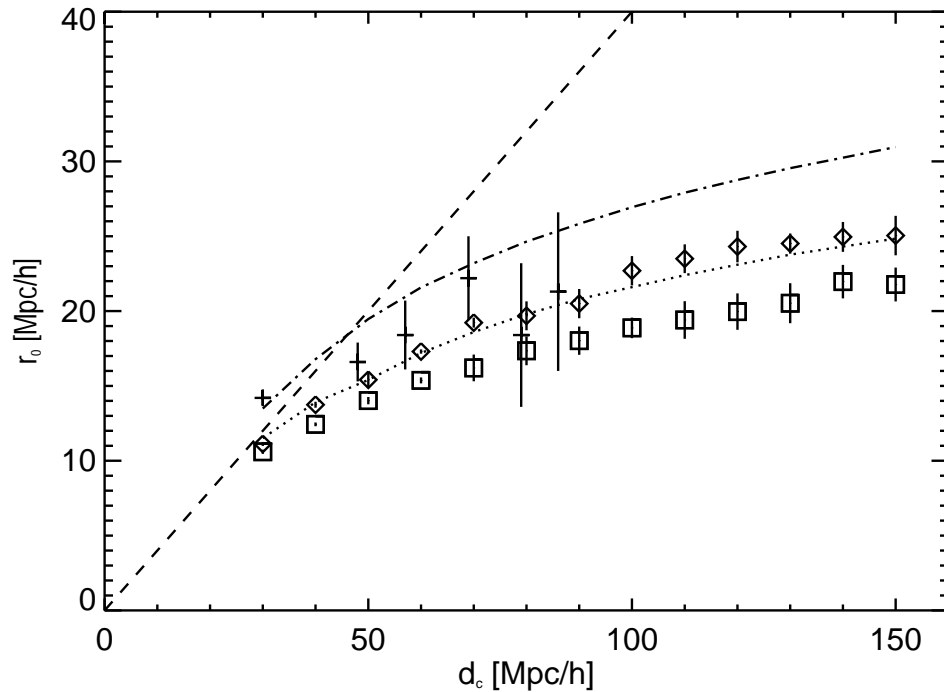
Figure 6.6.: The correlation length as a function of the mean intercluster separation d_c for the τCDM (boxes with errorbars) and ΛCDM (diamonds with errorbars) simulation. The prediction of the Mo & White model are given as dotted and dot–dashed lines for the respective simulations. The dashed line is the linear relation proposed by Bahcall. Also given are the APM data points taken from Croft et al. 1997 (crosses).

samples from the forthcoming 2dF and SDSS surveys will allow a determination of the correlation function of clusters in the real Universe which will end the debate outlined above. If Cold Dark Matter models of the type discussed above do indeed describe the Universe, then the correlation length of the richest clusters will not follow the linear scaling advocated by Bahcall & Cen (1992) but will turn over and rise only gently as shown above. Clearly, of the two cosmological models discussed here, the ΛCDM one is more consistent with the APM data.

6.6. Summary

The study of galaxy clusters in the largest cosmological N–body simulations done to–date has yielded some interesting results. An investigation of massive clusters at redshifts of $z \approx 0.8$ has shown that the model with $\Omega_0 = 1$ cannot produce enough massive clusters to account for the objects which have already been observed. The ΛCDM simulation doesn't have this problem – if the most massive observed cluster which doesn't seem to be a relaxed object is assumed to be anomalous. However, the case of this cluster means that this discussion has still

to be taken with a tablespoon of salt due to the uncertainties and statistics of the observational samples.

The high mass end of the analytical Press–Schechter mass function is followed very nicely by the galaxy clusters extracted from the Hubble Volume Simulations. The two different group finding schemes, $FOF_{0.2}$ and SO, show differences which are small and are understood from earlier work.

The two–point correlation function of galaxy clusters can be studied in unprecedented detail using the Hubble Volume Simulations. It was shown that the correlation function can be described in terms of the correlation function of the mass times a bias factor as introduced in the work by Mo & White (1996). However, a perfect match required slightly smaller bias values than they would predict. Fitting the correlation function around $\xi(r) \approx 1$ with a power law yields the correlation length, r_0. It was shown that the correlation length does increase with the mean separation, d_c of subsamples of the cluster catalogs. However, the relationship between r_0 and d_c is not linear – as expected for a fractal distribution – but it turns over gently. The prediction by Mo & White is in good qualitative agreement with what was found from the simulation but somewhat overpredicts r_0. The correlation lengths found for the clusters obtained from the APM catalog by Croft et al. (1997) are in good agreement with the ΛCDM model but are too high for the τCDM model.

Acknowledgements

Bibliography

[1] Abell G.O., ApJS, **3**, 211 (1958)

[2] Abell G.O., Corwin H.G., Olowin R.P., ApJS, **70**, 1 (1989)

[3] Bahcall N.A., Soneira R.M., ApJ, **270**, 20 (1983)

[4] Bahcall N.A., Cen R., ApJ, **398**, L81 (1992a)

[5] Bahcall N.A., West M.J., ApJ, **392**, 419 (1992b)

[6] Bahcall N.A., Fan X., Cen R., ApJ, **485**, L53 (1997)

[7] Bardeen J.M., Bond J.R., Kaiser N., Szalay A.S., ApJ, **304**, 15 (1986, BBKS)

[8] Bartelmann M., Ehlers J., Schneider P., A&A, **280**, 351 (1993)

[9] Blanchard A., Bartlett J.G., submitted to A&A, astro-ph/9712078

[10] Bond J.R., Cole S., Efstathiou G., Kaiser N., ApJ, **379**, 440 (1991)

[11] Carlberg R.G., Morris S.L., Yee H.K.C., Ellingson E., ApJ, **479**, L19 (1997)

[12] Clowe D., Luppino G.A., Kaiser N., Henry J.P., Gioia I.M., astro-ph/9801208

[13] Croft R.A.C., Efstathiou G., MNRAS, **267**, 390 (1994)

[14] Croft R.A.C., Dalton G.B., Efstathiou G., Sutherland W.J., Maddox S.J., astro-ph/9701040

[15] Donahue M., ApJ, **468**, 79 (1996)

[16] Donahue M., Voit G.M., Gioia I., Luppino G., Hughes J.P., Stocke J.T., excepted by ApJ (1998), also astro-ph/9707010

[17] Efstathiou G., Dalton G.B., Sutherland W.J., Maddox S.J., MNRAS, **257**, 125 (1992)

[18] Efstathiou G., in "Les Houches, Session LX, Cosmology and Large–Scale Structure", ed.s Schaeffer R., Silk J., Spiro M., and Zinn–Justin J., Elsevier Science B.V. (1996)

[19] Eke V.R., Cole S., Frenk C.S., MNRAS, **282**, 263 (1996)

[20] Eke V.R., Cole S., Frenk C.S., Henry J.P., submitted to MNRAS, astro-ph/9802350

[21] Gross M.A.K., Somerville R.S., Primack J.R., Borgani S., Girardi M., to appear in Proceedings of 12th Potsdam Cosmology Workshop, "Large-Scale Structure: Tracks and Traces" Sept. 15-19, 1997, also astro-ph/9711035

[22] Hauser G.M., Peebles P.J.E., ApJ, **185**, 757 (1973)

[23] Henry J.P., ApJ, **489**, L1 (1997)

[24] Jenkins A., Frenk C.S., Pearce F.R., Thomas P.A., Colberg J.M., White S.D.M., Couchman H.M.P., Peacock J.A., Efstathiou G.P., Nelson A.H. (The Virgo Consortium), ApJ, 499, in press (1998)

[25] Kaiser N., ApJ, **284**, L9 (1984)

[26] Lacey C., Cole S., MNRAS, **271**, 676 (1994)

[27] Luppino G.A., Gioia I.M., ApJ, **445**, L77 (1995)

[28] Luppino G.A., Kaiser N., ApJ, **475**, 20 (1997)

[29] Mo H.J., White S.D.M., MNRAS, **282**, 347 (1996)

[30] Mo H.J., Jing Y.P., White S.D.M., MNRAS, **282**, 1096 (1996)

[31] Oke J.B., Postman M., Lubin L.M., ApJ (accepted, 1998)

[32] Padmanabhan T., Structure Formation in the Universe, Cambridge University Press 1993

[33] Peacock J.A., West M.J., MNRAS, **259**, 494 (1992)

[34] Peacock J.A., Dodds S.J., MNRAS, **267**, 1020 (1994)

[35] Peebles, P.J.E., Principles of Physical Cosmology, Princeton University Press 1993

[36] Pen U.L., submitted to ApJ, astro-ph/9610147

[37] Postman M., Huchra J.P., Geller M.J., ApJ, **384**, 404 (1992)

[38] Press W.H., Schechter P.L., ApJ, **187**, 425 (1974)

[39] Reichart D.E., Nichol R.C., Castander F.J., Burke D.J., Romer A.K., Holden B.P., Collins C.A., Ulmer M.P., submitted to ApJ, astro-ph/9802153

[40] Richstone D., Loeb A., Turner E.L., ApJ, **393**, 477R (1992)

[41] Romer A.K., Collins C.A., Cruddace R.G., MacGillivray H., Ebeling H., Böhringer H., Nature, **372**, 75 (1994)

[42] Sadat R., Blanchard A., Oukbir J., A&A, **329**, 21 (1998)

[43] Tozzi P., Governato F., to appear in "The Young Universe", ed.s D'Odorico S., Fontana A., and Giallongo E., A.S.P. Conf. Ser. (1997) also astro-ph/9711258

[44] Viana P.T.P., Liddle A.R., MNRAS, **281**, 323 (1996)

[45] White S.D.M., Efstathiou G., Frenk C.S., MNRAS, **262**, 1023 (1993)

[46] White S.D.M., in "Les Houches, Session LX, Cosmology and Large–Scale Structure", ed.s Schaeffer R., Silk J., Spiro M., and Zinn–Justin J., Elsevier Science B.V. (1996)

[47] Zehavi I., Riess A.G., Kirshner R.P., Dekel A., ApJ, **503** (1998)
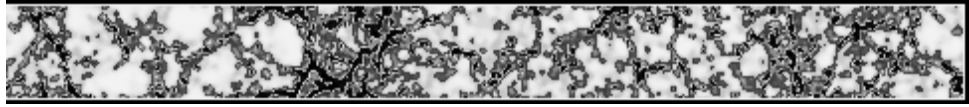
Linking Cluster Formation to Large Scale Structure

Look for a problem that is interesting and important – never mind how it is classified – and tackle it.

Mancur L. Olson

7.1. Introduction

In the preceding Chapters, Large–Scale Structure (LSS) was viewed from different angles. Two–dimensional pictures of slices through the various simulation sets showed a rather complicated situation where objects which are themselves clustered are interconnected by a network of filaments and sheets. From this viewpoint, which was used in Chapter 3, it was unclear which structure element dominated. Filaments, sheets, clusters, and voids all showed up in the simulations. In Chapter 4 it became evident that as a consequence of gravity being a long–range force any object defined in some way is part of a bigger object when the criterion used to find the object is relaxed. There, the adaptively smoothed density field was investigated, and the sizes and masses of objects as a function of an overdensity threshold were measured. It was found that for thresholds close to the mean density, most of the mass was in *one* single object which extended all across the simulation volume. For high thresholds, the mass above this threshold was distributed in many small objects (small in terms of the size of the volume). For a hypothetical arbitrarily fine mesh an overdensity threshold of 178 would yield all virialized objects. The most massive objects, corresponding to rich clusters of galaxies which are investigated in Chapters 5 and 6 are of particular importance. Observationally, it is not the density field which is observed but galaxies and thus galaxy clusters. Galaxy clusters are tracers of the underlying mass distribution. As seen in Chapter 5, galaxy clusters correspond to high peaks in the smoothed initial density field. It was also seen that the peculiar velocities of galaxy clusters

deviate from the prediction of Linear Theory because of non–linear effects. Thus, there is an interesting interplay between galaxy clusters and LSS. On the one hand, galaxy clusters trace LSS like the highest peaks of a reef which mark the reef itself during high tide. On the other hand, LSS has a strong influence on the properties of galaxy clusters. From this perspective, it is natural to investigate the formation process of galaxy clusters more closely. The main point of interest here will be the infall pattern of the mass which falls onto a (proto–) cluster. Once that is done, the spatial distribution of the mass which surrounds galaxy clusters will be investigated. That way, further insight into a still open question will be gained which is not only related to simulations but especially to observations.

Currently, there is an ongoing debate about how best to describe LSS. Sheets or walls (Geller & Huchra 1989, de Lapparant et al. 1986), filaments (Giovanelli et a. 1986), and mixes of these to produce a cell–like geometry (Jôeveer & Einasto 1987) have all been suggested. In an earlier work, Bond et al. (1995) have shown that this mix already shows up in the overdensity pattern of the initial Gaussian density field – which is related to the cluster peak correspondance mentioned above. So far, no consensus has been reached on which component of LSS might be predominant. But this ambiguity has something to offer. Here, I attempt to investigate LSS starting from objects which are well–defined. It is widely believed that the formation process of galaxy clusters is linked to LSS. So the idea is to have a look at how clusters build up and then to gain insight into how this is connected to the mass distribution outside the clusters. Note that *a priori* no hypothesis is made of what LSS consists of. Rather, it is the aim of this Chapter to understand this very point.

7.2. The Formation of Clusters

7.2.1. The Simulations

The GIF simulations are well–suited for this work because of their high mass resolution. In addition, there exist a large number of output times so that the formation process of galaxy clusters, which occurs at redshifts lower than $z = 1$, can be investigated in detail. From the four simulations, two are taken, namely the τCDM and the OCDM simulation. As seen in Chapter 4, the two other simulations are nearly indistinguishable from the OCDM simulation with respect to the spatial distribution of the mass. And if the difference in the dynamics between high and low Ω models leads to a difference in the formation process, it will clearly show up most strongly between the τCDM and the OCDM models. The output redshifts taken are $z = 0.93, 0.82, 0.72, 0.62, 0.52, 0.43, 0.35, 0.27, 0.20, 0.13, 0.06,$ and 0.0.

7.2.2. The Selection of Clusters

The cluster selection taken here is identical to the one used in Chapter 5 for the study of the peculiar velocities of clusters. Spheres of radius $r_A = 1.5 \, h^{-1} \, \text{Mpc}$ are put around dense knots found with a friends–of–friends group finder with a dimensionless linking length of $b = 0.05$ times the mean interparticle separation. Overlapping spheres are later merged. From each model the ten most massive clusters are taken. These span a mass range from
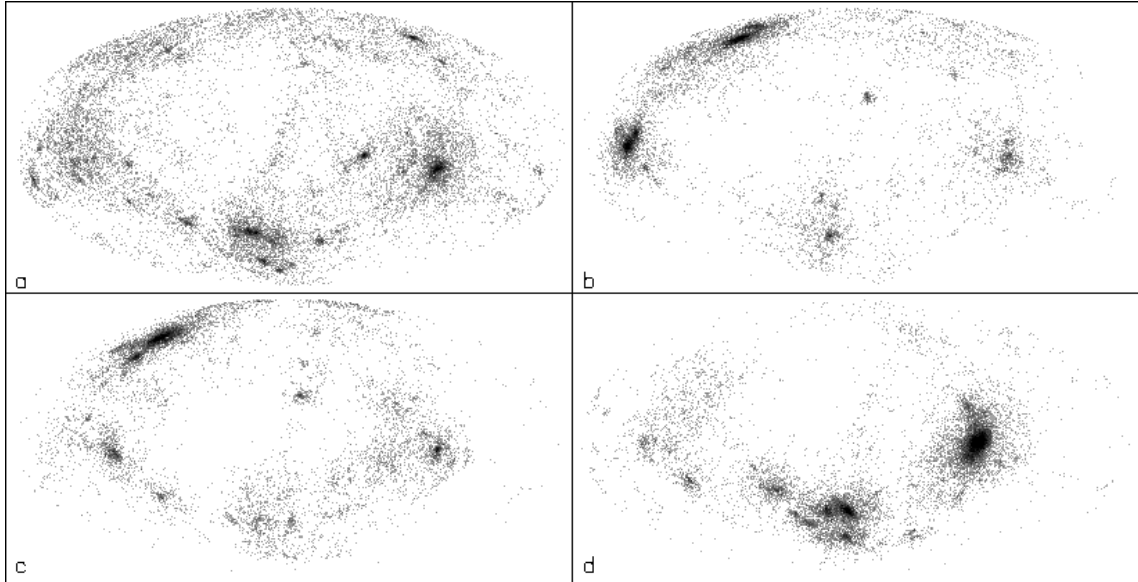
Figure 7.1.: The infall pattern of matter onto a cluster in the τCDM model viewed by a hypothetical observer in the barycenter of the system. Shown are different time intervals: (a) $z = 0.$ to $z = 0.13$, (b) $z = 0.13$ to $z = 0.27$, (c) $z = 0.27$ to $z = 0.43$, and (d) $z = 0.43$ to $z = 0.62$.

$2.7 \times 10^{14}\,h^{-1}\,M_\odot$ ($3.5 \times 10^{14}\,h^{-1}\,M_\odot$) to $7.3 \times 10^{14}\,h^{-1}\,M_\odot$ ($8.4 \times 10^{14}\,h^{-1}\,M_\odot$) for the τCDM (OCDM) model.

7.2.3. Construction of the Formation History

After having found the clusters at $z = 0$ the particles in each of them are marked in a list, and are then extracted from the whole set of particles at all redshifts. Two additional pieces of information are derived for each particle: The time when it falls into the cluster and its position at that time. This is done in the following manner. Given the selection criteria, a cluster is a spherical object with a radius $r_A = 1.5\,h^{-1}\,$Mpc (comoving) at any time. Let the current time be z_i. Going back to z_{i-1}, some of the particles which will be inside r_A at z_i are still outside. Hence, these particles will fall into the cluster between z_{i-1} and z_i. So for these particles z_{i-1} as well as their position at this time are saved. As the center of the cluster the barycenter at z_{i-1} of the biggest lump is taken.

7.2.4. Investigating the Formation of the Clusters

As described in Chapter 5, the formation of a cluster is usually modeled by the spherical collapse of some high peak in the initial density field. However, previous studies, e.g. Tormen et al. (1997), have already shown that the actual formation process in hierarchical models is rather irregular. Instead of a steady accretion of matter, lumps fall onto a pre–existing object,

a typical process well known in CDM models.

A hypothetical observer was placed at the barycenter of each cluster. This observer watches the matter as it falls into the cluster. For spherical infall he would see matter coming in more or less randomly from all directions. For each observer, maps of the infall pattern are produced by plotting the positions of the particles at infall using a two–dimensional projection which is known as the Aitoff projection. Figure 7.1 shows typical examples of such maps for a cluster in the τCDM simulation. From this some points can be addressed. First, it is obvious that matter is not falling in uniformly over the sky of the hypothetical observer as one would expect in a spherical infall model. Rather infall occurs from distinct directions. Second, there is a tight correlation between the infall directions at different times. The cluster forms by accretion from a few preferred directions.

This process can be quantified by computing the autocorrelation function of the infalling matter

$$1 + \omega(\vartheta) = \frac{4\pi}{A(\vartheta)} \frac{N_{\mathrm{PP}}(\vartheta)}{N(N-1)} \,, \tag{7.1}$$

where $N_{\mathrm{PP}}(\vartheta)$ denotes the number of particle pairs separated by an angle $\vartheta + \delta\vartheta$, $A(\vartheta) = 2\pi \sin\vartheta\, \delta\vartheta$ is the size of the annulus, and N is the total number of particles in the sample. Obviously, $\omega(\vartheta)$ is the excess probability of finding a particle pair with separation $\vartheta + \delta\vartheta$ in the simulations compared with spherical infall.

Figure 7.2 shows the autocorrelation functions for the infalling matter of the cluster in fig. 7.1 and for random spherical infall. For small angles all the curves have a peak. This just reflects the particle clumps seen in fig. 7.1. The strength of the peaks directly reflects the amount of matter in these clumps. For some of the curves, peaks also appear at larger angles. For example, curve (b) has a second peak around $60°$. This reflects the angle between the two most massive objects in fig. 7.1(b).

These curves can be directly compared with the correlations of matter between different maps, as quantified by the crosscorrelation function

$$1 + \omega(\tilde{\vartheta}) = \frac{4\pi}{A(\vartheta)} \frac{N_{\mathrm{P_1 P_2}}(\vartheta)}{N_1 \cdot N_2} \,, \tag{7.2}$$

where $N_{\mathrm{P_1 P_2}}(\vartheta)$ denotes the number of pairs of a particle from map 1 and one from map 2 separated by an angle $\vartheta + \delta\vartheta$, where $A(\vartheta) = 2\pi \sin\vartheta\, \mathrm{d}\vartheta$ is the size of the annulus again. N_1 and N_2 are the total number of particles in the maps 1 and 2, respectively.

Figure 7.3 shows cross correlations between pairs of maps from fig. 7.1. These have similar scale but are generally weaker than the autocorrelations. This can be seen by comparing the maps directly, too. The behaviour for this particular cluster is typical for both the auto– and cross–correlations in the infall patterns of *all* clusters in *both* the τCDM and OCDM models. Not a single case was found which deviates qualitatively from it.

From the above, it is apparent that correlations between the infall patterns at different times are strong. Can such correlations be expected? From previous studies, e.g. Tormen et al. 1997, it is clear that clusters form by the accretion of haloes. This process is clearly reflected by the discussion above. But why is then the infall pattern of matter between so many and so different redshift intervals correlated? Obviously, there must be a connection between the infall pattern and LSS itself. This will be discussed in the next section.
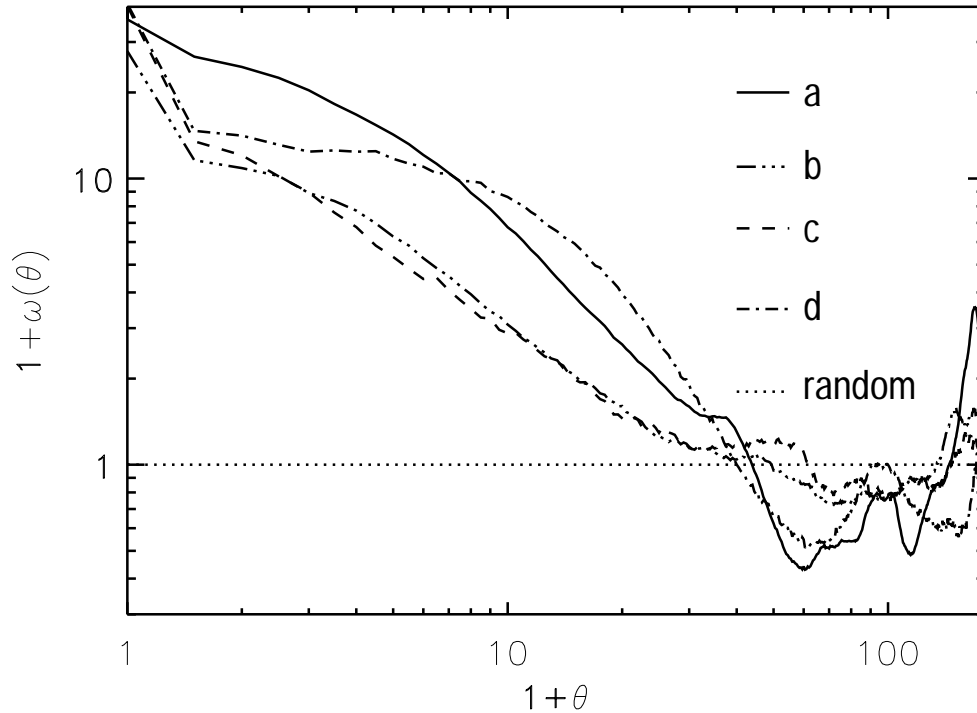
Figure 7.2.: The autocorrelation functions of the matter shown in fig. 7.1 for the same time intervals used in the four panels of fig. 7.1. Also shown is the prediction for spherical infall (random).

7.2.5. Connecting Cluster Formation and Large Scale Structure

From the above it is obvious that during the formation of a cluster matter falls in from well–defined directions. What is the connection between these directions and Large Scale Structure? In order to investigate this issue the distribution of matter surrounding the clusters at $z = 0$ is obtained as follows. Around the clusters onion–like shells of thickness $1.5\,h^{-1}\,$Mpc are put. All particles in a shell are extracted. The hypothetical observer at the cluster center drew maps of these particles, i.e., LSS is viewed from the center of each cluster.

Figure 7.4 shows maps for shells surrounding the τCDM cluster analyzed in figures 7.1 to 7.3. Again, these maps are typical of those found for all the clusters. The maps show various points. First, there exist density enhancements in the distribution of the particles which only marginally change their locations from map to map. Most of them are more or less circular. These must clearly be filaments extending outwards from the cluster. In addition, fig. 7.4 shows another interesting feature. There are enhancements which connect the filaments and also extend outwards from map to map, but are less dense. Figure 7.5 shows the LSS around a different τCDM cluster where these connections between the filaments are very strong. There is a U–shaped broad band in the right part of five of the six maps. This object is obviously a
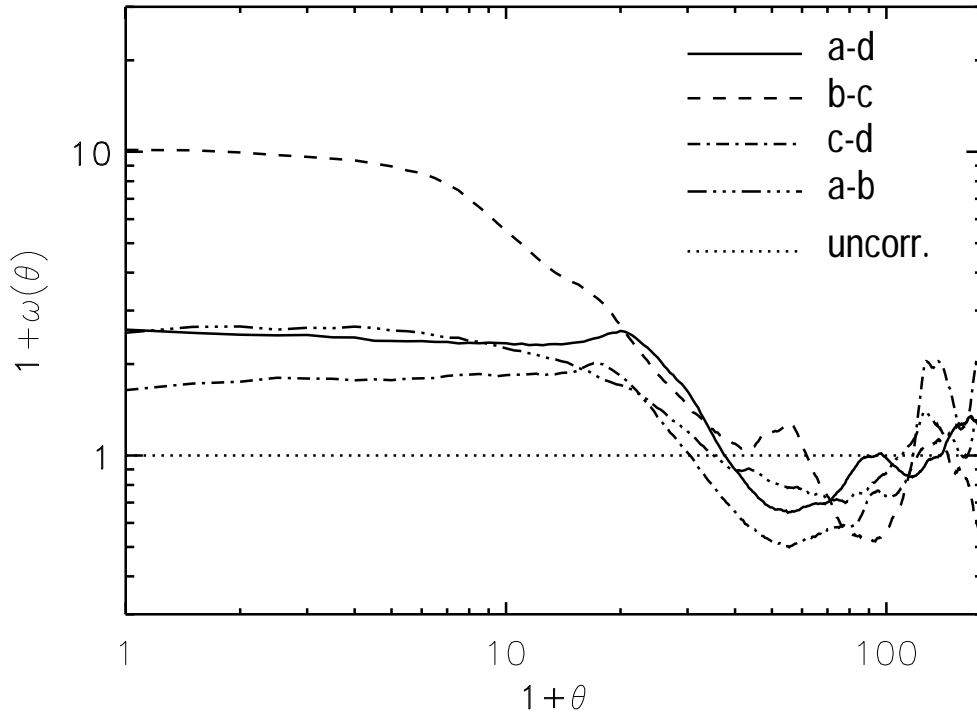
Figure 7.3.: The cross correlation between pairs of maps from fig. 7.1. Also shown is the result expected for uncorrelated maps (dotted).

sheet. One has to note that filaments can be found in *all* of the cluster maps. There are connections between them in all maps, too. However, impressive examples of sheets like the one in figure 7.5 are rare. Second, when comparing the maps in figure 7.4 with the one in fig. 7.1 it can be seen that the big clumps fall in along the filaments. This is true not only for the lowest redshift range but for the earlier ones, too. Even at a redshift of 0.6 infall onto clusters is tightly coupled to LSS at $z = 0$.

This connection can be quantified by means of the angular cross correlation functions between the combined infall maps of the cluster and the LSS maps, computed for each cluster in each cosmology. Figure 7.6 shows cross correlations between the infall patterns and surrounding LSS for the ten τCDM and OCDM clusters. These are averaged over the redshift ranges and radii shown in figures 7.1, 7.4, and 7.5. This mean cross correlation behaves in a similar manner to the cross correlations between the different maps (Fig. 7.3). There is indeed a well defined correlation between the infall onto clusters and their surrounding LSS. This correlation does *not* depend on Ω.
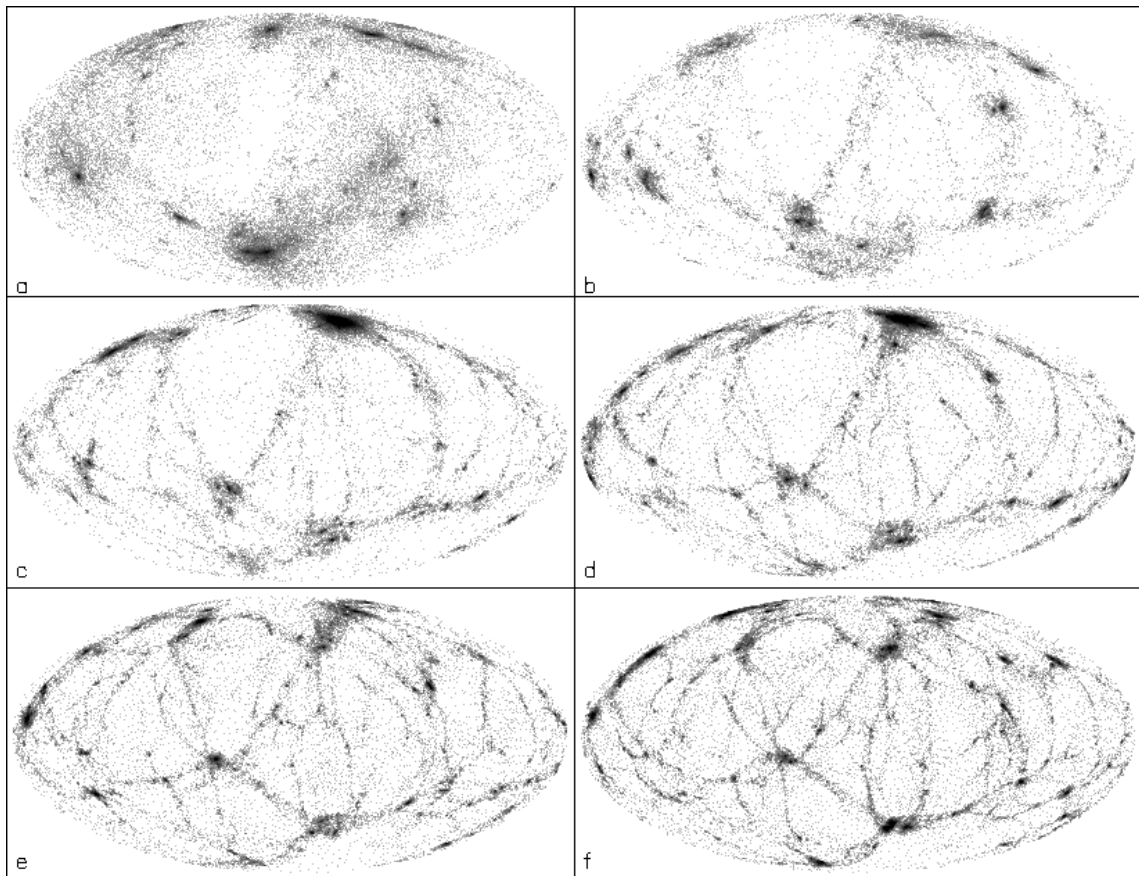
Figure 7.4.: The LSS around the cluster shown in fig. 7.1 viewed by a hypothetical observer at the barycenter of the cluster at $z = 0$. Shown are shells at 1.5 to 3.0 (a), 3.0 to 4.5 (b), 4.5 to 6.0 (c), 6.0 to 7.5 (d), 7.5 to 9.0 (e), and 9.0 to 10.5 h^{-1} Mpc (f) from the cluster center.
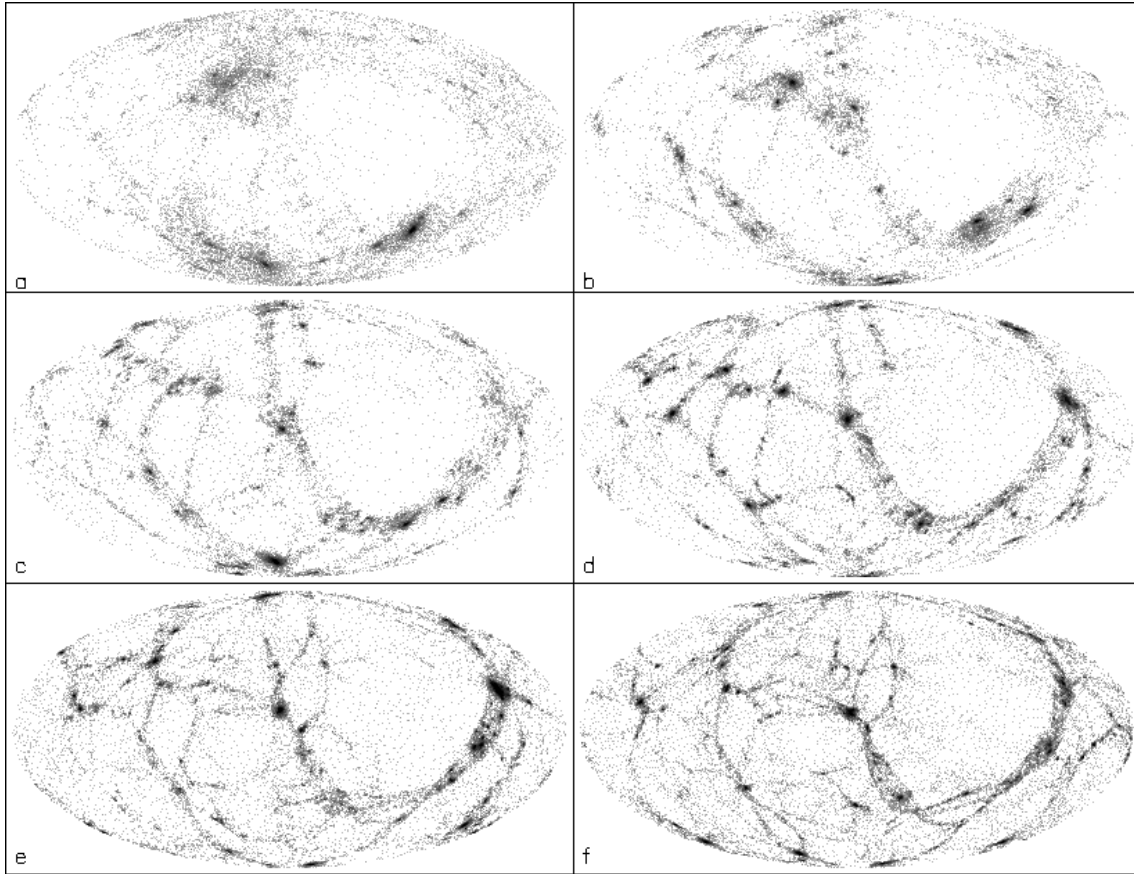
Figure 7.5.: The LSS around another cluster from the τCDM simulation shown using the same representation as in fig. 7.4.
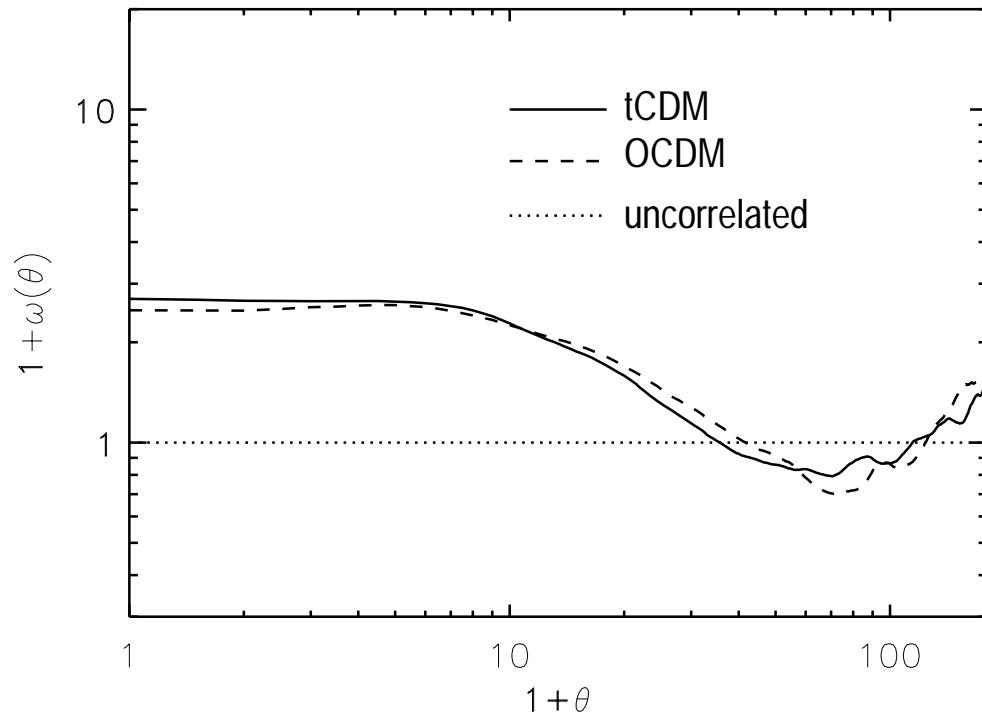
Figure 7.6.: The combined cross correlation between the infall patterns of the clusters in the τCDM and OCDM simulations and their surrounding LSS.
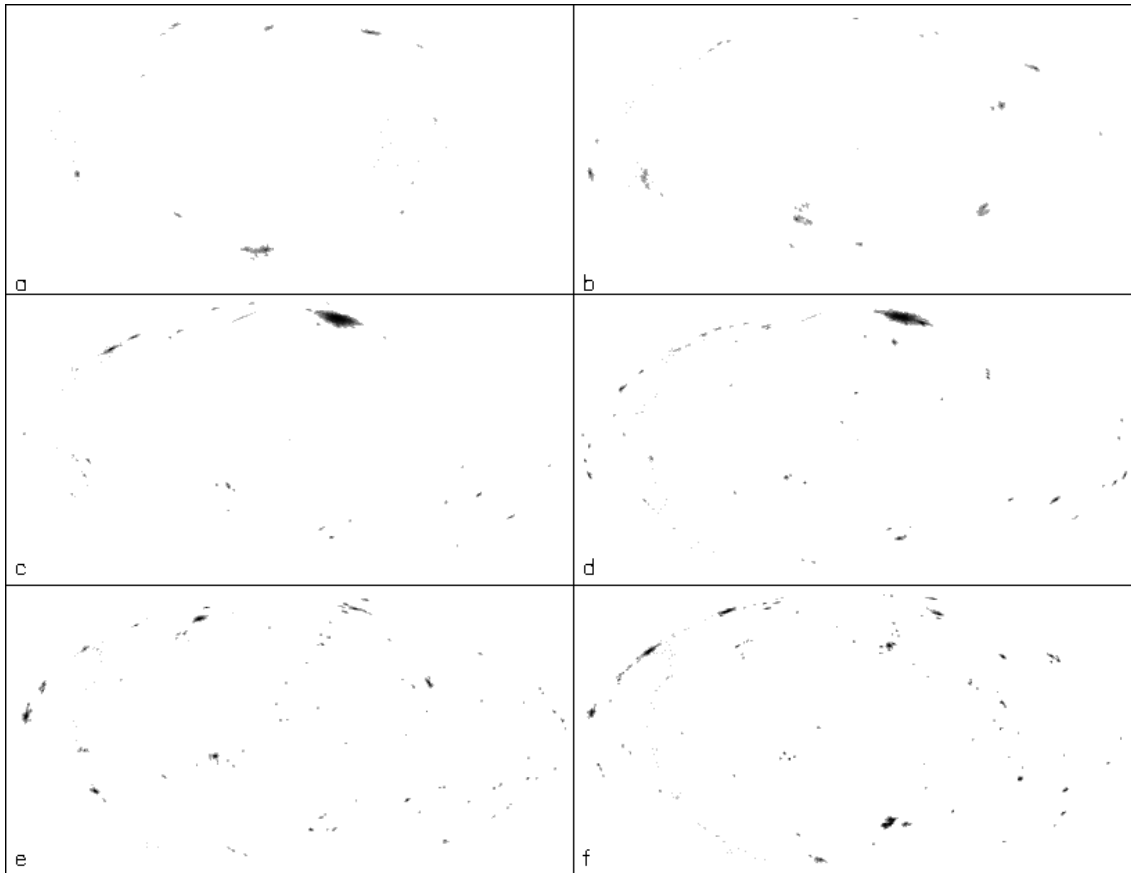
Figure 7.7.: A different representation of fig. 7.4 where only the lumps (filaments) show up.

Radius	Fig. 7.4			Fig. 7.5		
[Mpc/h]	f_{all}	f_1	f_2	f_{all}	f_1	f_2
$1.5 - 3.0$	11%	5%	2%	13%	9%	2%
$3.0 - 4.5$	22%	3%	3%	24%	4%	4%
$4.5 - 6.0$	52%	42%	2%	28%	10%	3%
$6.0 - 7.5$	45%	32%	1%	34%	5%	4%
$7.5 - 9.0$	32%	7%	4%	43%	17%	3%
$9.0 - 10.5$	39%	8%	5%	32%	6%	2%

Table 7.1.: Fractions of mass in the dark spots for the maps in fig. 7.4 and 7.5. Given are the total mass fractions (f_{all}) as well as the mass fractions of the two biggest spots (f_1 and f_2) for the different radii.

7.2.6. Fraction of Mass in the Peaks

What is the amount of mass which can be seen in the various structures in the above maps? In order to answer this question the amount of mass inside the dark spots has to be computed. This was done by using a standard friends–of–friends group finder on the sets of points on the unit sphere from which the above maps were drawn. As linking parameter a value of $b = 0.2$ times the mean interparticle separation is taken. All objects with 20 or more particles are considered as big groups.

Table 7.1 gives the fraction of mass inside such big dark spots for the figures 7.4 and 7.5 (f_{all}). Also shown is the fraction of mass in the two most massive spots in each map (f_1 and f_2). Typically, about a third of the mass lies in filaments at the overdensity of $\sim$20 picked out by the choice of linking length. Note, that with this procedure sheets can not be "detected". Their density contrast is significantly lower than that of filaments – as can be seen from figures 7.4 and 7.5.

Fig. 7.7 shows a representation of the maps in fig. 7.4 where only the particles in these dark spots, i.e. the filaments, are plotted. Apparently filaments are clumpy structures rather than homogeneous cylinders.

Performing a similar analysis for the infall patterns onto clusters gives results which vary more strongly between clusters and time intervals. E.g., for the cluster shown in fig. 7.1 the fractions of mass in the dark spots are 5%, 15%, 30%, and 51% for the maps (a) to (d), respectively. This scatter between 5% and around 55% is quite typical for clusters in both the τCDM and the OCDM sample.

For the whole τCDM (OCDM) cluster sample the averaged mass fractions in the filaments are 14% (14%) , 29% (35%), and 42% (46%) for shells beginning at radii 1.5, 3.0, and 4.5 h^{-1} Mpc. These values stay constant at around 40% (48%) for larger radii. There is a slightly larger mass fraction in the filaments in the low Ω model. This has already been found in Chapter 4 where the LSS was investigated by means of a percolation analysis.

7.3. Summary

The study of the formation process of clusters and its connection with LSS has yielded several conclusions. First, as already noted by many other studies, in CDM universes clusters form by the accretion of collapsed haloes onto other pre–existing haloes. This occurs from preferred directions. These directions do not change much with time. Second, there is a correlation between the formation process of a cluster and its surrounding LSS. Qualitatively speaking, matter falls in mainly from filaments and sheets. Filaments show up as clear density enhancements in the 2D projections used above. They extend outwards from the cluster center and are connected by less dense sheets of matter. Because of their considerably lower density contrast these sheets are nearly impossible to find in 3D representations of N–body simulations (compare Chapter 4). The above representation clearly shows that both filaments and sheets do exist in simulations. Quantitatively speaking, the amount of mass in the filaments is around 40% and 48% of the total mass for radii from 4.5 to 10.5 h^{-1} Mpc in the τCDM and OCDM model, respectively. At smaller radii, it is around 30%. However, the mass distribution is dominated by lumps inside the filaments. Third, the only difference which can be found between the τCDM and the OCDM model is in the amount of mass in the filaments, it is slightly larger for the OCDM model. This agrees with the results from Chapter 4 where the amount of mass inside overdense regions for any overdensity threshold was always larger for the OCDM than for the τCDM model.

The formation process of each cluster is governed by its surrounding LSS. The internal properties of the cluster may change during its formation, as shown by Tormen et al. (1997). This process is not chaotic but it is linked to the LSS.

Bibliography

[1] Bond J.R., Kofman L., Pogosyan D., astro-ph/9512141

[2] de Lapparant V., Geller M.J., Huchra J.P., ApJ, 302, L1 (1986)

[3] Geller M.J., Huchra J.P., Science, 246, 897 (1989)

[4] Giovanelli R., Haynes M., Myers S.T., Roth J., AJ, 92, 250 (1986)

[5] Jôeveer M., Einasto J., in IAU Symp. 79, The Large–Scale Structure of the Universe, eds. Longair M.S., Einasto J. (Dordrecht: Reidel), 241 (1978)

[6] Tormen G., Bouchet F.R., White S.D.M., MNRAS, 286, 865 (1997)
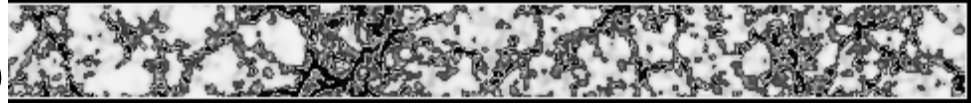
Chapter 8

The N–body Simulations

This Chapter gives an outline of the general technique used for the N–body simulations. In section 8.1, AP^{3}M is introduced. Then, in section 8.2, a part of the development of a version which can be run on a Cray T3E parallel supercomputer.

8.1. AP^{3}M

8.1.1. Basics

The aim of the computer code is to follow the movements of N particles subject to their own mutual gravity in a cosmological volume. Gravity is a long–range force, so for each particle the acceleration due to the other $N - 1$ particles must be obtained to compute the resulting velocity and the change in the position. The simplest way to do this is to compute the forces between all pairs. This is known as the Particle–Particle (PP) algorithm. Using the comoving coordinates introduced in section 2.1, the equation of motion of the i–th particle is

$$\frac{\mathrm{d}\mathbf{v}_i}{\mathrm{d}t} + 2\frac{\dot{a}}{a}\mathbf{v}_i = -\frac{G}{a^3}\sum_{j\neq i} m\frac{\mathbf{x}_i - \mathbf{x}_j}{|\mathbf{x}_i - \mathbf{x}_j|^3} \;. \tag{8.1}$$

Here, $\mathbf{x}_i$ is the position of the i–th particle, $\mathbf{v} = \dot{\mathbf{x}}$ is its velocity, m is its mass (Peebles 1980). The overdot denotes differentiation with respect to time, G is the gravitational constant, and a is the expansion parameter (compare eq.s (2.22) and (2.23)).

   The PP algorithm has a huge disadvantage. As the number of particles, N, is increased, the number of operations needed for computing the forces grows as N^2. A solution to this problem is to divide the force into a short–range component, computed using the direct summation above, and a long–range component. One way to compute the latter is the Particle–Mesh (PM) algorithm. Here, the particles are assigned to a mesh with an appropriate smoothing function to get a discrete density distribution. Then, the long–range forces can be obtained using Poisson's equation by means of a Fast Fourier transform (FFT). The scheme works as follows:

1. Particles are assigned to a grid with an appropriate smoothing function (kernel). This produces a discrete density distribution.

2. The density distribution is convolved with the Green's function, G. This gets a potential at mesh points.

3. The potential is differenced to obtain forces at mesh points.

4. The forces are interpolated back onto the particles with the same kernel as above.

The FFT technique is particularly interesting for a cosmological simulation. As the Universe in principle is infinite, there will always be contributions to the forces from scales which are much bigger than the simulated volume. A standard way of dealing with this is to assume periodic boundary conditions. The FFT technique does this automatically. On small scales, its accuracy is limited – the Nyquist theorem essentially states that all forces on scales smaller than two mesh cells are inaccurate. On these scales, the forces must be obtained by the direct summation of the PP algorithm.

Combining these two algorithms gives the Particle–Particle Particle–Mesh (P^3M) algorithm. For a fairly uniform distribution it behaves like a PM algorithm. However, once the particle distribution becomes clustered, the PP part starts to dominate. The aim of a cosmological simulation usually is two–fold: It is desirable to have a large computational volume *and* a high mass resolution, that is many particles per object. Obviously, the latter is a problem for P^3M. For a highly clustered distribution, the PP part consumes a huge amount of time, and the code is slow. One way to overcome this is to allow for mesh refinements of heavily clustered regions. If applied to a P^3M algorithm, this technique is called Adaptive P^3M (AP^3M, Couchman 1991). It finds highly clustered regions and places a refined P^3M region with a finer mesh on it. This subregion then consists of a non–periodic PM part with a smaller mesh size and a PP part which is set up in the same fashion as on the top level, that is on the whole volume. The idea is to shift PP work on the top level to PM work on the refined level. This algorithm can be iterated by placing another refined region into the first level of refinements etc. If the total CPU time per time step is measured for a simulation run with AP^3M, it stays roughly constant (see Pearce & Couchman 1997) whereas it increases linearly otherwise. The basic scheme works as follows:

1. Find those regions where the placement of a refinement would reduce the computational work[1].

2. Compute PM on all particles and PP only on particles which are not in to be refined zones.

3. Do a further P^3M calculation on those regions found above such that only the short range part of the forces of the standard P^3M force (that is, the one from the base mesh) are computed.

4. Accumulate the forces, update the particle data, and iterate.

---

[1] Actually, the refinement placing is the trickiest part of the AP^3M code, and different schemes for doing so exist. However, the basic idea always remains the same, regardless of how it is phrased.

8.1.2. The code

The first simulations were run on a CRAY T3D with 128 processors at the Computer Center of the Max–Planck–Gesellschaft in Garching. A parallelized version of AP^{3}M was available. The parallelization was done by Pearce & Couchman (1997) using `CRAFT`, which is a set of compiler options, that is, the compiler itself determines the way particles are distributed over the processors. All information is sent automatically between processors. This version of the code is reasonably fast on a T3D. However, due to the way the parallelization is set up, once the simulations became too heavily clustered (as was the case for the GIF simulations, see Chapter 3.2), a larger T3D was necessary to finish the runs. The reason for this is the limited amount of memory (64 MB) each processor on the T3D owns. The runs were then finished on the T3D at the Edinburgh Parallel Computer Center.

The Max–Planck–Society had decided to acquire a CRAY T3E, which finally arrived in January 1997. For this computer, no simulation code was available which could be used because CRAY had not developed `CRAFT` for the T3E. So the original serial version of AP^{3}M had to be taken and parallelized for the T3E. This was mainly done by MarFarland (for a description of the implementation of the message passing concept `shmem` see MacFarland et al. 1998). Some of the work described here was devoted to parallelizing parts of the code. This will be described in detail in the following section. Details about `CRAFT` and `shmem` can be found in the Cray MPP Fortran Reference Manual, SR-2504, 6.2.1 and in Application Programmer's Library Reference Manual, Vol. 2, SR–2165.

8.2. Code Development

The parallelization of AP^{3}M was done in two stages. First, a parallel P^{3}M was developed. This code can be used for systems which are not too heavily clustered – otherwise the code becomes very slow and inefficient. The second part is the implementation of the refinements – this is a future project and will probably require as much effort as the P^{3}M part itself. Two main tasks were parallelized as part of the effort to get a `shmem` version of P^{3}M: the particle update and the parallel input of data.

Because the particle update scheme was changed in a later stage of the implementation of `shmem` it will be described only briefly. The particles are distributed on the processors using a domain decomposition. That means that each processor "owns" well–defined regions in space. Here, the distribution of particles is split into separate regions in the x–y plane, that is into columns. Each processor owns a set of non–adjacent columns across the simulation volume. To compute the pairwise forces a processor has to store the particle data in the regions surrounding its actual domain (ghost cells). Originally, the information of which particle belongs to which processor was stored by means of a linked list as follows. For the whole particle set, a one–dimensional array is set up. Each particle has an entry in this array. A processor only knows the index of one particle. It can access all other particles via the linked list. Assume this particle has the index `i` and the array be `list`. Then, `list(i)` is the index of the next particle, `j`. `list(j)` contains the index of the next particle, `k` and so on. The list is set up to be circular so that the processor knows it has collected all particles once `list(l)=i`, where `l`

is the numberof the final particle which belongs to the processor.

As the simulation evolves, particles move. In particular, they can change the processor to which they belong. The particle update consisted of the following parts:

1. Update the particle data using the computed forces.

2. Check whether a particle has moved so that it belongs to different processor.

3. Update the particle list. The way this was done was to set it as the first particle of the corresponding processor and change the indices of `list` accordingly. That meant changing the linked list such that the two involved processors could access all particles they owned.

Of course, the actual coding was more complicated than described here. Most of the concepts which are described abover were used for the parallel input of the data in modified form. As the particle update was changed later (the linked list was removed in order to save space, the particles are now being sorted) only the full details of the parallel input are given in the following.

8.2.1. Parallel I/O: Reading in from multiple files

Introduction

Input and output of data (I/O) is one of the bottlenecks of any parallel system unless it is done efficiently, that is in parallel. On the T3D, this is not possible. Only $PE0$[2] can communicate with the outer world which consists of another supercomputer (in Garching this was a CRAY Y/MP Vectorcomputer). This, and the fact that the data to be read or written consists of *all* the relevant simulation data results in an enormous amount of time which is spent with I/O only. It amounts to about 30% to 40% of the whole time used on the T3D.

The situation changed with the advent of the T3E which allows parallel I/O. As already mentioned above, the simulation code was re–parallized by Tom MacFarland using the explicit message passing scheme `shmem`. The first version consisted of the P³M part which allowed parallel output only. Input of the data had to be done from *one* file. From the above it is obvious that this situation had to be changed in order to make more efficient use of the T3E[3]. Thus, setting up a routine which allows parallel input from multiple files was necessary. The following describes how this was achieved.

The Data Structure

To understand the basic problem, the data structure itself must be described. The particle data is distributed across a set of files. The number of these files can be set by specifying the number of I/O processors, because each one writes its own file. This is done in a straightforward

---

[2] `PEn` here stands for processor number `n`.

[3] In addition, having multiple output files but needing only one input file presented additional problems: The files had to be concatenated using scripts in order to have a restartable configuration. However, with particle sets of $3 \cdot 10^6$, particle positions, velocities, numbers, and masses add up tp roughly 900 MByte of data. It was not at all obvious that the operating system could handle files of this size correctly.

fashion – from which some complications result. Each I/O processor writes its own particle data and communicates with a fixed sub–set of the non–I/O processors. That is, it reads their particle data and writes them into the same file as its own data. The number of particles each I/O processor writes is *not* constant. This is because the distribution of the particles is generally not homogeneous (with the exception of the very early stages of the simulation, but even there small fluctuations exist). Hence, each processor stores some number of particles which is different from the number of particles divided by the number of processors. The code was set up by Tom MacFarland such that it did (and still does) not store the number of particles in each file. Only the total number of particles, plus the major parameters of the simulation, is written to a file. PE0 writes these parameters in front of the particle data as a header. The routine which reads from multiple files must be able to deal with this fact.

The basic structure of the routine should be:

- Only PE0 has to read the header information before reading in the particle data.

- All I/O processors have to be able to read in data for some arbitrary number of particles without knowing this number in advance.

- The I/O processors have to communicate with the non–I/O processors and send them data they need.

On the T3E, each processor can in principle do I/O. However, in the simulation code reading and writing data is done only by a subset of all processors. This number of I/O processors is set by the user as a parameter before the code is compiled. One of the basic features of shmem is that it is an *asynchronous* message passing scheme. This means that one processor can send data to another processor and the latter does *not* need to receive it at exactly the same time, it may do something else. Thus, sending the data from the I/O processors to the non–I/O processors amounts to finding which processor gets which data. How this is done is described below.

The Core of the Routine

A number of variables which contain essential information are defined[4]:

I_DO_IO: A logical which is .true. for I/O processors and .false. otherwise.

MY_IO_PE: The number of the I/O processors. This is 0 for all non–I/O processors and equivalent to the processor number otherwise.

MORE_2_DO: A logical used in the main I/O loop in order to show each processor whether or not it has to continue running.

The basic structure of the routine is as follows:

1. The basic variables are defined.

2. The files are opened and PE0 reads the header information[5].

---

[4]The names of the variables are chosen so that reading the following listings should be straightforward.
[5]Actually, PE0 skips the header information because the code reads the basic parameters earlier.

3. The main loop consists of a `DO WHILE` loop. An I/O processor reads data and sends it to the non–I/O processors, or copies it into its own domain, unless the end of a data file is reached.

4. Non–I/O processors wait for particle data and, once this has arrived, they receive it.

5. If an I/O processor reaches the end of its data file it sends or copies the data and then stops the whole process (by setting `MORE_2_DO` to `.false.`).

6. The non–I/O processors have to find out whether or not to expect more data. If all I/O processors have finished their work they must leave the main loop, too. This is the only tricky point so far. One way to do this is to have the I/O processors send the number of particles read to one processor and all the others to get this number and compare it with the total number of particles. However, this would result in a bottleneck for one processor. The scheme here is different. The number of particles on each processor is counted and passed to all processors by means of a special routine called `shmem_fcollect`. Each processor then simply sums up the numbers of particles (read and copied to the processors). If this sum is equal to the total number of particles `MORE_2_DO` is set to `.false.` and the loop is left.

So the basic structure, without the communication, looks like this[6]:

```
C
C I/O procs open files
C
      IF (I_DO_IO) THEN
        file_stream=fopen(filename,"rb")
      END IF
C
C    PE0 skips the header information (HEADER_SIZE_BYTES is
C the size of the header in bytes)
C
      IF (I_DO_IO .and. (MY_IO_PE.eq.0)) THEN
        SEEK_SET_VAL = GET_SEEK_SET()
        i_position = HEADER_SIZE_BYTES
        ierr = FSEEK(file_stream,i_position,SEEK_SET_VAL)
      ENDIF
C
C Ensure that all processors start to read at the same time
C
      CALL barrier()
C
C Read particle data
C
```

---

[6]In the listing, comments describe what is done in the subsequent lines.

```
        MORE_2_DO = .TRUE.
        DO WHILE (MORE_2_DO)
C
C     The I/O processors read the data. i_lines_to_read is the
C maximum size of data they can read. In this case, each
C particle consists of 12 REAL*4 variables.
C
        IF (I_DO_IO) THEN
           IERR = fread(raw_file_data(1,0),4*12,
     &                   i_lines_to_read, file_stream)
           IF (IERR .eq. i_lines_to_read) THEN
C
C The end of the file has not been reached yet.
C Here, some operations will follow (see below).
C
           ELSE
              MORE_2_DO = .FALSE.
C
C The end of the file has been reached.
C Here, some operations will follow (see below).
C
           END IF
        END IF
C
C Ensure that all processors start to communicate at the
C same time
C
        CALL barrier()
C
C Communication here. See below.
C

C
C Check whether or not reading the data is finished:
C Count the particles on each processor...
C
        CALL count_cells_quiet(Nl,N2l,N3l)
        sndint(1) = Nl
        CALL barrier()
C
C ... and communicate the information to all processors.
C npes is the total number of processors,
C
        CALL shmem_fcollect(rcvint,sndint(1),1,0,0,npes,pSync)
```

```
        how_many_particles(0:npes-1) = rcvint(1:npes)
C
C The processors compute the sum and check whether they are
C done.
C
        sum1 = sum(how_many_particles)
        IF (sum1 .eq. Nmax) THEN
          MORE_2_DO = .FALSE.
        END IF
C
C Synchronize the process so that no confusion arises when
C more data is read...
C
        CALL barrier()
```

The basic scheme for the parallel code above is that all processors execute the *same* code. Their processor number is used to deny them access to parts they are not allowed to execute. E.g., in the example above, the logical I_DO_IO is used to have the I/O processors access file operations whereas all other processors do not enter these statements. Because this may result in different execution times for the different parts of the code, and because most parts of the code have to be executed by all processors at the same time, so–called barriers are set. These barriers let a processor wait until all other processors have arrived at it. Then, the whole set of processors continues to execute the subsequent code.

Sending/Receiving Particle Data

As introduced above, the basic principle of which processor owns which particle data is the following: Using a *domain decomposition*, each processor owns all the data of the particles which are in some region in space. Each particle belongs to a processor which holds the particle data of the region it is in.

Thus, each I/O processor has to find out where the particles it has read are located and send them (if necessary) to some other processor. This is done as follows: After each I/O processor has read some fixed number of particles, it calls a subroutine which sorts the particles according to the number of the processor they belong to, and sets up a list with the destinations. This list it then used for the particle communication. The particle communication is done consecutively for the set of I/O processors. Recall that a domain decomposition is used. In principle, an I/O processor could read in data which belongs to *any* processor. This is why the scheme loops over the I/O processors. At any time, only the particle data read in by *one* of the I/O processors is subject to communication because all other I/O processors may be a recipients. The actual I/O processor, that is, the one whose number equals the current index of the loop, checks whether it has to copy data from its read–in array into its data space. All other processors get a copy of the actual I/O processors distribution table, check whether they have to get data, and if they have to, they then get the data[7]. Note that each I/O processor owns its own distribution table

---

[7]The data transfer is done by getting rather than sending because this is more efficient in shmem.

because it has read a disjoint set of particles.

Thus, the particle information is treated as follows:

1. Each I/O processor calls the subroutine `sort_distribution_table` which sets up the lists for the particle exchange.

2. Each I/O processor copies the data it owns into the arrays where they belong.

3. The non–I/O processors get their particle data from the I/O processors by means of the list set up by `sort_distribution_table`.

The complete routine looks like this (some of the above comments and the definitions of some variables are omitted)[8]:

```
      SUBROUTINE readpar(datafile)
C
C Definitions of some variable are omitted
C
      INTEGER MY_IO_PE
      INTEGER file_stream
      INTEGER fopen, fread, fseek
      CHARACTER*7 str_pe
      INTEGER SEEK_SET_VAL, GET_SEEK_SET
      LOGICAL MORE_2_DO
C
C    Note the definitions of the arrays! The locations
C of the arrays are the same on all processors! This is
C necessary for the communication scheme!
C
      POINTER (p_file_data,file_data(12,0:FILE_BLOCK_LINES-1))
      REAL*4 file_data
      REAL*4 raw_file_data(12,0:FILE_BLOCK_LINES-1)
      POINTER (p_remote_file_data,
     &         remote_file_data(12,0:FILE_BLOCK_LINES-1))
      REAL*4 remote_file_data
      POINTER (p_distribution_table,
     &         distribution_table(2,0:npes-1))
      p_file_data=LOC(sndbuf)
      p_remote_file_data=LOC(rcvbuf)
      p_distribution_table=LOC(rcvint)
      p_file_data=LOC(sndbuf)
      p_io_send_flag=LOC(sndint(1))
```

---

[8] The reader who is not interested in the details of the parallel code may skip this listing and proceed to the next Chapter.

```fortran
      INTEGER distribution_table
      INTEGER remote_distribution_table(2,0:npes-1)
      INTEGER Nl,N2l,N3l,sum1
C
C Define the names of the input files
C
      WRITE(str_pe,'(i4)')MY_IO_RANK
      startpos_me=SCAN(str_pe,'0123456789')
      longfile = dirname(1:lnblnk(dirname))//'/data/'
     &       //datafile//"."//
     &         str_pe(startpos_me:LEN_TRIM(str_pe))
C
C Initialize scaling factors for file data
C
      grow=REAL(L)
      vscale=grow
C
C    Construct particle distribution function as
C function of PE number
C
      MY_IO_PE=(mype/io_proc_skip)*io_proc_skip
C
      IF (I_DO_IO) THEN
        file_stream=fopen(longfile,"rb")
      END IF
C
      IF (I_DO_IO .and. (MY_IO_PE.eq.0)) THEN
        SEEK_SET_VAL=GET_SEEK_SET()
        i_position=HEADER_SIZE_BYTES
        ierr=FSEEK(file_stream,i_position,SEEK_SET_VAL)
      ENDIF
      CALL barrier()
C
C Read particle data
C
      MORE_2_DO = .TRUE.
      i_lines_to_read = FILE_BLOCK_LINES
      DO WHILE (MORE_2_DO)
        distribution_table = 0
C
C    Read the data. The data is properly scaled and copied
C into the array file_data which has the same location on
C each processor. After that, the distribution table is set
C up by calling the appropriate subroutine.
```

118

```fortran
C
      IF (I_DO_IO) THEN
        IERR = fread(raw_file_data(1,0),4*12,
     &                 i_lines_to_read,file_stream)
        IF (IERR .eq. i_lines_to_read) THEN
          DO i = 0, i_lines_to_read-1
            file_data(1,i)=raw_file_data(1,i)
            file_data(2:4,i)=raw_file_data(2:4,i)*grow+1.
            file_data(5:7,i)=raw_file_data(5:7,i)*vscale
            file_data(8,i)=0.0
            file_data(9,i)=0.0
            file_data(10,i)=0.
            file_data(11,i)=0.0
            file_data(12,i)=raw_file_data(8,i)
          END DO
          CALL sort_distribution_table(file_data,
     &               distribution_table, i_lines_to_read)
        ELSE
          i_end_lines = IERR
          MORE_2_DO = .FALSE.
          DO i = 0, i_end_lines-1
            file_data(1,i)=raw_file_data(1,i)
            file_data(2:4,i)=raw_file_data(2:4,i)*grow+1.
            file_data(5:7,i)=raw_file_data(5:7,i)*vscale
            file_data(8,i)=0.0
            file_data(9,i)=0.0
            file_data(10,i)=0.
            file_data(11,i)=0.0
            file_data(12,i)=raw_file_data(8,i)
          END DO
          CALL sort_distribution_table(file_data,
     &               distribution_table, i_end_lines)
        END IF
      END IF
C
      CALL barrier()
C
C    Communicate the data: This is done by looping over
C the number of I/O processors (outer DO loop). Each I/O
C processor has to copy data it has to store from
C its own read-in array into some intermediate array
C (IF statements). All other processors have to receive
C data over the network (ELSE statement). Note that only
C one I/O processor enters the IF statement. The loop
```

```
C then ensures that the I/O processors send their data
C consecutively.
C    i_size specifies the number of particles a processor
C is supposed to get
C    i_start gives the position of the first particle it
C will get in the read in-array
C    All processors except the current I/O processor
C may have to receive data. In order to check this, they
C grab a copy of the distribution table from the current
C I/O processor. If it has to get data this is communicated
C by means of shmem_get4.
C    After the communication phase the particles are
C inserted into the particle lists of each individual
C processor (using a separate subroutine called
C insert_particle).
C
      DO i_current_io_rank=0,IO_PROCS-1
        IF ((I_DO_IO) .and.
     &       (i_current_io_rank.eq.MY_IO_RANK)) THEN
          i_size=distribution_table(2,mype)
          i_start=distribution_table(1,mype)
          IF (i_size.gt.0) THEN
            remote_file_data(:,0:i_size-1)=file_data(:,
     &             i_start:i_start+i_size-1)
          END IF
        ELSE
          i_remote_pe=i_current_io_rank*io_proc_skip
          CALL shmem_get(remote_distribution_table(1,0),
     &                   distribution_table(1,0),2*npes,
     &                   i_remote_pe)
          i_start=remote_distribution_table(1,mype)
          i_size=remote_distribution_table(2,mype)
          IF (i_size.gt.0) THEN
            CALL shmem_get4(remote_file_data(1,0),
     &                      file_data(1,i_start),
     &                      12*i_size,i_remote_pe)
          END IF
        ENDIF
        DO i=0, i_size-1
          CALL insert_particle(remote_file_data(1,i))
        END DO
        CALL barrier()
      END DO
C
```

```
          CALL count_cells_quiet(Nl,N2l,N3l)
          sndint(1)=Nl
          CALL barrier()
          CALL shmem_fcollect(rcvint,sndint(1),1,0,0,
     &                        npes,pSync)
          how_many_particles(0:npes-1)=rcvint(1:npes)
          sum1 = sum(how_many_particles)
          IF (sum1 .eq. Nmax) THEN
            MORE_2_DO = .FALSE.
          END IF
          CALL barrier()
        END DO
C
C Close the files
C
      IF(I_DO_IO) THEN
        CALL fclose(file_stream)
      END IF
      RETURN
      END
```

Bibliography

[1] Couchman H.M.P., ApJ **368**, L23 (1991)

[2] MacFarland T.J., Couchman H.M.P., Pearce F.R., Pichlmaier J., submitted to New Astronomy, astro-ph/9805096

[3] Pearce F.R., Couchman H.M.P., New Ast **2**, 411 (1997)

[4] Peebles P.J.E., The Large–Scale Structure of the Universe, Princeton University Press (1980)

Chapter 9
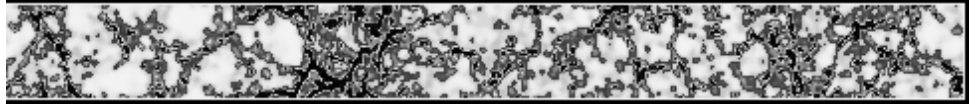
Summary

In this work, large N–body simulations were used to investigate different aspects of of the formation and evolution of Large–Scale Structure (LSS). These aspects may be separated into two main parts, namely the distribution of matter on very large scales, and the formation, evolution, and properties of galaxy clusters.

On the largest scales, the distribution of mass forms a complicated network which qualitatively is very similar to the pattern which can be seen in galaxy catalogs. There, galaxies are found preferentially in clusters, filaments, and sheets around large region with no or almost no galaxies. It is not clear, whether the predominant component of LSS in galaxies is sheets or filaments. In the simulations, the situation is similar if adaptively smoothed two–dimensional representations of slices through the distribution of the Dark Matter are shown (compare e.g. fig. A.4). Around big voids, clusters, filaments, and sheets appear. Of course, in the simulation the connectedness of structure is more pronounced. All the haloes are interconnected by a network of Dark Matter of low density. Even in the voids, small haloes can be found.

Three–dimensional representations of the adaptively smoothed density field reveal interesting properties of LSS. In this work, an overdensity threshold was applied to the field and the properties of mass above the threshold were investigated. For low overdensities ($\delta < 2$) most of the overdense mass can be found in a single object which extends all across the universe – an effect known as percolation. The occupied volume, however, is only a few percent. Apart from the biggest object, a plethora of small spherical objects exists. If the threshold is increased, the biggest object starts to crumble and eventually ($\delta \approx 4$) breaks up into many smaller objects, that is percolation ceases. There are small differences between the cosmological models. The percolation thresholds and the mass and volume fractions differ for different models. These differences can be understood in terms of the power spectra of the models and their dynamical history. Visual representations give the impression that the biggest object is a very complicated conglomerate of filaments (see e.g. fig. A.10). There has been an industry trying to characterize LSS by inventing measures for its topology, geometry, and connectedness. In this work, the Minkowski functionals were computed for the density field. Further

quantities were derived which give typical length scales. The amount of additional information obtained, however, was rather poor. In particular, the size of the mesh used here was too small. Some elements of LSS appear to have sizes of only a couple mesh cells or smaller. Basically, the Minkowski functionals confirm what visual impressions of the biggest object already show. The derived quantities, like the ratio of the volume and the surface of the biggest object, suggest that on average one dimension of this object is much larger than the other two dimensions. The biggest object appears to consist of filaments and no sheets. For large overdensity thresholds ($\delta = 180$), the biggest object is identical with the biggest cluster and is nearly spherical.

Clusters of galaxies stand out in the LSS. They can be spotted easily in two–dimensional representations and for high overdensities, they are by far the most massive objects in the density field. It is natural to investigate LSS from the perspective of cluster formation. This was done in this work by reconstructing the formation process of galaxy clusters and relating it to the surrounding LSS. Clusters form by the accretion of matter. In the CDM universes discussed here, this process has no resemblance with a spherical collapse. Rather, smaller objects merge to form larger objects. If the cluster center is defined as the barycenter of the most massive progenitor, objects fall into the cluster from a few preferred directions. These directions are constant in time and correspond to the locations of filaments and sheets. Although sheets do not appear in the investigation of the three–dimensional smoothed density field, a few of these objects can be seen if LSS is viewed from the center of a massive cluster. The overdensity of the sheets is low. This fact may explain why they are only found this way.

There is another reason why clusters of galaxies are special objects. Their present day masses are very big so matter had to be assembled from a large region of space in the early Universe. Speaking in terms of the smoothed initial density field, clusters must have formed from high peaks. This was checked in this work and indeed the majority of clusters can be associated with a high peak. More massive clusters tend to correspond to higher peaks although there is some scatter in this relation. The formation redshifts of clusters are small (there is a dependence on Ω_0 here). That means that for instance the peculiar velocities should not deviate much from the predictions of Linear Theory. In particular, the velocities of clusters should correspond to the velocities of their associated peaks. It turned out that the latter is indeed the case if the velocities or the peaks in the initial density are compared with the velocities of the particles in the initial conditions which end up in the cluster at present time. In addition, the velocities of the peaks agree very well with the predictions of Linear Theory if the actual realization of the power spectrum used in the simulations is taken. The choice of the filter which is used in the smoothing does not change these results. However, the velocities of the clusters at the present time are about 40% larger than the extrapolated linear velocities. If these deviations are investigated on a cluster by cluster basis it turns out that for clusters which are themselves part of superclusters, that is which have another cluster close by, the deviations are large.

The largest sample of simulated galaxy clusters ever was obtained from the Hubble Volume Simulations which were done as part of this work. These simulations follow the evolution of 10^9 particles in regions which enclose significant fractions of the whole observable Universe. These cluster samples were used to investigate a couple of points which could not be addressed that accurately before. Recently, observations of massive clusters at a redshift of $z \approx 0.8$ have added a new aspect to the debate about the density parameter Ω_0. In a Universe with $\Omega_0 = 1$

clusters form so late that one could not expect to find massive clusters at $z \approx 0.8$. The simulation dumps at $z = 0.78$ from the two Hubble Volume Simulations were used to look for the most massive objects which had formed by that time. Despite the uncertainties in the observations of massive clusters at $z \approx 0.8$ and despite the small sample currently available, it can be concluded that the $\Omega_0 = 1$ model fails to form such objects. The most massive clusters have masses which are too small, and their number densities are far too low to be able to account for the observations. The uncertainties in the observations is reflected by the most massive cluster which is far too massive even for the flat low Ω_0 Hubble Volume Simulation. Clearly, for a more detailed investigation, the observational sample has to grow.

As already indicated above, clusters themselves are clustered and not distributed homogeneously. A means to describe this is the two–point correlation function $\xi(r)$. Conventionally, the correlation function is investigated as a function of the abundance of clusters which is usually expressed via the mean separation of the sample, d_c. This convention arose from the way observationally complete samples are compiled. It was well known that the correlation length, r_0, which is defined via $\xi(r_0) = 1$, depends on the cluster abundance. Sparser cluster samples are more strongly clustered than less sparse samples. Thus, the amplitude of $\xi(r)$ is larger for the sparse samples which is reflected in the increase in r_0. However, the relation between d_c and r_0 has been controversial for decades now. A linear, that is fractal–like scaling was proposed but new and large observational samples of clusters like the one from the APM galaxy catalog do not support this scaling. The cluster samples from the Hubble Volume Simulations show that r_0 does not increase linearly with d_c. The correlation function is well described by the analytical theory developed by Mo & White which expresses $\xi(r)$ of the clusters as $\xi(r)$ of the Dark Matter times a bias factor. Although the correlation lengths obtained by fitting the Mo & White function are somewhat too large, the qualitative trend agrees very well. Again, the flat low density model agrees better with the observational data.

Clearly, the work presented here shows how N–body simulations can be used to refine theories and to investigate them in more and more detail as the simulation techniques get more and more sophisticated. However, in a sense the times of very big Dark Matter only simulations have come to an end because with the Hubble Volume Simulations the largest possible scales have been reached. From now on, it will be necessary to add missing physics, that is baryons, in the simulations to learn more about the formation and evolution of galaxies. Although analytical and phenomenological (or semi–analytical) models of galaxy formation have been refining the knowledge of how galaxies form, the understanding of the processes contributing in some way or another is still in its infancy. Clearly, in the future, N–body simulations which include gas physics will be needed to learn more about the physics that governs the formation of galaxies or clusters of galaxies. The computer will always be a laboratory for theoreticians to take the physical recipes and see what they lead to.

Danksagung

There's a time when life is full of meaning
That's the time that I'm looking forward to.

(from "Something To Do" by Yo La Tengo)

I coded and ran my first N–body simulation in 1985 on a C64 "homecomputer". The galaxy I wanted to simulate consisted of 21 (star) particles and had no Dark Matter halo at all. It didn't work. Ten years later Simon White provided me with the unique opportunity to participate in coding, running, and analyzing some of the largest and certainly most sophisticated cosmological simulations to–date. In addition, he encouraged me to bring in my own ideas and to work on projects independently. Thank you very much, Simon.

I have benefitted a lot from the many discussions I had with the members of the Large–Scale Structure crowd at the MPA. In particular, I'd like to thank Matthias "Hello Miss!" Bartelmann for being a big help during the early stages of my work, for being a discussion partner and tutor of lensing issues, and for sharing some bizarre and thus non–German humor. I opologize to Achim Weiss for having him exposed to the Dead Parrot Sketch about a zillion times.

My office mates, Volker and Martin, have shared with me the the daily routine of work. I would like to thank them for providing such a nice atmosphere and for bearing my occasional Thomas Bernhard impersonations. I sink zis was reelly krushal.

Participating in the Virgo Consortium was a unique experience, too. This work would not have been possible in its current form without the various contributions from those Virgoans who bothered to contribute to the project. In particular, I would like to thank Adrian Jenkins for being a close partner during the course of this work. Credits are due to Carlos Frenk for his enthusiasm which usually was beyond all reasonable limits, to Frazer Pearce for all his efforts he put into the old code and for resonating when I was in my complaints mode, and, of course, to all remaining Virgoans for allowing me to put their names on our papers although their contributions to the project essentially come down to zero.

Without the general incompetence at the RZG and its prevailing unwillingness to deal with the user's demands it would have been much easier to get the work done. However, Gabriele Mahl and Ingeborg Weidl are exceptions to this rule and deserve credits for their efforts to deal with the Hubble Volume Simulations.

crEdits Are also due to all those in–duh!–Viduals who trEated me as theIr peRsonal helpdEsk in case of comPuter pRoblems, thUs preveNting me from Getting too absorbeD by the stuff I was actually supposed to do (names can Be found by extractIng and sorting the capital lettErs in this paraGraph).

During the course of this work, I made many new friends and I'd like to thank them all. My German class (Adi, Antonaldo, Eugene, Itziar, Marat, and Ravi) has allowed me to elaborate on why sitting at the coffee table for 45 minutes after lunch is a complete waste of time. Thank you also Hans, Margit und Alina, Alex, and Rachel.

But in particular I'd like to thank two persons whom I met and who became friends while I was working on this thesis. Antonaldo Diaferio has taught me a lot about the importance of what really matters in life. Mille grazie, Antonaldo, I look forward to all future dinners and occasions to meet you. Tom MacFarland not only contributed a lot to various projects which

are discussed in this thesis, but also made me think about many things outside academia and made me enjoy life over a glass of wine or n (where n may be any integer). Tom, I still think that once I subscribe the *Economist* you'll receive a cheque from them. But I really hope we will be able to share a good bottle of wine in 2008 and laugh about this.

I know this is not the Oscar awards but nevertheless I want to thank my parents for their support und understanding while I was working on this.

Last but not least I would like to thank a very special person for being there when I needed her. Susanna, you have made quite a bit of this possible, without you I would have never made it. This is why I dedicate this work to you. Thank so very much!

Curriculum Vitae

Persönliche Daten: Jörg Colberg
geboren am 15.02.1968 in Wilhelmshaven
ledig

Schulbesuch:

Aug. 1974 – Juni 1978	Grundschule in Wilhelmshaven
Aug. 1978 – Juni 1980	Orientierungsstufe in Wilhelmshaven
Aug. 1980 – Juni 1987	Max–Planck–Gymnasium, Wilhelmshaven
	Abschluß: Abitur

Militärdienst:

Juli 1987 – Juni 1989	Soldat auf Zeit (2 Jahre)

Berufsausbildung:

Okt. 1989 – Dez. 1994	Rheinische Friedrich–Wilhelms–Universität Bonn
	Studium: Physik, Astronomie
	Abschluß: Diplom–Physiker
Jan. 1995 – März 1995	Ergänzende Arbeiten am Thema der Diplomarbeit
Sep. 1995 – Herbst 1998	Max–Planck–Institut für Astrophysik/
	Ludwig–Maximilians–Universität München
	Promotionsstudium: Astrophysik
	Abschluß: Dr. rer. nat.
	Thema der Arbeit: "*Parallel Supercomputer Simulations of Cosmic Evolution*", in Zusammenarbeit mit dem Virgo Supercomputing Consortium (GB/D/CAN)

Tätigkeiten während des Studiums:

Juli 1992 – Sep. 1993	Studentische Hilfskraft: Optische Interferometrie und Digitale Bildverarbeitung (Max–Planck–Institut für Radioastronomie)
Okt. 1993 – Feb. 1995	Übungsgruppenleiter (Anfängerkurse)
Okt. 1992 – Feb. 1994	tätig in der Fachschaft Physik

Colour panels

The Simulation Sets
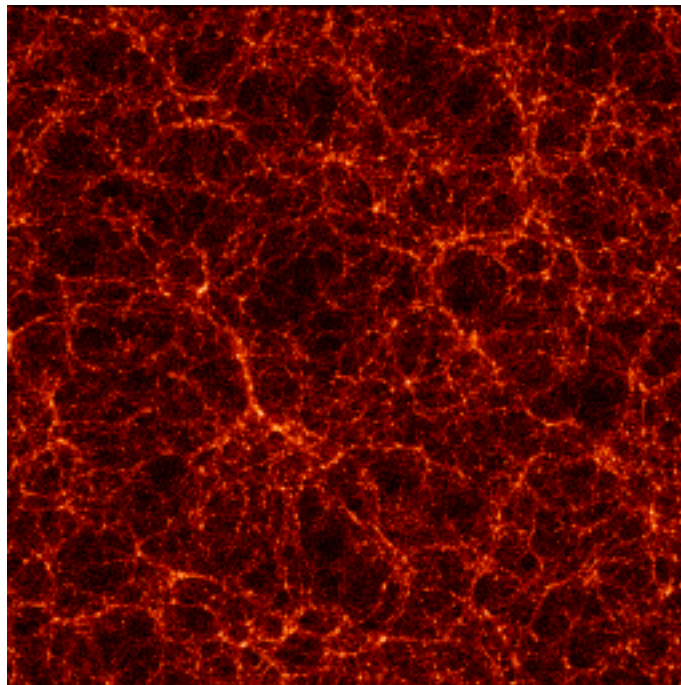
Figure A.1.: A slice through the SCDM Virgo simulation. The particles are binned up on a mesh. The colour scale is logarithmic.
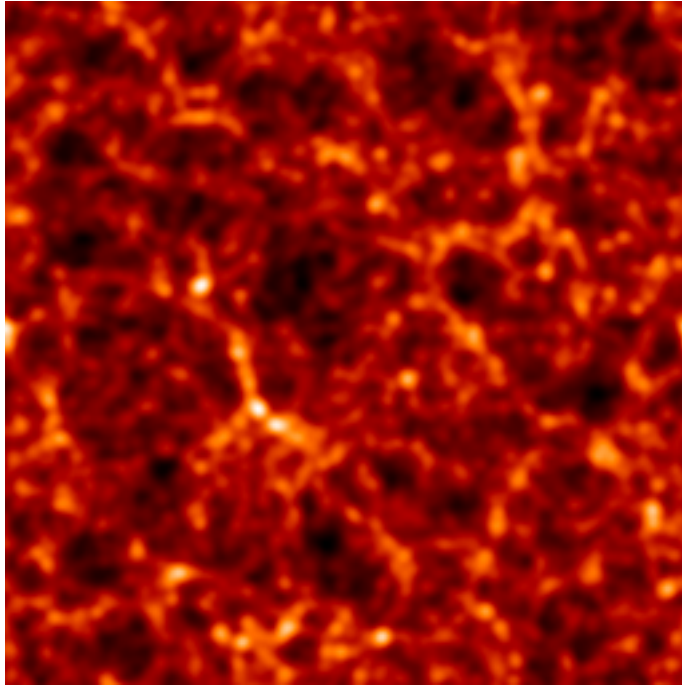
Figure A.2.: The same slice through the SCDM Virgo simulation smoothed with a Gaussian (kernel size 2.5 Mpc/h).
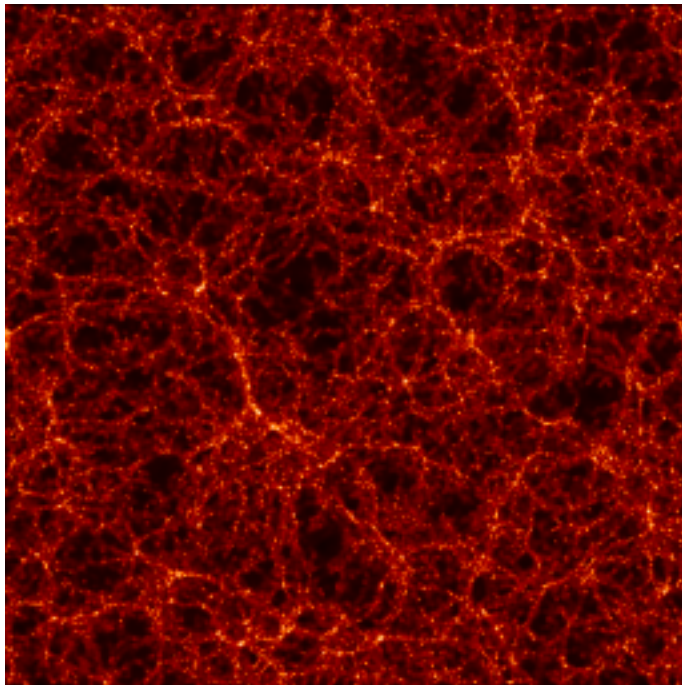
Figure A.3.: The same slice through the SCDM Virgo simulation smoothed with the adaptive smoothing technique.

II
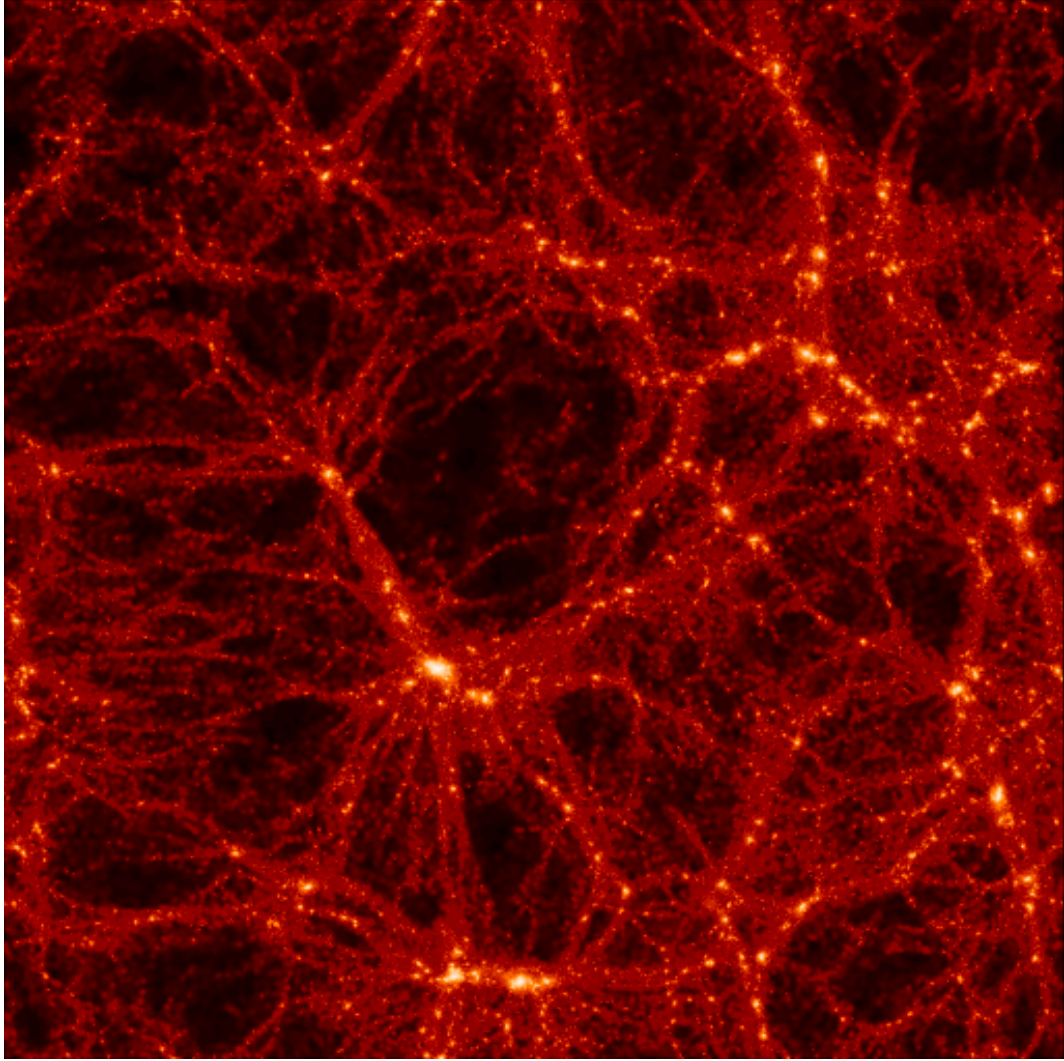
Figure A.4.: A slice of thickness 8.5 Mpc/h through the τCDM GIF simulation at $z = 0$.
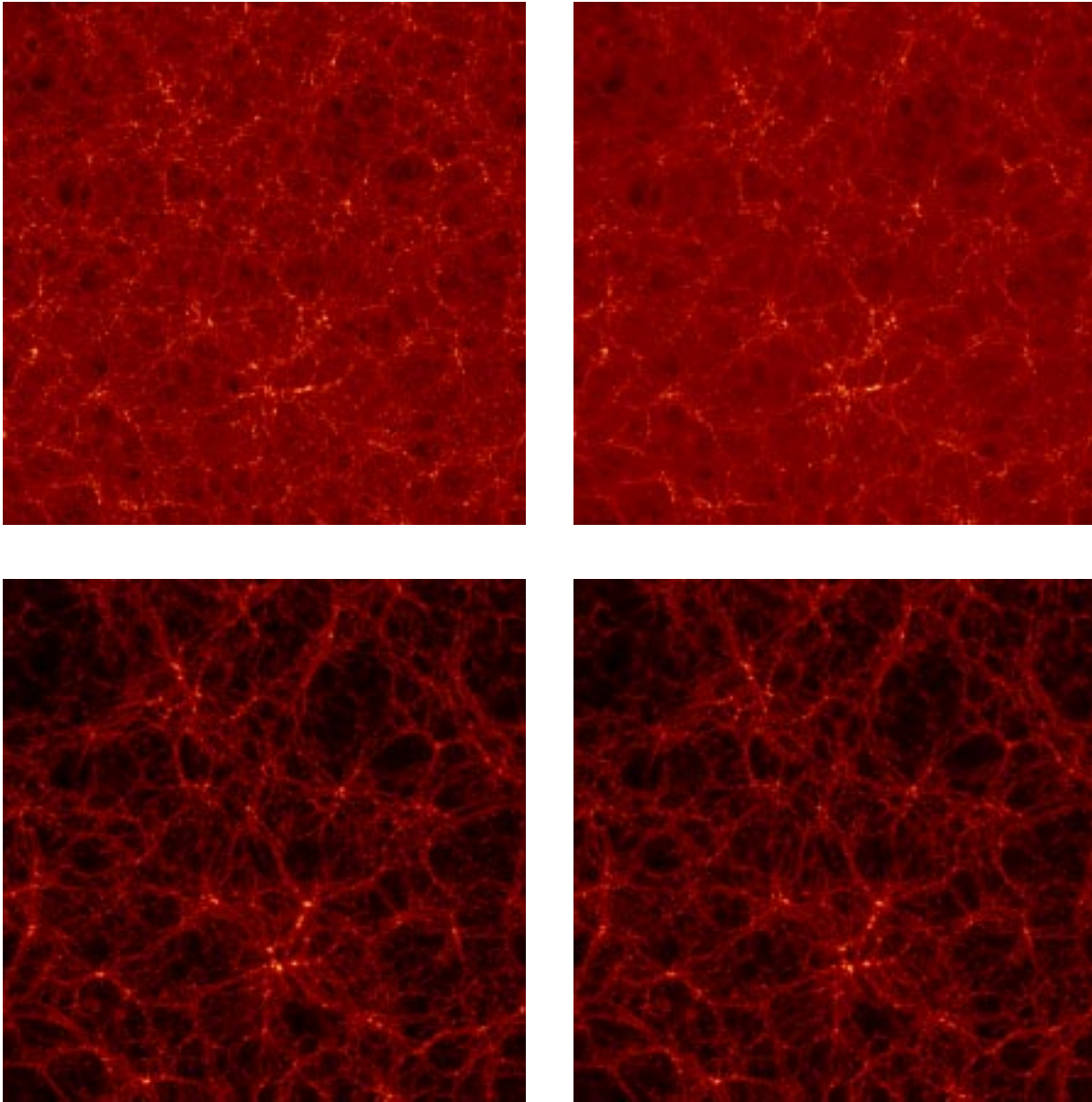
Figure A.5.: Slice of thickness 1/10th of the box size through the four Virgo simulation at $z = 0$: SCDM (top left), τCDM (top right), ΛCDM (bottom left), and OCDM (bottom right).
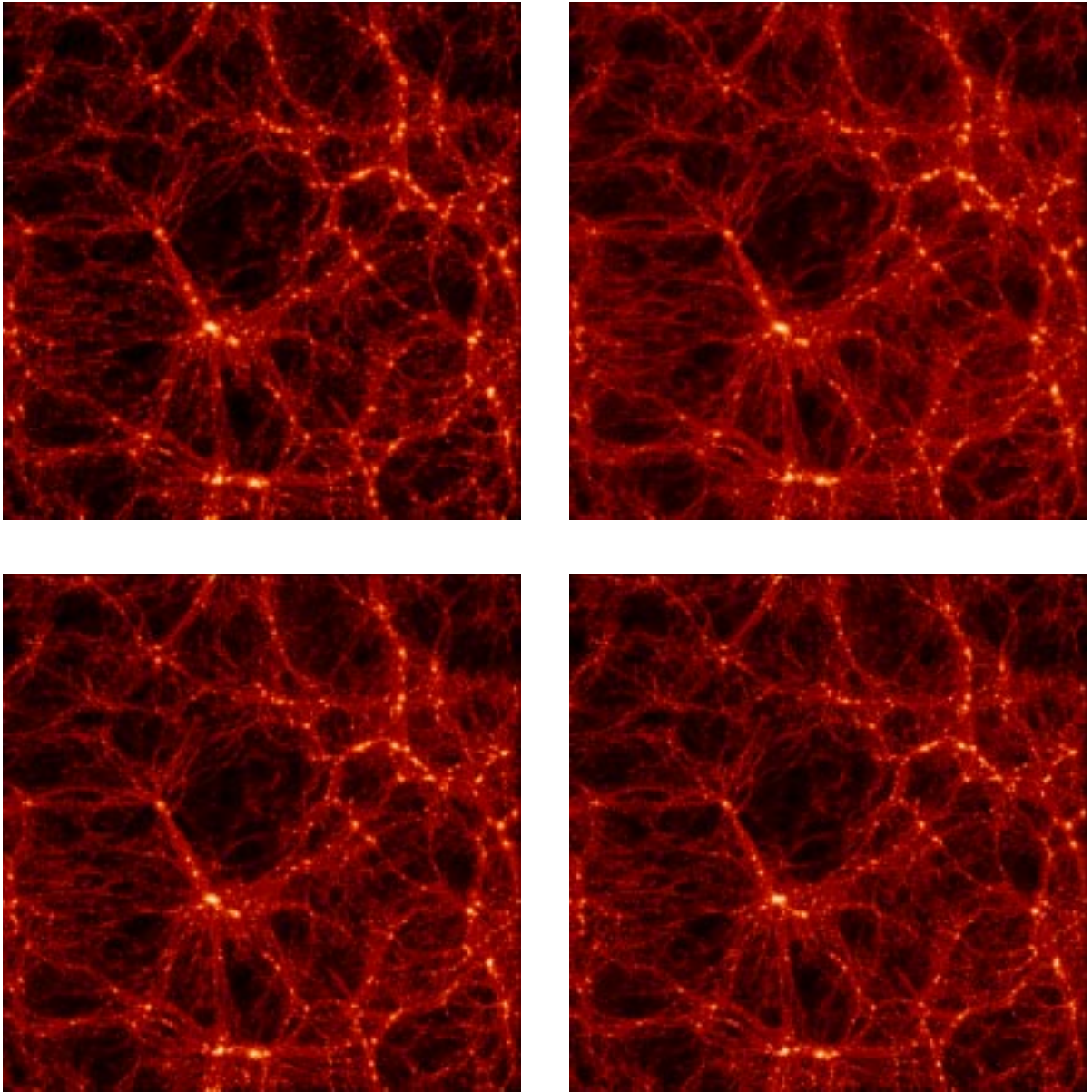
Figure A.6.: Slice of thickness 1/10th of the box size through the four GIF simulation at $z = 0$: SCDM (top left), τCDM (top right), ΛCDM (bottom left), and OCDM (bottom right.
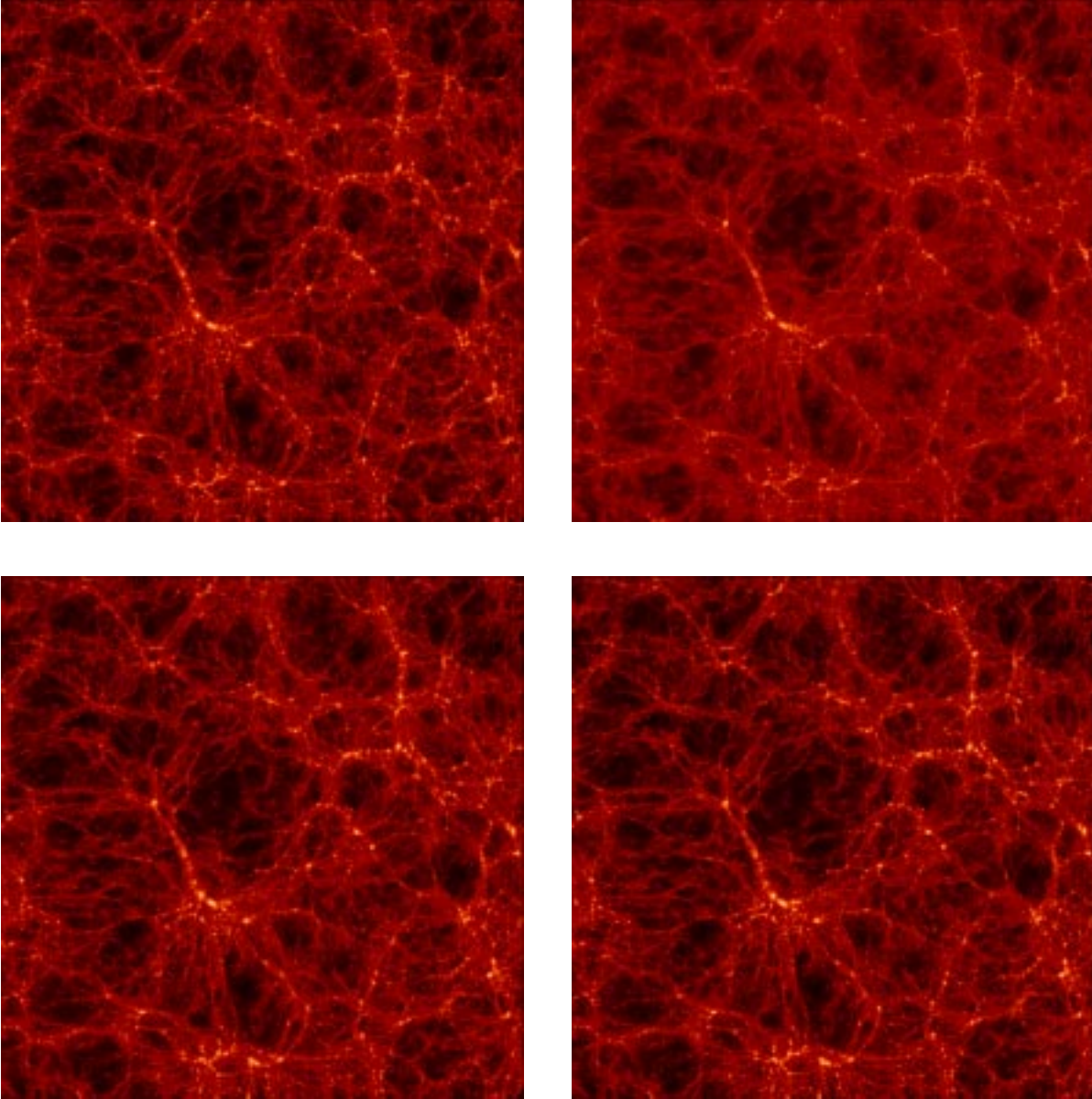
Figure A.7.: Slice of thickness 1/10th of the box size through the four GIF simulation at $z = 1$: SCDM (top left), τCDM (top right), ΛCDM (bottom left), and OCDM (bottom right).
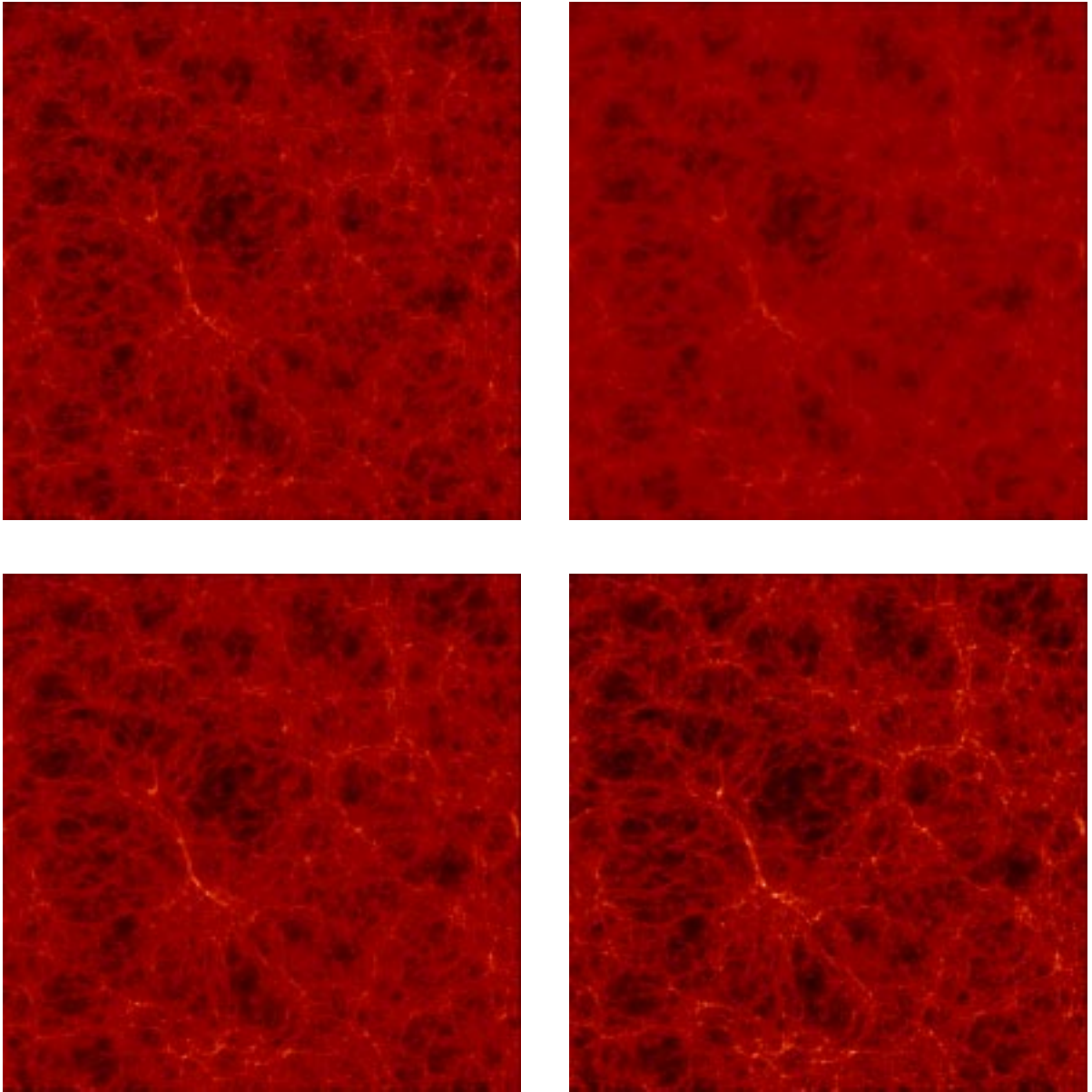
Figure A.8.: Slice of thickness 1/10th of the box size through the four GIF simulation at $z = 3$: SCDM (top left), τCDM (top right), ΛCDM (bottom left), and OCDM (bottom right).

The Distribution of Mass
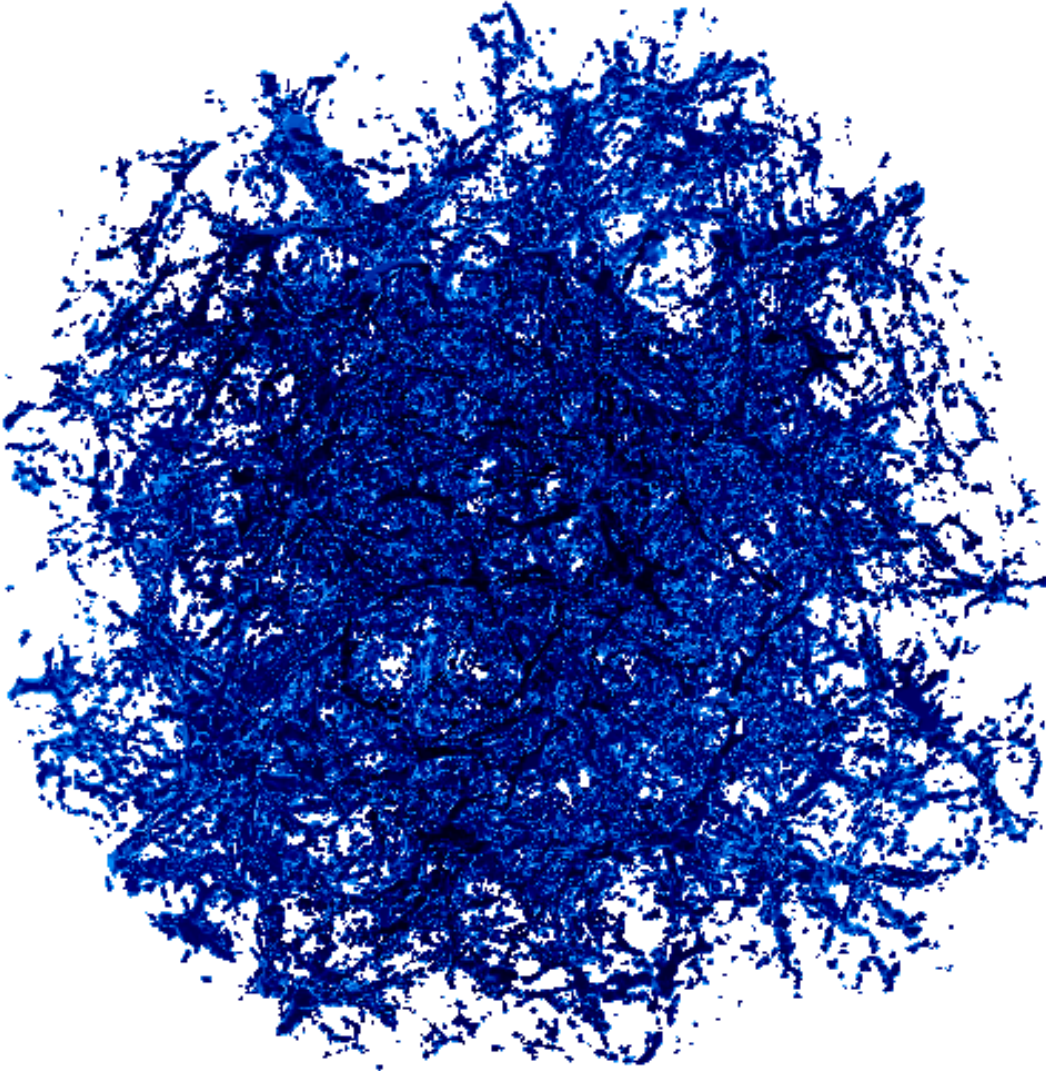
Figure A.9.: An isooverdensity contour view of the complete τCDM box at an overdensity of 2. Shown are all objects above the threshold.
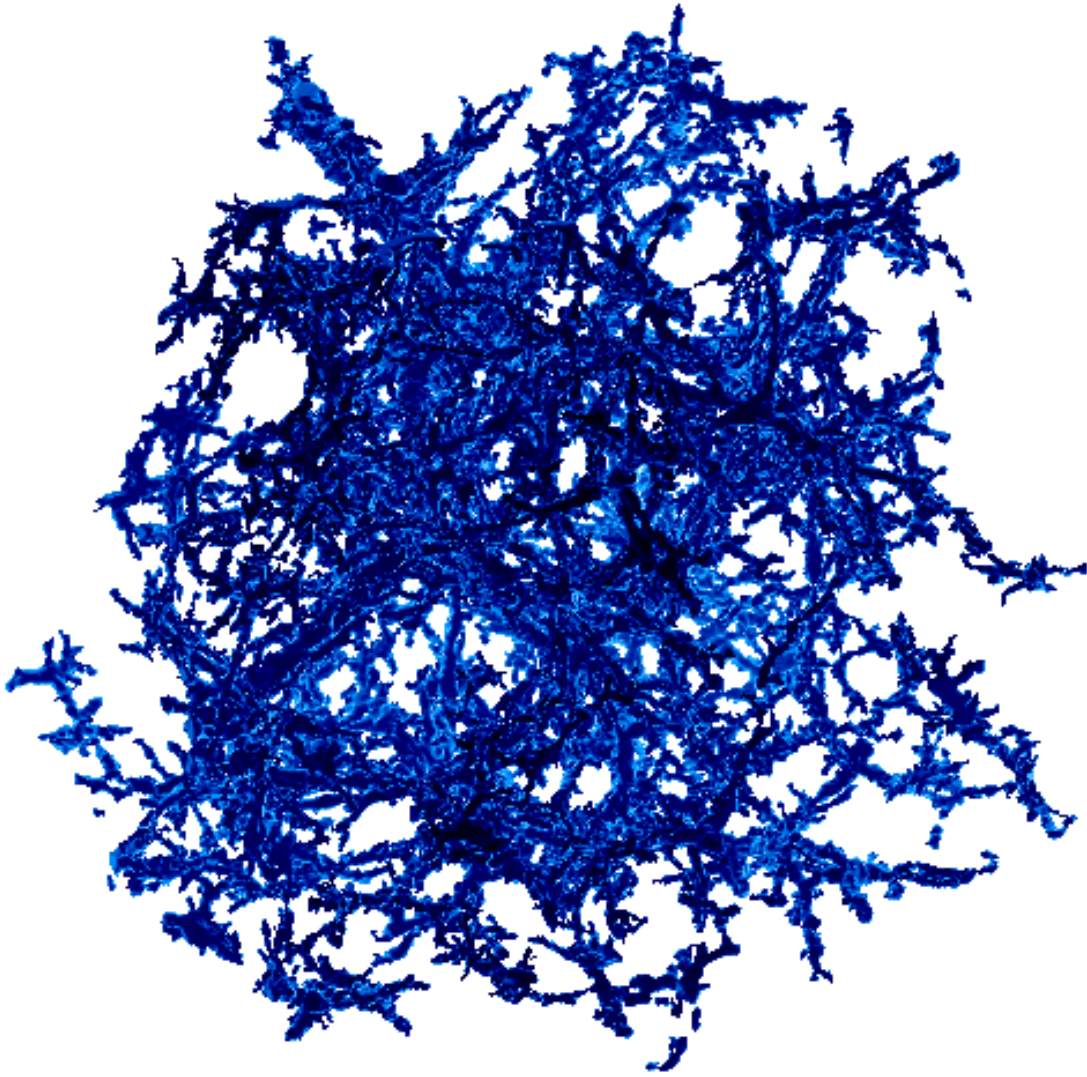
Figure A.10.: An isooverdensity contour view of the complete τCDM box at an overdensity of 2, shown is only the biggest object. This object contains roughly 50% of the mass and occupies around 2.5% of the total volume.
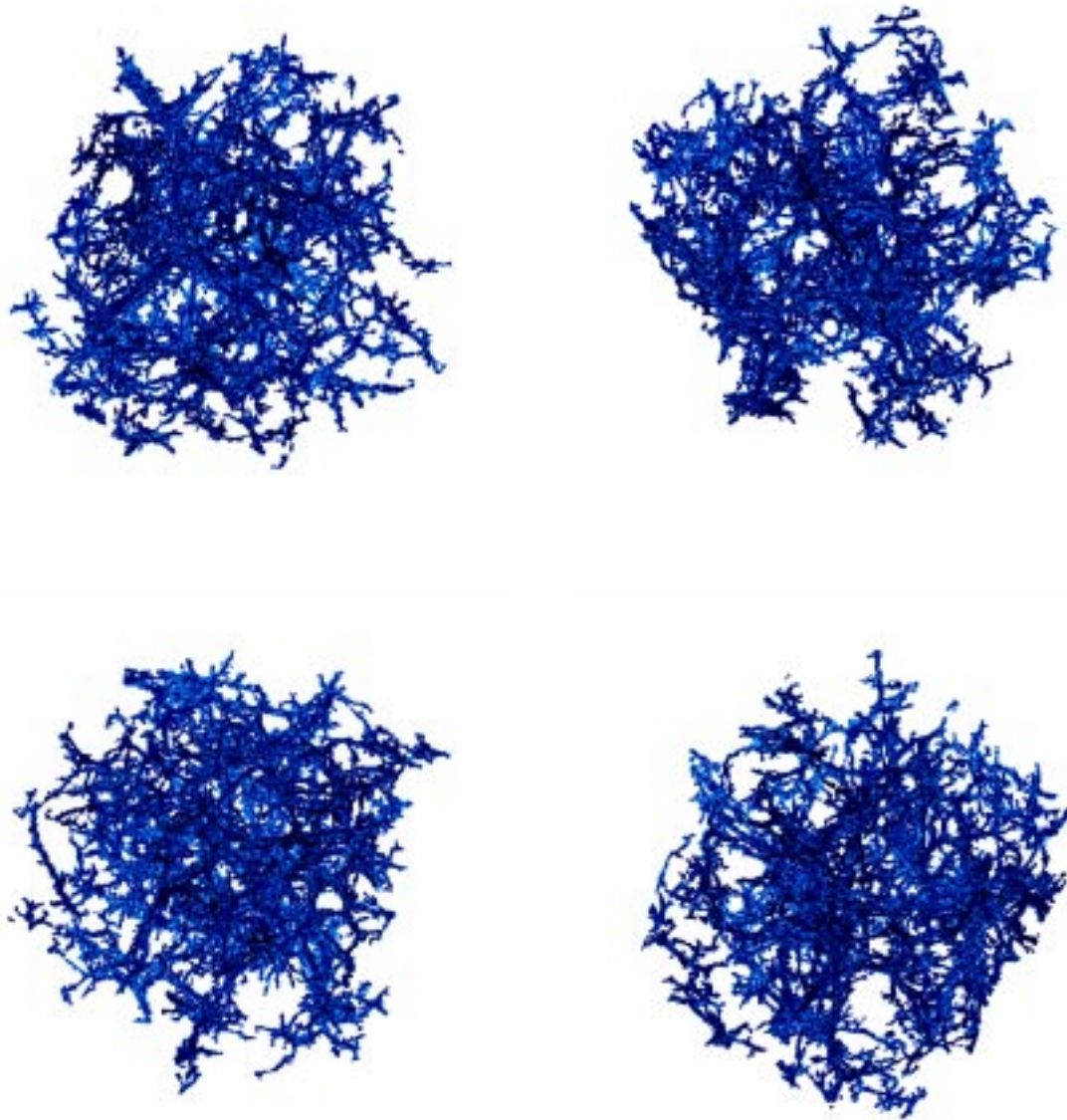
Figure A.11.: The same isooverdensity contour view of the biggest object as in figure A.10, shown from different angles.
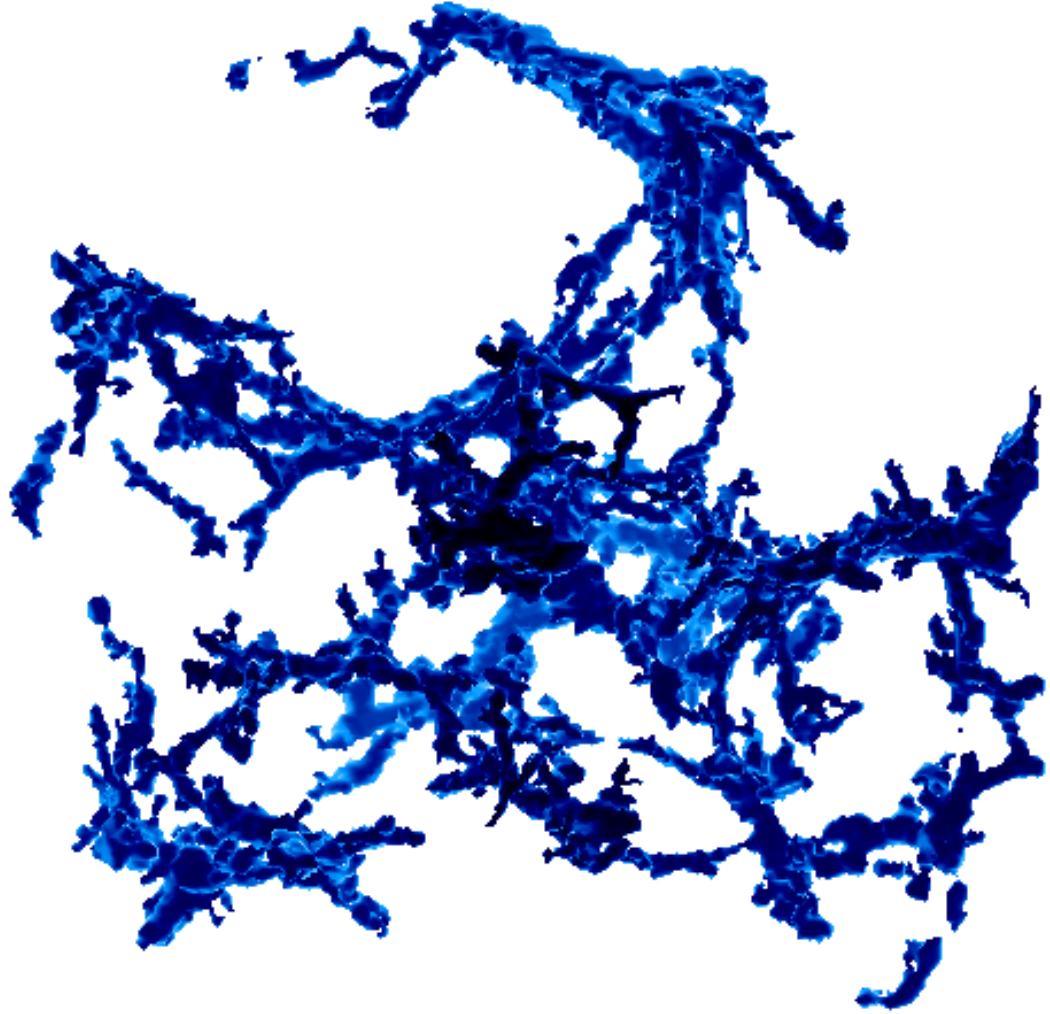
Figure A.12.: An isooverdensity contour view of an eighth of the τCDM box at an overdensity of 2, shown is a part the largest object. The isolated pieces are joined to the object due to periodic boundaries.
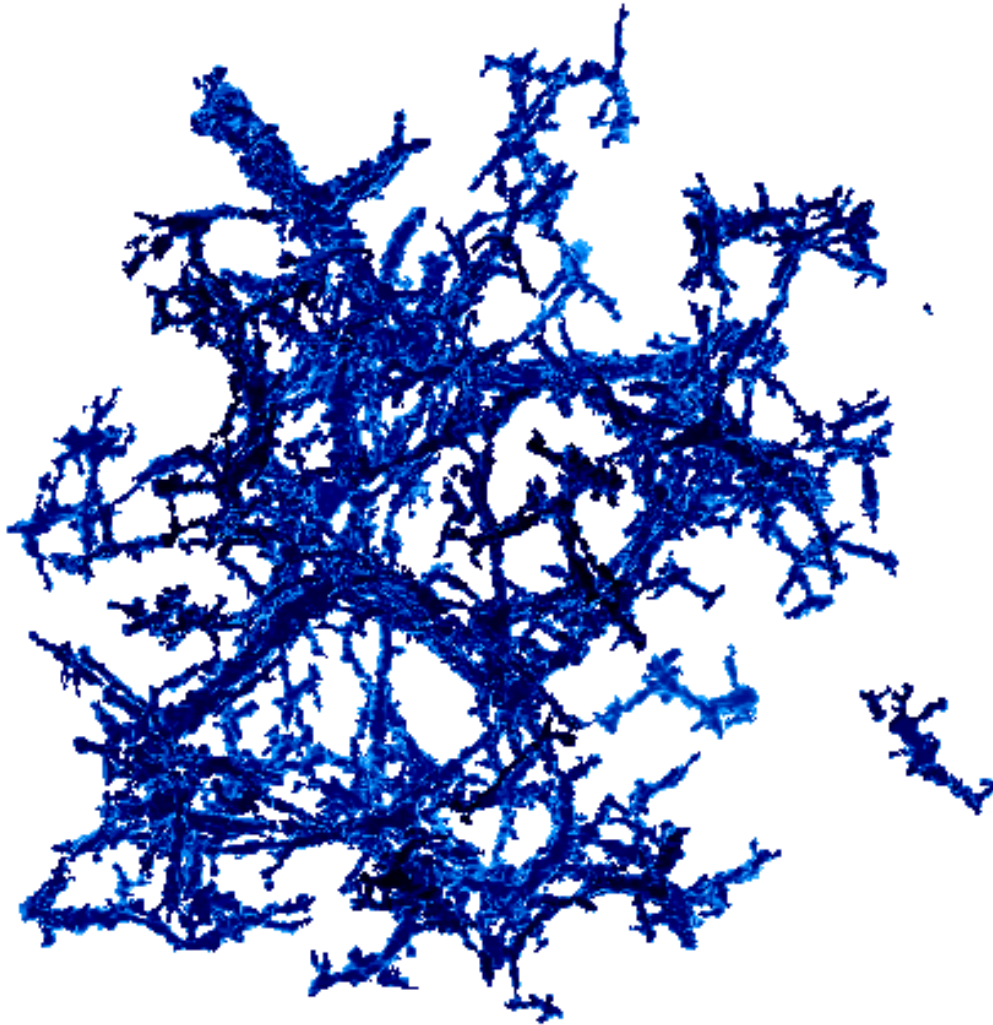
Figure A.13.: An isooverdensity contour view of the complete τCDM box at an overdensity of 3, shown is again the largest object. It contains around 30% of the mass and occupies around 1% of the volume. The isolated piece at the right edge is in fact joined to the object due to periodic boundaries.
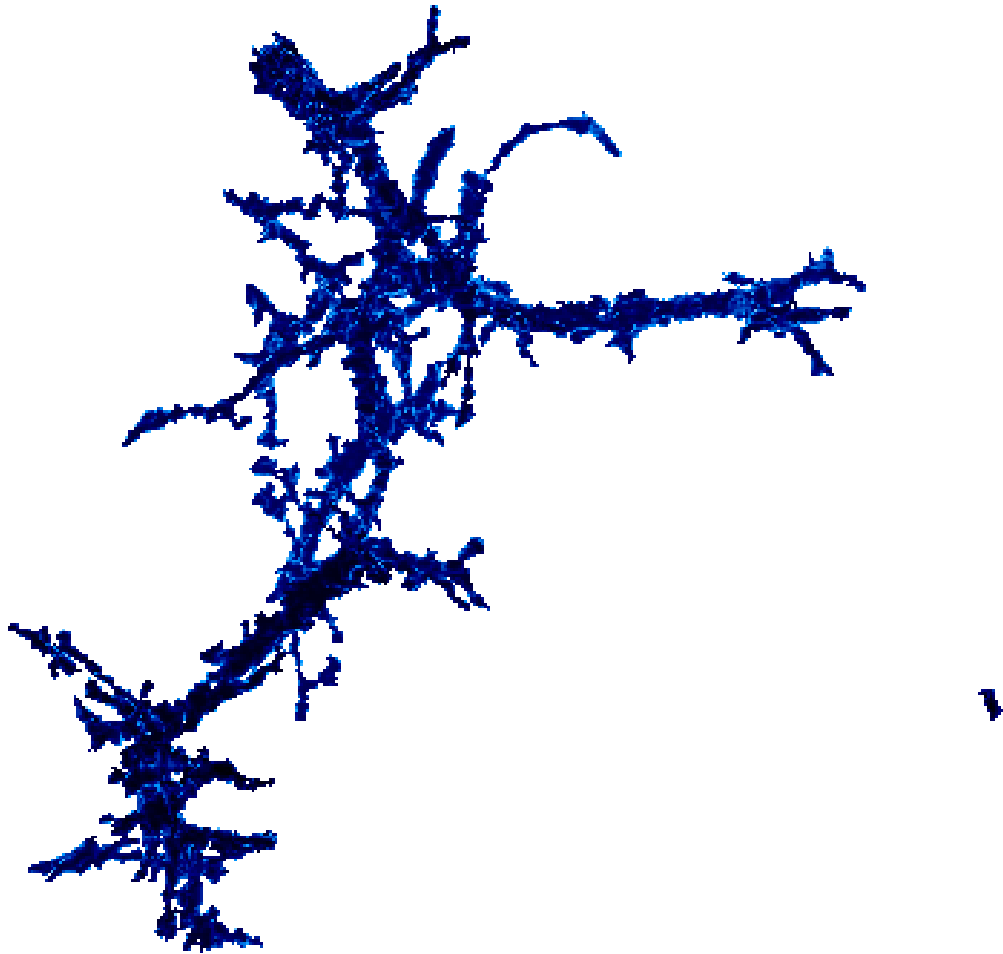
Figure A.14.: The largest object in the τCDM box at an isooverdensity contour of 4. Due to periodic boundaries the small piece at the right edge is joined with the left side of the object. It is not clear whether there is still percolation. The fraction of the mass in this object is now about 8% and it occupies less than 1% of the volume.

Peculiar Velocities of Galaxy Clusters
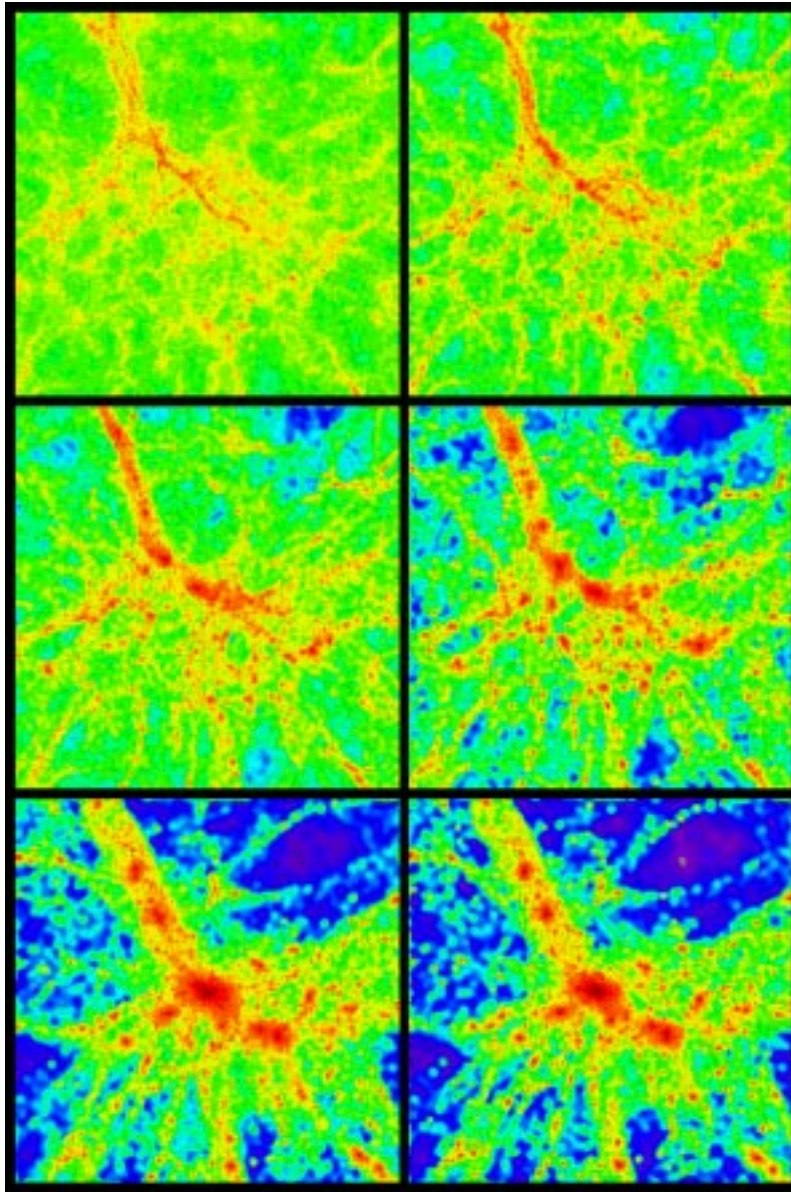
Figure A.15.: The formation process of a cluster from the τCDM (leftmost panel) and the ΛCDM (rightmost panel) simulation at $z = 2$ (top), $z = 1$ (middle), and $z = 0$ (bottom). The colour tables are the same for the two cosmologies.

The Hubble Volume Simulations
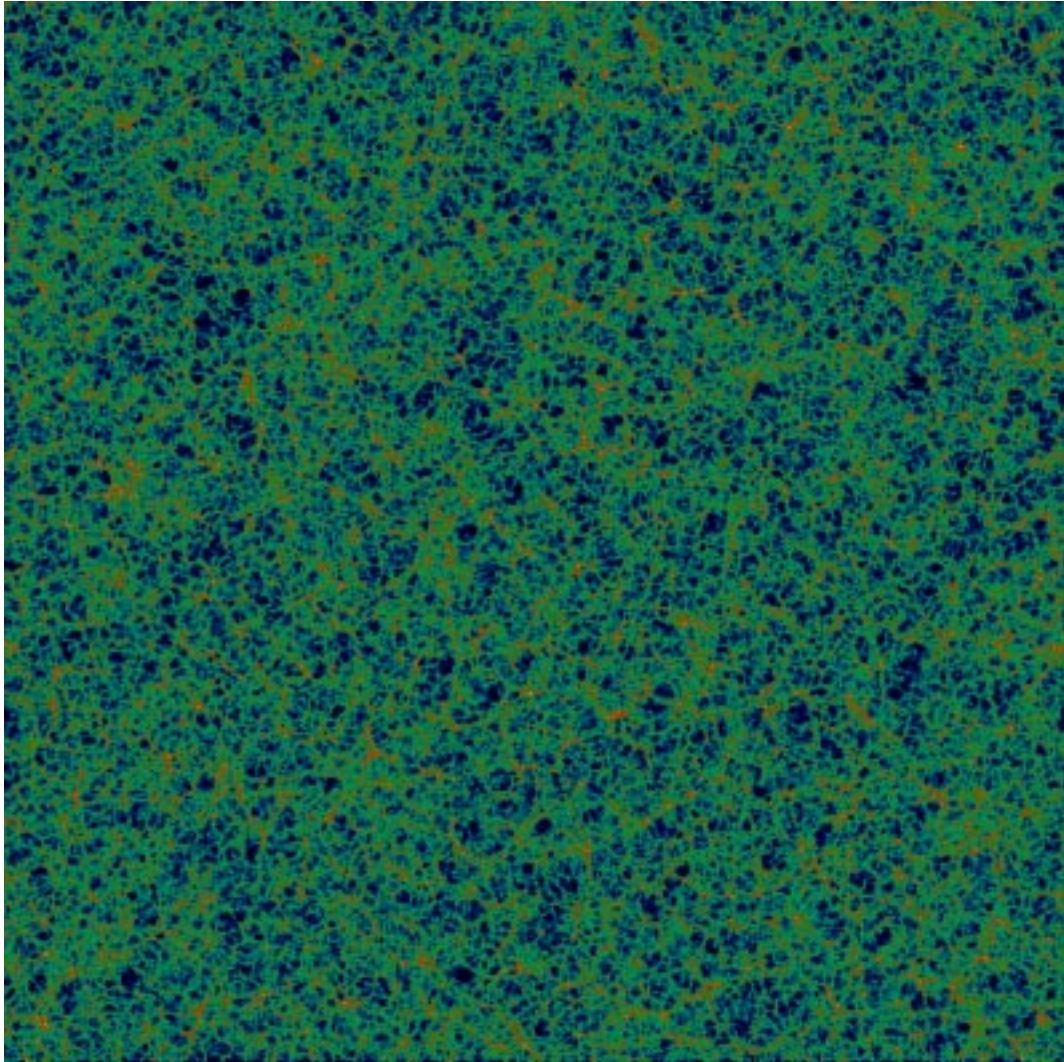
Figure A.16.: A thin slice of thickness $20\,\mathrm{Mpc}/h$ through the τCDM Hubble Volume simulation at $z = 0$.